REACTIVE FLOW IN VUGGY CARBONATES: METHODS AND MODELS APPLIED TO MATRIX ACIDIZING OF CARBONATES

A Dissertation

by

OMER IZGEC

Submitted to the Office of Graduate Studies of
Texas A&M University
in partial fulfillment of the requirements for the degree of

DOCTOR OF PHILOSOPHY

May 2009

Major Subject: Petroleum Engineering

REACTIVE FLOW IN VUGGY CARBONATES: METHODS AND MODELS APPLIED TO MATRIX ACIDIZING OF CARBONATES

A Dissertation

by

OMER IZGEC

Submitted to the Office of Graduate Studies of
Texas A&M University
in partial fulfillment of the requirements for the degree of

DOCTOR OF PHILOSOPHY

Approved by:

Chair of Committee,	A. Dan Hill
Committee Members,	Ding Zhu
	David Schechter
	Hisham Nasr-El Din
	Tahir Çağın
Head of Department,	Stephen A. Holditch

May 2009

Major Subject: Petroleum Engineering

ABSTRACT

Reactive Flow in Vuggy Carbonates: Methods and Models Applied to Matrix Acidizing of Carbonates. (May 2009)

Omer Izgec, B.S.; M.S., Middle East Technical University

Chair of Advisory Committee: Dr. A. Dan Hill

Carbonates invariably have small (micron) to large (centimeter) scale heterogeneities in flow properties that may cause the effects of injected acids to differ greatly from what is predicted by a model based on a homogenous formation. To the best of our knowledge, there are neither theoretical nor experimental studies on the effect of large scale heterogeneities (vugs) on matrix acidizing. The abundance of carbonate reservoirs (60% of the world's oil reserves) and the lack of a detailed study on the effect of multi-scale heterogeneities in carbonate acidizing are the main motivations behind this study.

In this work, we first present a methodology to characterize the carbonate cores prior to the core-flood acidizing experiments. Our approach consists of characterization of the fine-scale (millimeter) heterogeneities using computerized tomography (CT) and geostatistics, and the larger-scale (millimeter to centimeter) heterogeneities using connected component labeling algorithm and numerical simulation.

In order to understand the connectivity of vugs and thus their contribution to flow, a well-known 2D visualization algorithm, connected component labeling (CCL), was implemented in 3D domain. Another tool used in this study to understand the connectivity of the vugs and its effect on fluid flow is numerical simulation. A 3D finite difference numerical model is developed based on Darcy-Brinkman formulation (DBF).

Using the developed simulator a flow-based inversion approach is implemented to understand the connectivity of the vugs in the samples studied.

After multi-scale characterization of the cores, acid core-flood experiments are conducted. Cores measuring four inches in diameter by twenty inches in length are used to decrease the geometry effects on the wormhole path. The post acid injection porosity distribution and wormhole paths are visualized after the experiments.

The experimental results demonstrate that acid follows not only the high permeability paths but also the spatially correlated ones. While the connectivity between the vugs, total amount of vuggy pore space and size of the cores are the predominant factors, spatial correlation of the petro-physical properties has less pronounced effect on wormhole propagation in acidiziation of carbonates.

The fact that acid channeled through the vugular cores, following the path of the vug system, was underlined with computerized tomography scans of the cores before and after acid injection. This observation proposes that local pressure drops created by vugs are more dominant in determining the wormhole flow path than the chemical reactions occurring at the pore level. Following this idea, we present a modeling study in order to understand flow in porous media in the presence of vugs. Use of coupled Darcy and Stokes flow principles, known as Darcy-Brinkman formulation (DBF), underpins the proposed approach. Several synthetic simulation scenarios are created to study the effect of vugs on flow and transport.

The results demonstrate that total injection volume to breakthrough is affected by spatial distribution, amount and connectivity of vuggy pore space. An interesting finding is that although the presence and amount of vugs does not change the effective permeability of the formation, it could highly effect fluid diversion. We think this is a very important observation for designing of multi layer stimulation.

DEDICATION

This work is dedicated to
my mom Fatma Karaca
my brother Bülent İzgeç
& my fiance
Ezgi Can Eren

ACKNOWLEDGEMENTS

I would like to express my sincere appreciation for Dr. Hill and Dr. Zhu for their academic guidance, constructive suggestions and constant support throughout this study. From the beginning to the end they always left enough room for me to think and work independently.

I would also like to thank Dr. Schechter, Dr. Nasr El-Din and Dr. Tahir Çağın for serving as my committee members and for their invaluable comments.

I would like to thank Ryan Keys helping me in core-flood experiments, and Riene Viera for her help in geological classification. I would also like to thank my office and teammates for sharing their time, and knowledge with me: Saleh Al-Mutairi, Abdulwahab Al-Ghamdi, Abdullah Sultan, Jianye Mou, Yoshiaka Keita, Miroslav Mikhailov, Maysam Pournik, Javier Nevito. It was a real enriching experience to work with you.

Being a graduate student at Texas A&M University was a giftful experience for me. Endless homework and class projects, tough exams, failures and successes in my research assignment thought me a very important thing: To think outside the box, first you have to have a box.

My summer experiences with Chevron ETC also contribute to this work by sharpening my engineering skills, extending my horizons. I am grateful to members of Reservoir Simulation Consulting Team in San Ramon and Petroleum Engineering Consulting Team in Houston.

My special thanks go to my mom, Fatma Karaca, and to my brother, Bülent İzgeç, for their support and encouragement.

To my sister in-law, Hilal Özcan, my friends, Can Attila, Dilhan Ilk, Cem Sevik, Olcay Aykaç, and many others: thanks a lot for making my Ph.D. years in U.S. a memorable ones.

The places I live, breath, study and have fun have always been important for me. I would like the name most important ones for my good memories. Places I studied: Richardson Petroleum Engineering Building Office 714, Barnes & Noble Bookstore, It's a Grind Café, Coffee Station Café, Evans Library, Poor Yorick's Café; places I lived: Mill Creek Condos, Renaissance Park Apartments, University Commons (The Trail at Wolfpen Creek), places I had fun: Revolution Café Bar, Fitzwillies.

Finally special thanks go to my fiancé, Ezgi Can Eren, for making my College Station years and my life such a good thing.

When a finger is pointing up to the sky, only a fool looks at the finger…

TABLE OF CONTENTS

Page

ABSTRACT iii

DEDICATION v

ACKNOWLEDGEMENTS vi

TABLE OF CONTENTS ix

LIST OF TABLES xii

LIST OF FIGURES xiii

CHAPTER I INTRODUCTION 1

1.1 Background 1
1.2 Carbonates and Carbonate Acidizing 1
1.3 Objectives 9

CHAPTER II USE OF COMPUTERIZED TOMOGRAPHY (CT) IN POROUS MEDIA FLOW RESEARCH 12

2.1 Basic Principles 13
2.2 Porosity Field Mapping 15
2.3 Use of CT with Vuggy Carbonate Samples 17
2.4 Chapter Summary and Observations 20

CHAPTER III CHARACTERIZATION OF VUGGY CARBONATE SAMPLES 21

3.1 Geological Classification of Barton Creek Samples 24
3.2 CT Data Gathering, Processing, and Prior Image Processing 26
3.3 Visualization of CT Data 32
3.4 Characterization of Core-level Heterogeneities: Geostatistical Approach .. 35
3.5 Characterization of Vuggy Porosity 44
3.6 Chapter Summary and Observations 48

CHAPTER IV EXPERIMENTAL WORK 49

4.1 Experimental Set-up 51
4.2 Experimental Procedure 52

Page

4.3 Experimental Results 53
  4.3.1 Pore volume to breakthrough (*PVbt)* curves 54
  4.3.2 Comparison of pre- and post-injection CT scans: mapping preferential flow paths 63
4.4 Chapter Summary and Observations 66

CHAPTER V NUMERICAL MODEL 67

5.1 Continuity Equation 68
5.2 Equation of Motion: Darcy-Brinkman Formulation (DBF) 70
  5.2.1 Finite difference solution 73
5.3 Convection-dispersion Equation (CDE) 83
  5.3.1 Diffusion, dispersion and convection 83
  5.3.2 Derivation of CDE 85
  5.3.3 Finite difference approximation 88
5.4 Benchmarking 91
5.5 Effect of Connectivity of Vugs on Flow Behavior 92
5.6 Separate Vug Scenarios 95
  5.6.1 Effect of vuggy pore space fraction on *PVbt* 98
  5.6.2 Effect of spatial distribution of vugs on *PVbt* 101
  5.6.3 Effect of size of vugs on *PVbt* 104
5.7 Use of Streamlines 106
5.8 Chapter Observations and Summary 107

CHAPTER VI FROM LABORATORY TO FIELD 109

6.1 Use Laboratory Results to Design Field Treatments 109
  6.1.1 Volumetric wormhole model 110
  6.1.2 Skin calculations 113
6.2 Chapter Observations and Summary 116

CHAPTER VII CONCLUSIONS 118

CHAPTER VIII RECOMMENDATIONS FOR FOLLOW-UP WORK 121

NOMENCLATURE 123

REFERENCES 126

APPENDIX A 132

APPENDIX B 140

Page

APPENDIX C 144

VITA 157

LIST OF TABLES

Page

Table 3.1 Geological classification of the samples. 25

Table 3.2 Geostatistical characterization results of CT monitored experiments. 36

Table 4.1 Experimental conditions and results 54

Table 5.1 Sim parameters used in benchmarking 92

Table 5.2 Simulation parameters used in single vug simulation 96

LIST OF FIGURES

Page

Figure 1. 1 Acid flow in pores with pressure less than fracture pressure 2
Figure 1. 2 Dissolution patterns and wormhole types.. 6
Figure 2. 1 Schematic representation of working principle of CT scanner 14
Figure 2. 2 Visual look to basic CT scanning terminology 15
Figure 2. 3 Pre-processing of the CT data and slice-based statistics 18
Figure 3. 1 Two typical 4 in diameter by 20 inch long vugular core samples used in experiments 24
Figure 3. 2 Surface photo (3.5x3.5 inches) and CT scanner (4x4 inches) images.......... 25
Figure 3. 3 CT scanner slices of BC1 sample 28
Figure 3. 4 Change of total fraction of vuggy pore space throughout the core 29
Figure 3. 5 Digitally constructed 3D images of inner structure of the core samples before acidizing (solid parts showing vugs) 34
Figure 3. 6 Variation of coefficient of variation throughout the core............................. 37
Figure 3. 7 Pair (x_i,y_i) on a scattergram 40
Figure 3. 8 Schematic illustration of concepts used in variogram analysis 41
Figure 3. 9 Larger vugs and/or smaller distance between vugs compared to large distance between vugs and/or smaller vugs (bottom). Corresponding streamlines showing small and fast flow path 43
Figure 3. 10 Pseudo tube concept and lateral CT slices for varigoram interpretation...... 44
Figure 3. 11 3D (left) constructed image of a core sample showing the heterogeneity of the sample studied, and cross sectional view from top (right) 45

Page

Figure 3. 12 Illustration of CCL algorithm: 1) raw image, 2) image while processing, and 3) final image 47

Figure 3. 13 Application of the CCL algorithm on a vuggy rock. From upper left to bottom right: inner structure of the vuggy rock (solid parts are matrix and void parts are vugs), extracted portion of the rock, separate vugs and two vug networks detected by CCL in the region........ 47

Figure 4. 1 Schematic of the experimental set-up used in acid core-flood experiments........52

Figure 4. 2 Experimental results reported for homogenous 1-inch by 6-inch carbonate cores (Wang et al. 1993)........ 55

Figure 4. 3 Experimental results with vuggy 4-inch by 20-inch carbonate cores........ 56

Figure 4. 4 Vuggy carbonate acidizing (this study) and Wang (1993) data on Buijse and Glasbergen plot 61

Figure 4. 5 Experimentally observed relation between total vuggy pore space and *PVbt*........ 62

Figure 4. 6 CT derived distribution of vugs and preferential flow paths (left, color arrows) compared to actual wormhole paths (right) 64

Figure 4. 7 Pre- and post-acidizing porosity and vuggy fraction........65

Figure 5. 1 Control volume used in the model........68

Figure 5. 2 Schematic representation of the finite difference solution algorithm for DBF........75

Figure 5. 3 Simulation domain and boundary conditions........76

Figure 5. 4 Staggered grid used in finite difference approximation 76

Figure 5. 5 Grid configuration and matrix elements........77

Page

Figure 5. 6 Representative coefficient matrix used in calculation of pressure field from Eq. 5.16 77

Figure 5. 7 Comparison of analytical solution and numerical simulation of flow between two parallel plates with DB formulation (ana: analytical, num: numerical) 91

Figure 5. 8 Models used in connectivity investigation 92

Figure 5. 9 Connectivity investigation: change in effective permeability of the domain (keff) as a function of connectivity permeability (kcon) 94

Figure 5. 10 Velocity fields, from left to right increasing connection permeability.........94

Figure 5. 11 Form left top to right bottom: pressure drop, velocity field in main flow direction, velocity field in secondary flow direction and tracer path (respectively) observed near a 1 cm radius separate vug.............................97

Figure 5. 12 Simulation domains with varying vuggy pore space amout.........................99

Figure 5. 13 Effect of vuggy pore space fraction on *PVbt*..100

Figure 5. 14 Simplified simulation domains with varying vuggy pore space amout 100

Figure 5. 15 Dimensionless effluent concentration for domains given in Fig. 5.14........101

Figure 5. 16 Piston like displacement (homogenous permeability), and preferential flow (vuggy/heterogeneous permeability) 102

Figure 5. 17 Simulation domains with varying correlation strength of permeability......103

Figure 5. 18 Effluent concentration for domains given in Fig. 5.17...............................104

Figure 5. 19 Effect of spatial distribution of vugs on *PVbt* 104

Figure 5. 20 Simulation domains with varying vug sizes 105

Figure 5. 21 Dimensionless effluent concentration for domains given in Fig. 5.20........105

Page

Figure 5. 22 Effect of sizeof vugs on *PVbt* 106

Figure 5. 23 Vug network extracted from a real vuggy carbonate rock (left), and corresponding velocity streamlines (right) 107

Figure 6. 1 Volumetric model: wormhole radius as a function of injected acid 113

Figure 6. 2 Schematic representation of the near well bore region with damaged, acidized and original formation 114

Figure 6. 3 Evolution of skin as a function of injected acid and wormhole radius 116

Figure A. 1 Network created in AVS Express for 3D Visualization 138

Figure B. 1 Detailed visualization of a wormhole created after acidizing of 1.5x20 inches carbonate core 140

Figure B. 2 Wormhole created during an acid jetting experiment with 4-inch by 20-inch core 140

Figure B. 3 Inner structure of a highly vuggy carbonate rock (solid parts showing vug network) 141

Figure B. 4 Acid flow path observed in 1x6 inches sandstone core, the area in red circle emphasize the altered permeability region following the acid treatment 141

Figure B. 5 Wormholes created during acid fracturing experiments 142

Figure B. 6 Wormholes created during acidizing experiment using a 1-inch by 6-inch cream chalk core 142

Figure B. 7 Wormholes created during acidizing experiment using a 1-inch by 6-inch cream chalk core. Method of image subtraction used 143

Figure C. 1 Inner structure of BC1 (solid parts showing vugs and/or wormholes)...... 144

Figure C. 2 Inner structure of BC2 (solid parts showing vugs and/or wormholes)...... 145

Page

Figure C. 3 Inner structure of BC3 (solid parts showing vugs and/or wormholes)...... 146
Figure C. 4 Inner structure of BC4 (solid parts showing vugs and/or wormholes)...... 147
Figure C. 5 Inner structure of BC5 (solid parts showing vugs and/or wormholes)..... 148
Figure C. 6 Inner structure of BC6 (solid parts showing vugs and/or wormholes)..... 149
Figure C. 7 Inner structure of BC7 (solid parts showing vugs and/or wormholes)..... 150
Figure C. 8 Inner structure of BC10 (solid parts showing vugs and/or wormholes)... 151
Figure C. 9 Inner structure of BC12 (solid parts showing vugs and/or wormholes)... 152
Figure C. 10 Inner structure of BC13 (solid parts showing vugs and/or wormholes)... 153
Figure C. 11 Inner structure of BC14 (solid parts showing vugs and/or wormholes)... 154
Figure C. 12 Inner structure of BC21 (solid parts showing vugs and/or wormholes)... 155
Figure C. 13 Inner structure of BC22 (solid parts showing vugs and/or wormholes)... 156

CHAPTER I

INTRODUCTION

1.1 BACKGROUND

Matrix acidizing of carbonates is dominated by the wormholing process, the creation of large flow channels in the rock. It is almost certain that the wormhole pathway through the matrix follows local high permeability pathways. Carbonates invariably have small scale heterogeneities in flow properties that may cause the effects of injected acids to differ greatly from what is predicted by a model based on a homogenous formation. Presence of larger scale heterogeneities such as vugs is expected to effect acidizing efficiency drastically. Understanding of effect of vugs on non-reactive and reactive fluid flow is crucial to understand the matrix acidizing in carbonates.

1.2 CARBONATES AND CARBONATE ACIDIZING

Well operations can damage the formation from the first moment the first drill bit penetrates into the pay zone to the end wells productive life. Identifying the cause of the formation damage and developing methods to prevent and/or recover this damage have been the subject of many research. Plugging of the perforations, and/or the rock structure causes dramatic decline in the performance of a well by reducing the ability of hydrocarbons to flow into the wellbore.

The reservoir zone where permeability has been affected by formation damage is referred as skin. The extent of this permeability reduction depends on the amount of damage and the depth to which it occurs.

Matrix acidizing is a technique that has been used extensively since the 1930s to improve production from oil and gas wells and to improve injection into injection wells.

This dissertation follows the style of SPE Journal.

Matrix stimulation is accomplished by injecting a fluid (e.g., acid or solvent) to dissolve and/or disperse materials that impair well production in sandstones or to create new, unimpaired flow channels between the wellbore and a carbonate formation. In matrix stimulation, fluids are injected below the fracturing pressure of the formation. Acid flow is confined to the formations natural pores and flow channels at a bottom hole pressure less than the fracturing pressure **(Fig. 1.1).** Substantial production improvements can be achieved with matrix stimulation if treatments are engineered properly. A success rate of greater than 90% is reasonable. Candidate selection, formation damage characterization, stimulation technique determination, fluid and additive selection, pumping schedule generation and simulation, economic evaluation, execution, and finally evaluation are the major steps of a stimulation task (Economides and Nolte 2000).

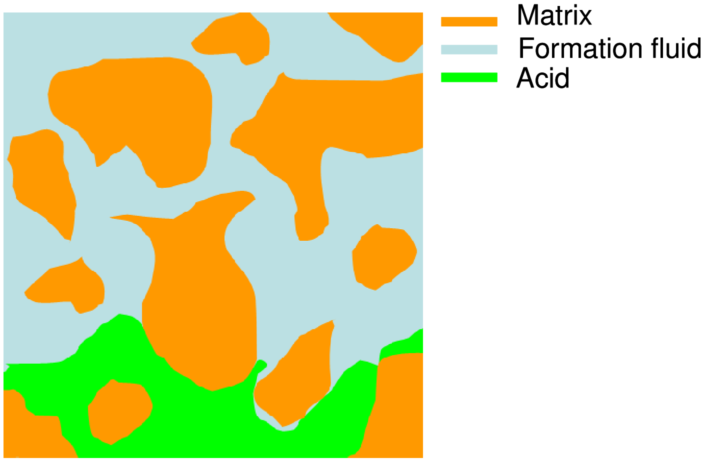

Figure 1. 1 Acid flow in pores with pressure less than fracture pressure

An ideal matrix treatment restores the permeability in the near-wellbore region to a value at least as high as the original undamaged permeability. Any choice of treatment acid should be derived from consideration of the specific problem and should utilize whatever information one has available.

Although both are called matrix acidizing, sandstone and carbonate acidizing differ from each other in many aspects. An acid treatment in sandstones often includes a preflush and/or an afterflush. These fluids must also be selected. Another factor to be considered in selecting an appropriate formulation for sandstone acidizing is mineralogy and petrology of the formation rock.

Carbonate rocks dissolve readily in acid. Although many acid compounds are available in the oil industry, only some of them have been proven economically effective in oil well stimulation. Hydrochloric and hydrofluoric acids are known as inorganic (strong) acids, while acetic and formic acid are the well known organic (weak) acids. The primary objection to the use of organic acids is their cost and lack of effectiveness in removing limestone. On the other hand these acids are used in well stimulation basically because they have a lower corrosion rate and are easier to inhibit at high temperatures than hydrochloric acid. Because organic acids are much less corrosive than hydrochloric or hydrofluoric acid they are used when long acid-pipe contact time is required.

Among others hydrochloric acid is the one mostly commonly used in oil well stimulation. Hydrochloric acid has many advantages in its application as follows:

1. Low cost and availability.
2. Easily inhibited to prevent attack on oil field tubulars.
3. Ability to be emulsified for slower reaction rate.

It has been long recognized that hydrochloric acid is the best field acid for most applications. It has, however, some limitations. The most important limitation is that hydrochloric acid is quite reactive; therefore, it will spend quite rapidly on carbonates. It is essential with hydrochloric acid to size the treatments and pump rates to optimize treatments.

Hydrochloric acid is normally pumped in concentrations ranging from 3.0% to 28%. The low concentration acids are used for the removal of salt plugs and emulsions, whereas high concentrations are selected to create larger flow channels by achieving longer reaction times (exposure). By far the most frequently used strength is 15%, for the following reasons:

1. Less cost per unit volume than stronger acids
2. Less costly to inhibit
3. Less hazardous to handle

Acids release hydrogen (H^+) as the cation when dissolved in water. This can be written, for hydrochloric acid, as:

$$HCl + H_2O \rightarrow H^+ + Cl^-$$

The reaction between hydrochloric acid and carbonates is given by:

$$2HCl + CaCO_3 \rightarrow CaCl_2 + CO_2 + H_2O$$

The rate of reaction between an acid and soluble formation depends on several factors. Among the most important ones are temperature and pressure within formation during treatment, type and concentration of acid used, and the type and purity of the formation.

Although there is no direct way to control the reaction rate between acid and soluble formation, there are some technologies to retard it. An acid system can be retarded by chemical and physical means or by mixing HCl with organic acid. Emulsified, retarded, gelled or cross-linked acids are some examples.

Dolomites are similar to limestones with the exception that they generally react more slowly with hydrochloric acid. Thus, it is important to characterize the formation to be acidized.

Misapplied stimulation treatments are costly and ineffective, creating more problems than they solve. In order to avoid failures several items should be considered as:

1. Type of formation and mineral composition of the formation
2. Type and amount of damage
3. Contact time available for chemical treatment
4. Physical limitations of well equipment
5. Bottomhole pressure and temperature
6. Acid solubility of formation
7. Permeability and porosity
8. Contaminants (water, mud, cement filtrate)
9. No damage, no gain

It is also important to evaluate the production potential. Even if damage exists, the treatment may not be economical if the production improvement potential is not to much.

The principle of a matrix acidizing treatment in carbonate reservoir is to bypass near well-bore damaged region by creating highly conductive channels known as wormholes. When the reaction rate is rapid, the larger pores tend to grow much more rapidly than do the smaller ones. This gives rise to a phenomenon known as wormholing in which a few large holes form and conduct all, or nearly all, of the acid (Schechter 1992). The success of the stimulation depends on the ability of the engineer to control the unstable process creating the wormholes.

There have been number of experimental and theoretical efforts to unlock the mystery behind the formation of fractal wormholes. One of the first experiments was conducted by Daccord (1987) in which water was injected in a plaster core. This study can be seen as the corner stone of the wormholing studies. Following Daccord's study, experimental and modeling efforts so far claimed that creation of wormholes is dominated by two distinct parameters: injection concentration and injection rate. At very low injection rates, acid is spent soon after it contacts the medium resulting in "face dissolution". In this case, acid can only penetrate into a very restricted portion of the damaged zone. As the injection rate increase acid tends to create preferential flow paths named as wormholes. The effect of injection rate, and distinct features of dissolution patterns observed in different injection rates are widely discussed in the literature (Daccord 1987, Fredd and Miller 2000).

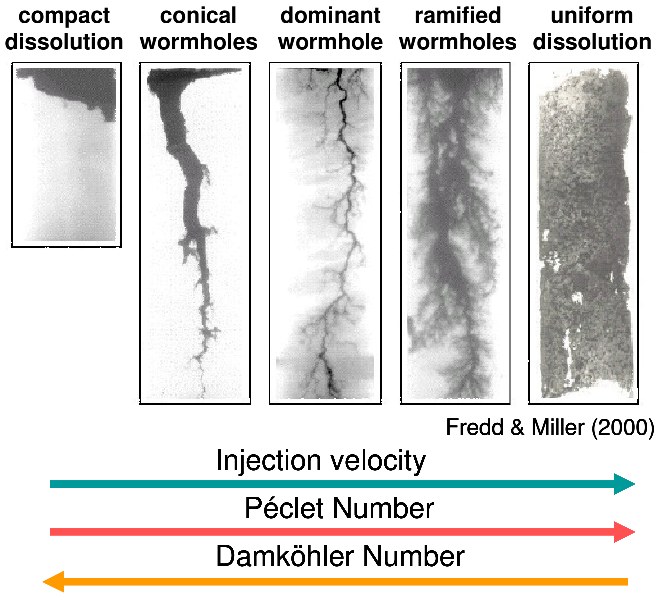

Fredd & Miller (2000)

Figure 1. 2 Dissolution patterns and wormhole types

Different fractal patterns of wormholes created during highly reactive flow in porous media was visualized using metal castings and neutron radiography (Hoefner and Fogler 1988). Later, Hoefner and Fogler extend their experimental and visualization efforts and proposed a network model to capture the pattern of wormholes with different injection rates. Network models represent the porous medium as a network of tubes interconnected to each other at the nodes. These kinds of network models are proved to capture the dissolution regimes resulted from small scale (pore scale) heterogeneities. A drawback of these models is difficulty to scale up to upper levels.

Wang et al (1993) studied the effect of injection rate on wormhole propagation with a large number of core-flood acidizing experiments and theoretical modeling. Hung et al (1989) developed a single wormhole model (a cylindrical tube represents the wormhole) to understand the effects of fluid leakage, reaction kinetics on wormhole growth and density. In early days this simple approach, assuming that a cylindrical wormhole already exists, gained much attention. Huang et. al's (1997), Buijse et. al's (1997) studies build on this assumption. In these models, dissolution of the wall of the tube is studied by solving the transport equation inside the tube. The velocity field is calculated by using Stokes equations. Pretty accurate assumption of zero concentration (for mass-transfer-limited process) at the wall leads to a simple model which gives a good understanding of the dimensionless numbers that govern the dissolution. One of the key results from these studies is the better understanding of the interaction of wormholes and competition between them. Another theoretical approach to understand the wormhole patterns is use of fractal mathematics which is presented by Frick et al (1994). This approach lacks covering the complete physics behind reactive porous media flow. Some investigators conduct radial flow experiments (Daccord et al. 1987, Mostofizadeh et. al. 1994) to fully understand the wormhole phenomenon.

It is clear that understanding the effect of aforementioned parameters on matrix acidizing of carbonates is crucial for a better acidizing design in field acidizing operations. As summarized above most of the previous studies focused on effect on injection rate, temperature, injection concentration, and geometry of the domain on carbonate acidizing. On the other hand, there are few studies focused on effect of heterogeneity in matrix acidizing. It is almost certain that the wormhole pathway through the matrix follows local high permeability pathways. Carbonates invariably have small scale heterogeneities in flow properties that may cause the effects of injected acids to differ greatly from what is predicted by a model based on a homogenous formation. Presence of larger scale heterogeneities such as vugs is expected to effect acidizing efficiency drastically.

Li et al. (2005) conducted a modeling study to understand the effect of small scale heterogeneities in matrix acidizing of sandstones. They concluded that the presence of small-scale heterogeneities in a sandstone has a dramatic impact on the acidizing process.

It has been shown that flow field heterogeneities cause acid to penetrate much farther into the formation than would occur if the rock were homogeneous. The correlation strength of petrophysical properties in flow direction increases the penetration time as much as 17 times. It is expected that in carbonate acidizing case this effect will be more pronounced.

Ziauddin and Bize (2007) recently studied the effects of pore-scale heterogeneities. In their study core samples from eight different carbonate rocks were studied. They characterized samples for mineralogy, texture, fabric, porosity and density distribution using Nuclear Magnetic Resonance (NMR), Computerized Tomography (CT), scanning electron microscopy (SEM), mercury injection, as well as resisitivity measurements and chemical testing. They classified each sample into a Reservoir Rock Type (RRT). They showed how using *PVbt* curves only can be misleading in characterization of acid-rock interactions.

Carbonate rocks often exhibit a wide range of pore sizes because they commonly contain vugs on a scale of one centimeter or larger. Understanding the physics of flow in vuggy carbonates is particularly a challenging problem because we lack knowledge of the distribution and the connectivity of the vugs.

Carbonate rocks commonly exhibit more complex features than sandstone formations because the formation of a carbonate often undergoes two geological processes. The initial process of carbonate sedimentation produces particles with a wide range of sizes and shapes after years of deposition in the ocean environment, where organisms are very active. The post-depositional diagenesis process changes the depositional texture and possibly produces more complicated pore size distribution than the initial carbonate sediments.

The vuggy fabrics which are the products of geological processes include a variety of pore types that generally fall into two groups. The first group is composed of non-tectonic fractures, karst conduits, caverns and collapse breccias; and this group is normally associated with karsting and massive dissolution. The second group is composed of interconnected molds that are associated with selective dissolution of fossil fragments, or voids within or between fossils that were never filled in by sediment (Lucia, 1999).

Carbonate rocks contain more than 50% of the world's hydrocarbon reserves many of them exhibit complex geology such as the vuggy porous system described above. From wateflood to matrix acidizing effect of multi-scale heterogeneities on field treatments has not been understood completely.

There have been several attempts to understand the flow behavior in vuggy rocks, including the more pronounced works of Hidajat et al. (2004), Moctezuma-Berthier et al. (2000), Xu et al. (1998), Zhang et. al. (2004 and 2005), and Arbogast et. al (2004). Zhang et al. conducted number of experiments using vugular rocks to understand the flow characteristics of vuggy rocks. These studies have addressed flow through such media, but not reactive flow as occurs in acidizing.

1.3 OBJECTIVES

The objective of this study is conduct an experimental and theoretical study to understand the effect of heterogeneities in different scales on carbonate acidizing.

For more intellectual interpretation of experiments a characterization approach is developed. In this approach, small scale heterogeneities are characterized by employing geostatistical techniques on the data obtained from CT scanner. A well-known image processing algorithm, connected component labeling, is used to chararacterize the vugs.

Following multiscale characterization acid coreflood tests are conducted with 4-inch diameter by 20-inch long carbonate cores. These core samples are larger in diameter and in length than those used in most of the previous studies, which have typically used one to two-inch diameter cores that were one foot or less in length. Large samples were necessary to provide a meaningful evaluation of acidizing response in rocks with large-scale heterogeneities.

Next in this study, the post acid injection porosity distribution and wormhole paths were visualized after the experiments to understand how wormholes are shaped in the presence of large vugs. A methodology is developed to track wormhole paths by mapping the connections among the vugs.

A model is developed to better understand the effect of connectivity of vugs on fluid flow. A Darcy-Brinkman formulation, as opposed to a Darcy formulation, underpins the proposed modeling approach. The Darcy-Brinkman formulation (Brinkman 1947) allows a natural transition between porous media flow and Stoke's free flow. This enables one to simulate flow through separate vugs, connected vug networks, and partially-filled (damaged) vug networks. By appropriate choice of parameters (k, and μ) the interface between rock and vug can be efficiently simulated. The combined experimental and theoretical approach is used to understand, show and discuss the major differences between acidization of non-vuggy and vuggy carbonates.

Chapter II gives a brief overview of basic principles of computerized tomography (CT). Discussed in this chapter are the recent developments in use of CT in porous media flow research, and basic equations for porosity mapping. An introductory study of use of CT scanner with vuggy carbonates is also presented in this chapter.

Chapter III gives the details of CT data gathering, processing and multi-scale characterization approach presented in this work. Here the details of the developed geostatistical approach and the method for investigation of the connectivity of the vugs are discussed.

Chapter IV summarizes the experimental work done in the scope of this study. Experimental set-up, procedure and finally the results are presented. Following discussion of pressure drop behavior in experiments, a wormhole tracking algorithm is presented to be used with CT data.

Chapter V covers the numerical modeling study done in this work. Finite difference approach for solutions of Darcy-Brinkman formulation (DBF) and continuity equation, and convection dispersion equation (CDE) are presented. Several conditions and scenarios are investigated.

Chapter VI demonstrates the derivation and use of a simple volumetric model, and a skin calculation for scaling up the laboratory results to field size.

Chapter VII gives a brief discussion of results.

Chapter VIII summarizes the author’s recommendations for the future work.

CHAPTER II

USE OF COMPUTERIZED TOMOGRAPHY (CT) IN POROUS MEDIA FLOW RESEARCH

Invented for medical purposes, the CT scanner is now being used for a wide variety of applications. These include studies of flow in porous media.

Honarpour et. al (1985) used CT to develop reservoir rock descriptions for formation mineral and rock property evaluation. Rock fabric heterogeneities such as directional permeabilities, macroscopic permeability barriers, and fracture system orientations were demonstrated in their study using CT. Auzerais et. al (1991) imaged the inside of a rock sample while filtrate fluid was injected through. They benefited from CT by verifying their theoretical developments with CT monitored experimental results. Bartko et. al (1993) studied the use of CT scanning in the investigation of acid damage to sandstone cores. They used the dual energy method (Siddiqui and Khamees 2004) to determine the porosity change in volume elements in sequential axial slices along the length of the core. They reported successful identification of the location of precipitation byproducts through changes in density.

Visualization of wormholes created during acid injection into the carbonates were reported by Bazin et. al (1996). Although claimed in their work, classification of dissolution patterns using CT is less than satisfactory in their work.

Recently, Tardy et. al (2007) used CT scanning technology in a study on use of self-diverting acids in matrix acidizing. They presented 2D CT images to validate their numerical model.

In this chapter, we briefly discuss the basic principles and porosity field mapping approaches. Then, we will use these concepts to develop our characterization approach, which will be presented in **Chapter III**.

2.1 BASIC PRINCIPLES

X-ray CT is a radiological imaging technique first developed in Great Britain in 1972 by Hounsfield (1972). CT revolutionized medical radiology by producing anatomical images of extraordinary accuracy and clinical detail. Hounsfield was awarded the Nobel prize in medicine in 1979 for his contributions (Wellington and Vinegar 1987).

Invented for medical purposes, the CT scanner is now being used for a wide variety of applications. These include studies of heterogeneous rocks, fractures, vuggy carbonates and determination of rock properties like porosity and bulk density.

Computerized Tomography (CT) is a non-destructive imaging technique that uses X-Ray technology and computerized mathematical algorithms to reconstruct an object from a series of plane cross-sectional images made along an axis. When an object, such as a core plug, is CT scanned focused and collimated beams from an X-Ray source penetrate the object and the emergent beams are captured by a set of detectors. The X-Ray source and detectors move around the object to cover the entire 360 degrees at each scan location. Different than machines used in medicine, so-called industrial scanners utilize high energy X-ray sources since they don't examine living subjects. A schematic representation of the basic working principle of CT scanner is given in **Fig. 2.1**.

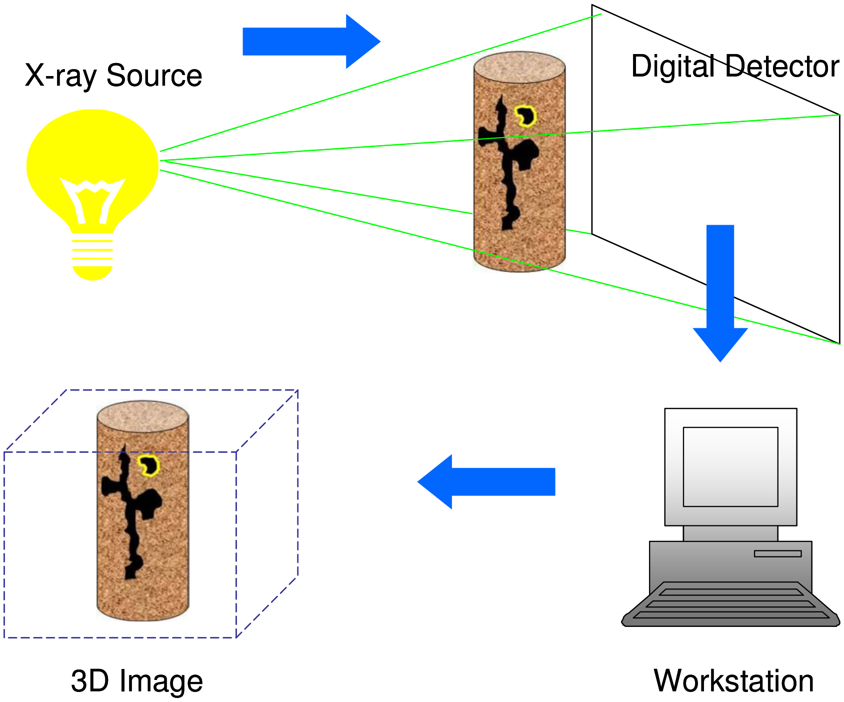

Figure 2. 1 Schematic representation of working principle of CT scanner

The attenuation of the energy in the X-Ray beams is related to electron density and atomic number of the materials present in the object being scanned. Each material possesses a distinct linear attenuation coefficient, and the total response received by the detectors is a combination of these coefficients. The linear attenuation coefficient, ξ, is given by Beer's law as follows (Akin and Kovscek 2003):

$$I = I_0 e^{-\xi h} \tag{2.1}$$

Here, I_0 and I are the intensities of the incident and the detected X-Ray beams, respectively, and h is the thickness of the object. The linear attenuation coefficient, ξ, depends on electron density (bulk density), ρ_{bulk}, and atomic number, Z.

CT attenuation data are presented in an internationally standardized scale called Hounsfield unit. The unit is based on the CT number (*CTN*) of air at -1000 and of water at 0 Hounsfield units (Wellington and Vinegar 1987). Thus, each Hounsfield unit represents a 0.1% change in density. *CTN* in Hounsfield units is given by (Akin and Kovscek 2003):

$$CTN = \frac{\xi - \xi_w}{\xi_w} .1000 \qquad (2.2)$$

Fig. 2.2 provides a visual description of the common CT-scanning terms.

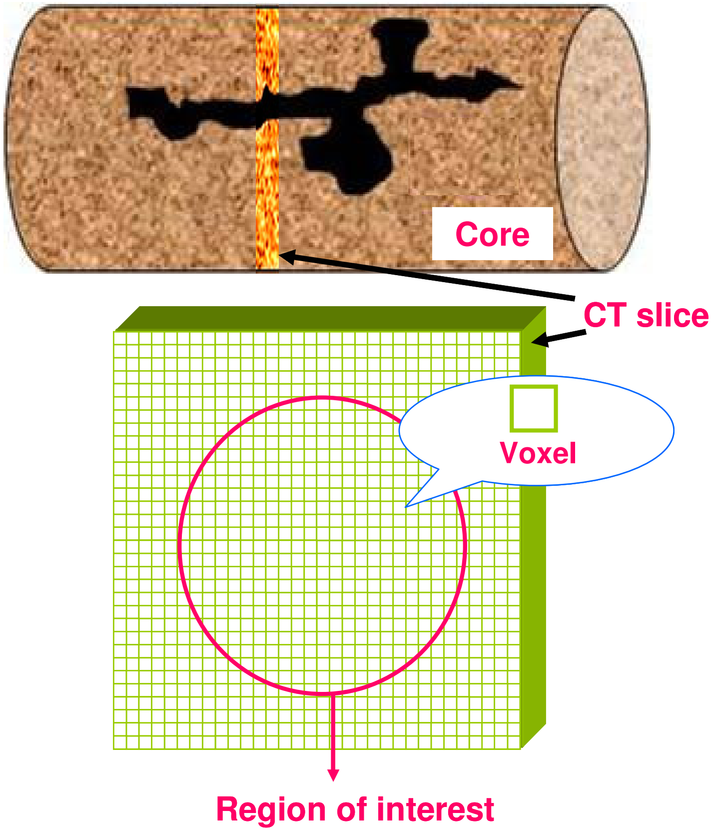

Figure 2. 2 Visual look to basic CT scanning terminology

2.2 POROSITY FIELD MAPPING

Calculation of porosity and in-situ phase saturation is possible once CT numbers are measured. The only preparation that is absolutely necessary for CT scanning is to ensure that the object fits inside the field of view and that does not move during the scan.

In this study since we are interested in both pre-injection and post-injection CT scans, it also important to start scanning the sample at the same point. Simply marking this point with a marker would resolve this issue.

The CT number was converted to bulk density based on specific conversion units presented in the literature (Akin and Kovscek. 2003, Withjack et al. 1991) The conversion equations, in turn, are based on the CT response of some known bulk densities. The conversion equation has the following general form (Akin and Kovscek. 2003):

$$\rho_{bulk} = aCTN + b \tag{2.3}$$

where *CTN* is the CT number, *a* is the slope, and *b* is the intercept of the linear equation relating the *CTN* of the standards with their corresponding bulk densities. Once the bulk density is known, porosity can be calculated using equation 2.4 provided the density of the matrix ρ_{ma}, and the fluid ρ_f are also known. This method assumes a linear relationship between X-ray attenuation and bulk density, which is appropriate for samples with uniform mineral composition.

$$\phi = \frac{(\rho_{matrix} - \rho_{bulk})}{(\rho_{matrix} - \rho_{fluid})} \tag{2.4}$$

With this formula, it is possible to calculate the porosity of each voxel. The average porosity was calculated by taking an average of the porosity in each voxel in the rock sample. The density of the matrix is calibrated so that the CT derived porosity is in accord with the one calculated in the lab.

It is important to be aware that measurements with X-ray CT are subject to a variety of errors. Following Van Geet et al.'s (2001a, 2001b) study, Akin and Kovscek (2003) discussed these errors briefly. The majority of CT scanners were developed for medical purposes. The objective of using these machines was to obtain a qualitative image, as opposed to quantitative analysis aimed in industrial usage. The errors associated with CT scanners can be summarized as: i) beam hardening, ii) star-shaped or so-called X-artifacts, iii) positioning erros, and iv) machine errors. Interested reader should refer to great reports by Akin and Kovscek (2003), Ketcham and Carlson (2001), Wellington and Vinegar (1987).

2.3 USE OF CT WITH VUGGY CARBONATE SAMPLES

The CT imaging was conducted with a 4th generation CT scanner. X-Ray CT scans were taken along the core. The cores were scanned from inlet to outlet of the core. The slice thickness and separation distance between slices were 2 mm. Slice-based statistics were studied for quick understanding of the degree of heterogeneity. **Fig. 2.3** illustrates a typical screenshot for the initial step of the CT scanning part of the study. Pre-processing of the CT data and slice-based statistics are given in this figure. First, data is transferred from the CT scanner to a SUN workstation. Then, the data is transferred from the SUN workstation to Microsoft Windows environment. Upon transferring and storage of the data, the commercial package VoxelCalc was used for region-of-interest (ROI) statistics.

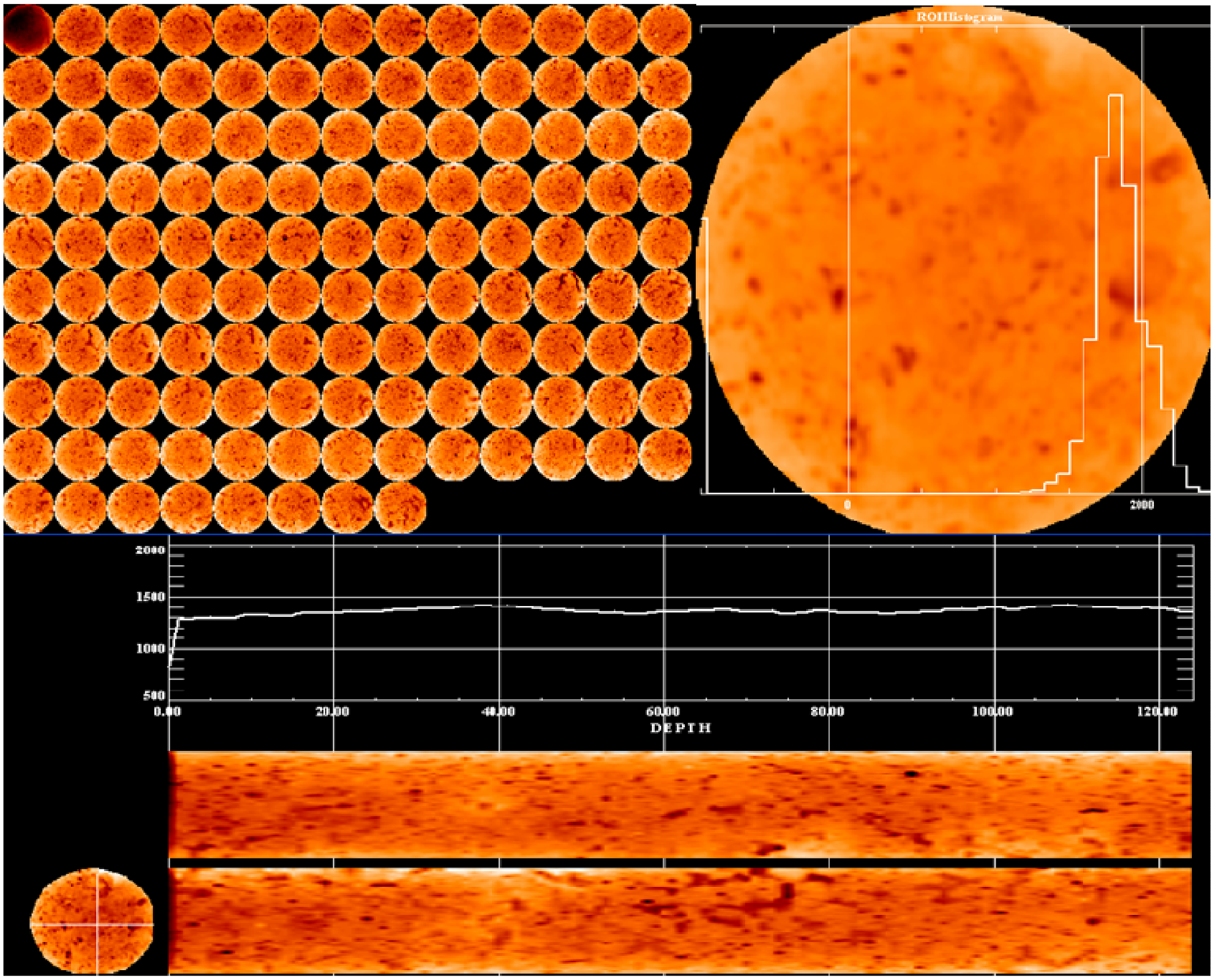

Figure 2. 3 Pre-processing of the CT data and slice-based statistics

Besides their simplicity, slice-based statistics are a very efficient way of understanding the degree of heterogeneity at first glance. One of the statistics used is histogram. In statistics, a histogram is a graphical display of tabulated frequencies, shown as bar. It shows what proportion of cases fall into each several categories. A histogram of a slice of a vuggy core is given in **Fig. 2.3.**

Using VoxelCalc software, it is possible to create horizontal and vertical slabs. CT orthogonal reconstruction of a sample of Barton Creek carbonate is given in the bottom section of **Fig. 2.3.** Cross-sectional slices are useful for understanding the inner structure of a rock.

We recommend the following procedure to be followed in each sample to be studied prior to detailed analysis.

1. Scan the core using the guidelines given in **Appendix A.**
2. Transfer the data from the CT scanner to the SUN workstation.
3. Use a FTP program to transfer data from the SUN workstation to a Windows-based computer.
4. Open VoxelCalc and load the CT slices.
5. Use the ROI feature of VoxelCalc to eliminate background (air outside the core) data.
6. Use slice-based statistics and orthogonal reconstruction for initial assessment of the degree of heterogeneity.
7. Export data in raw or ASCII format to analyze.
8. Calculate point-wise porosity for each voxel using Eq. 2.3, and Eq. 2.4.

A complete guideline from scanning a core to porosity mapping is given in **Appendix A.**

Using the ability of VoxelCalc to export the data in varying formats (ASCII, raw, CSV, FLD, HDF) the complete set of CT data (512x512x200) is written in raw format to be analyzed in a different environment.

Upon exporting the data, using Eq. 2.3 to Eq.2.4 porosity of each voxel was calculated. The details are given in **Chapter III**.

Another simple approach used in this study to calculate voxel porosity is by using a simple linear relation.

$$\phi_{i,j} = \frac{\overline{\phi_s}}{\overline{\overline{CTN_S}}} CTN_{i,j} \tag{2.5}$$

2.4 CHAPTER SUMMARY AND OBSERVATIONS

Use of CT scanning in porous media flow research is reviewed. Basic principles were studied. A workflow including scanning a core, and exporting the data to Windows environment, pre-processing the CT data including slice-base statistics, exporting the data for geostatistical analysis was presented. Methods for qualitative and quantitative preliminary investigation of core heterogeneity are presented using commercial software.

CHAPTER III

CHARACTERIZATION OF VUGGY CARBONATE SAMPLES

Despite the hydrocarbon wealth they hold, carbonate rocks are known to be the toughest rocks to be understood and characterized. They have either very complicated interrelationships, or no interrelationships at all between porosity and permeability. The importance of this difficulty becomes more pronounced considering the different relevant scales. A particular technique might not be suitable for all relevant scales; what works at one well might be inadequate for others, or for the rest of a field.

Unlike siliciclastic reservoirs, which form through erosion and transportation of material from existing rocks, carbonate rock-forming materials develop mainly through biological activity and, to a lesser degree, inorganic precipitation. Evolution of carbonate-producing organisms add complexity to carbonate rocks, and to relevant studies.

Physical, biological, and chemical variations create heterogeneous rock textures and fabrics during and after deposition, often destroying any comparatively simple relationships that might have existed between depositional attributes, porosity and permeability (Ahr 2008).

The petrophysical classification of carbonate porosity presented by Lucia (1983) emphasized petrophysical aspects of carbonate pore space, as does Archie’s classification (Archie 1952). Lucia (1983) proposed a useful division of pore types for petrophysical purposes. His approach consists of dividing pore space into two major categories as interparticle porosity and vuggy porosity. The pore space between grains or crystals is called interparticle porosity. Vuggy pore space was further subdivided into two groups depending on how the vugs are interconnected: i) vugs interconnected only through the interparticle pore networks are separate vugs, and ii) vugs that form an interconnected pore system are touching vugs.

Accurate characterization of pore space in a vuggy sample is crucial to interpreting the laboratory results. Several researchers studied the vuggy rocks in many aspects and present different techniques to characterize vuggy carbonate samples.

Xu et al. (1999) developed a pore network model and a calibration methodology for calibrating this model to be used in investigation of several aspects of waterflooding in vuggy carbonates. They used thin sections to quantify pore size, and mercury injection for throat sizes. Spatial correlation in the core sample was evaluated using thin sections and CT data using a geostatistical technique, variogram. SEM (scanning electron microscopy) was used to determine coordination number (the number of bodies to which each pore body is connected on average). One of the interesting results of their characterization effort is that they obtained same spatial correlation length of porosity from both thin section and CT scanner. Note that the length scale of both methods is orders of magnitude different form each other (micron for thin section, and mm to cm in CT scanner).

Hidajat et al. (2004) incorporated NMR (nuclear magnetic resonance) T_2 measurement, mercury porosimetry, thin section imaging (using optical microscopy and SEM), CT scanning, and electrical measurements to understand the contribution of vuggy pore space to permeability. Their main observation was a well-known one which states "*different length scales of heterogeneity, from microscopic to macroscopic level, make the property prediction for carbonate formations very challenging*". One of the important observations reported in their study is that although some of the samples contain highly vuggy pore space, they have very low permeability. We observed the same behavior in our core-flood experiments and further investigate and clarify this issue using the developed numerical model. The details can be found in **Chapter IV**.

Zhang et al. (2004, 2005) presented the results of their study on vuggy carbonates in two reports. Their "chunk flow" experiments with carbonate chunks were followed by CT scanning, capillary tube models, connected volume calculations, and high resolution numerical simulation of single-phase flow and solute transport. Their observations are in accord with the previous studies. Major findings from this study are: i) the vug connections and the permeability are scale dependent, ii) partitioning the pore space into to vuggy space and matrix pore space is a prudent approach for characterization and modeling studies, iii) further portioning the vuggy space as separate, touching or dead-end vugs is important to understand the flow behavior, and iv) Darcy's law only is not adequate to describe flow in complex vuggy carbonates.

Moctezuma-Berthier et al. (2000) proposed a method for permeability mapping on vuggy carbonate cores based on CT scanning and NMR T_2 distribution. Basically, NMR T_2 distribution was performed to evaluate the total contribution of vugs to the total porous media. The permeability map was generated based on the porosity map with a simple transformation: Cells with porosity higher than a given cut-off have a high permeability (permeability in vugs), and lower porosity parts have a low permeability (permeability in matrix). The vug volume fraction obtained from NMR T_2 distribution was used to calibrate the cut-off. Although the method might be useful, the cut-off value of 0.2 they used has no physical explanation. In this study we used a similar binarization approach to define vuggy and matrix pore space with the given physical explanations.

Previous studies present the use of CT scanner, geostatistical functions, image processing, mercury injection, empirical relations, and NMR T_2 as tools for carbonate core characterization. The complexity of the pore structure encountered in vuggy carbonates made it difficult to interpret the laboratory results. Different scales of the problem demand a multi-scale approach for characterization.

In this chapter a multi-scale characterization approach is presented to enhance our ability to interpret the laboratory results. First, geological classification of the carbonate rocks is presented. Following that, two statistical measures to evaluate the spatial distribution of vugs in the sample are presented. The importance of the correlation length of petrophysical properties are illustrated using the developed numerical simulator. Later in **Chapter V** we propose use of an image processing technique in a 3D domain, as opposed to prior conventional approaches using 2D domains. This algorithm, called *Connected Component Labeling*, enables us to understand the connectivity of the vugs and distribution of the largest separate vugs in CT originated highly fuzzy data set. A binarization approach based on geological classification of vugs is presented to calculate the contribution of vugs to the total porous space in the core.

3.1 GEOLOGICAL CLASSIFICATION OF BARTON CREEK SAMPLES

All samples were cut from an Edwards limestone outcrop boulder collected near Barton Creek in Austin, Texas **(Fig 3.1)**. The samples were geologically classified in terms of pore origin and type, and mineralogical constituents **(Table 3.1).**

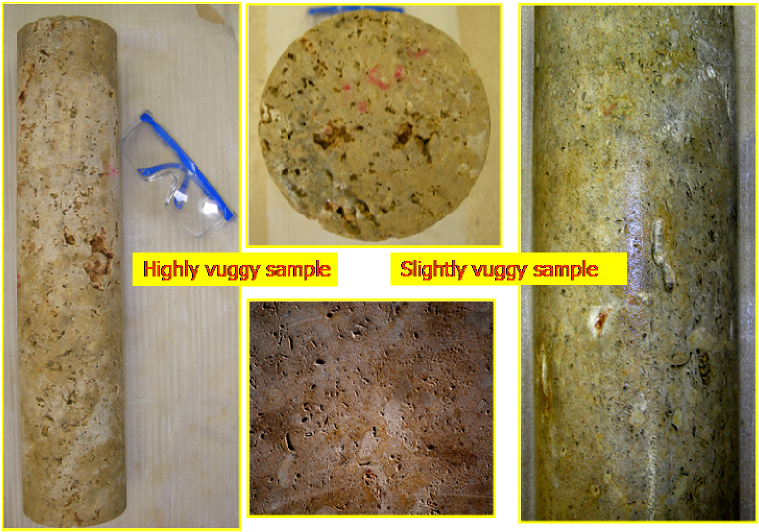

Figure 3. 1 Two typical 4 in diameter by 20 inch long vugular core samples used in experiments

The lower cretaceous carbonates in Central Texas used in this study are geologically similar to the Thamam group in the Middle East. Vuggy porosity can be seen from surface photos and the CT images **(Fig. 3.2).** The vug sizes were determined to be 1.4-11.4 mm. It was observed from surface photos and CT images that there are three distinct regions. Light colored regions in the sample correspond to matrix, whereas dark and black colored regions represent mud-filled and clean vugs respectively. The mineralogical heterogeneity was measured by staining the samples with Alizarin Red-s (ARS), and it was found that the core samples had no significant mineralogical heterogeneity.

Table 3.1 Geological classification of the samples

Rock-type	Limestone
Color	Yellowish white
Bedding&sedimentary structure	Burrows filled with lighter color, finer grain of skeletal debris, pelloids, and mud
Dunham's Classification	Packstone/grainstone mixture (skeletal debris packstone/grainstone with some pelloids)
Main grain types	Skeletal debris with the walls condition dissolved and filled by calcite in may places. Some pelloids.
Visible porosity	Abundant pelloid and skeletal moldics, interparticle, intraparticle, dissolution enhanced, vuggy
Cement	Calcite
Matrix	Calcite
Ahr's genetic classifcation	Hybrid 1 (hybrid of depositional and diagenetic processes)

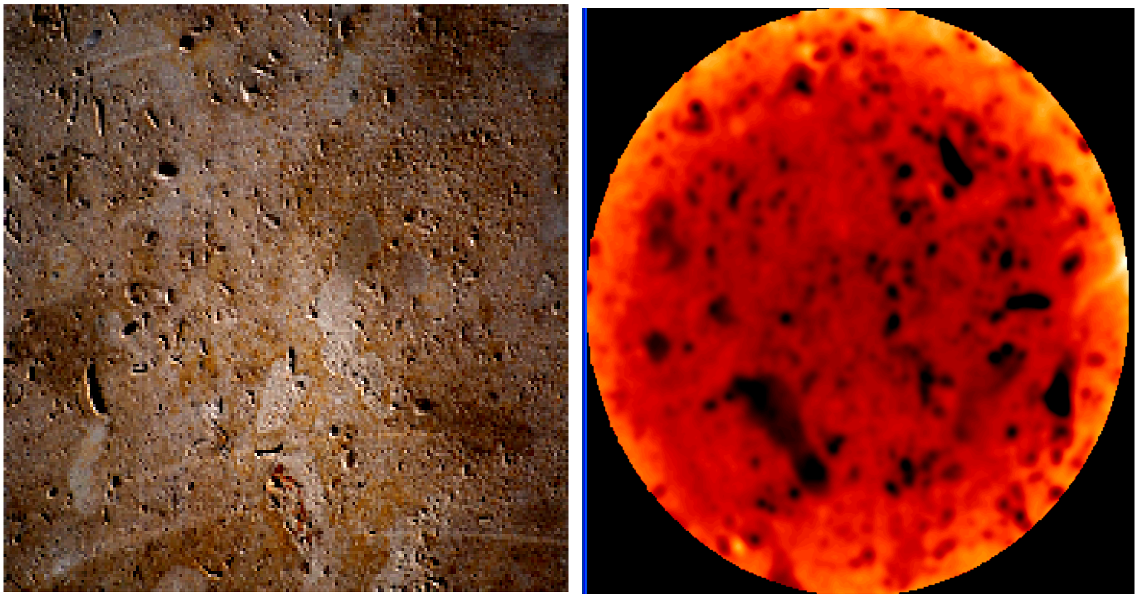

Figure 3. 2 Surface photo (3.5x3.5 inches) and CT scanner (4x4 inches) images

3.2 CT DATA GATHERING, PROCESSING AND PRIOR IMAGE PROCESSING

The cores were scanned with an industrial high-resolution X-ray CT scanner at Texas A&M University, Department of Petroleum Engineering. Compared with medical scanners, this instrument operates at higher energies, which enables users to scan high-density objects with higher resolution.

X-Ray CT scans were taken along the core. The slice thickness and separation distance between slices were 2 mm. A total of 150-200 slices were taken, depending on the desired resolution. Each scanned slice was reconstructed with 512 x 512 pixels, each of which is a square with sides of 0.3 mm by 0.3 mm. Therefore, the size of the data matrix was 512 x 512 x 200. **Fig. 3.2** shows an image of a CT slice. It was observed from the surface photo and CT image that there are three distinct regions. As mentioned above, light colored regions in the sample correspond to matrix, whereas dark and black colored regions represent mud-filled and clean vugs respectively. The scanned region can be categorized into four regions: i) the region outside the core, ii) matrix, iii) vugs, and iv) mud-filled vugs. Since the aim is to characterize and to better understand the variability of petro-physical properties, the first region (outside) was eliminated while exporting the CT data to be analyzed. Details of the procedure are given in **Appendix A.** The heterogeneity of the core sample can be seen in **Fig. 3.3** where the images of each slice are given.

Once the porosity of each pixel was calculated using given relations, the image was binarized so that each pixel can be represented by only two value 1) matrix, and 2) vug. It appeared that it is also possible to define each pixel by three different values as: 1) matrix, 2) vug, 3) mud-filled vugs as discussed above. In this study we choose to describe mud filled/partially mud-filled pixels as “vug” cells, since originally the vugs were not accumulated with mud or sediments (subsurface condition). The pixels having porosity value ~1 were labeled as vug pixels. Mud-filled (less dense material then matrix) pores give an apparent porosity much larger than matrix but also smaller than 1. For example, for a sample with an overall average porosity of 0.25, we labeled any pixel with porosity less than 0.35 as matrix, any pixel with porosity greater than 0.9 as a vug, and any pixel with an apparent porosity between 0.35 and 0.9 as a mud-filled vug.

Upon binarization of the scanned domain, the vuggy porosity fraction of each CT slice was calculated by calculating the number of the vug voxels in each slice and then normalizing it with the total number of the voxels in region of interest (ROI) of each slice. This gave a detailed representation of the variation of vuggy space throughout the core sample. Results of the analysis for samples used in CT monitored experiments are given in **Fig. 3.4.** Total vuggy porosity fraction of these samples can be found in **Table 3.2**.

The data gathering and processing method can be summarized with 4 main steps: i) transferring CT data from scanner to connected Unix workstation, ii) transferring data from Unix to Windows environment, iii) processing data to be exported (threshold, binarization, elimination of "outside" region), iv) labeling each voxel (vug, matrix), and the other steps including calculating the vuggy porosity fraction, data formatting for variogram, and data preparation for numerical simulation. The details of these steps will be discussed in the following sections.

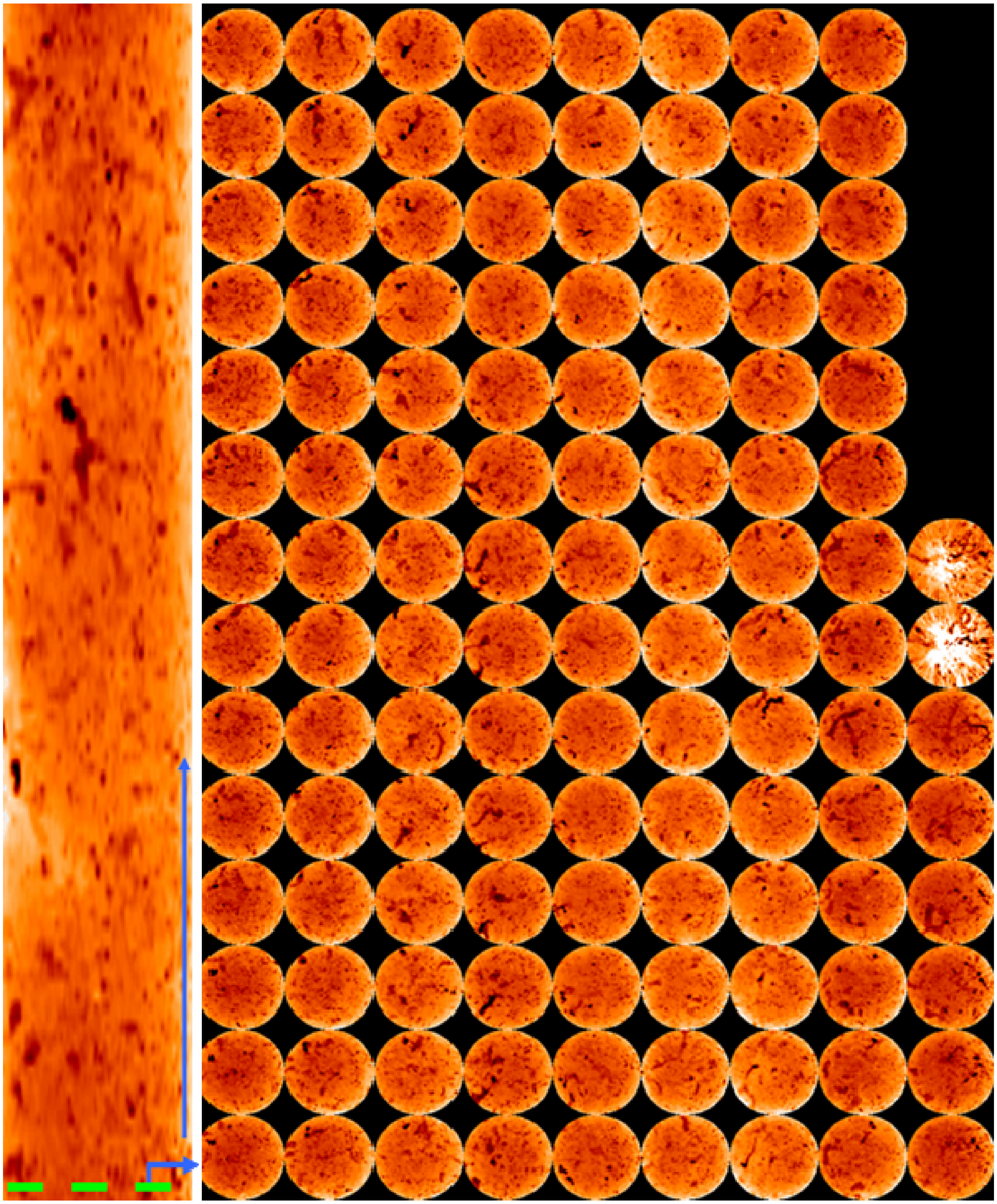

Figure 3. 3 CT scanner slices of BC1 sample

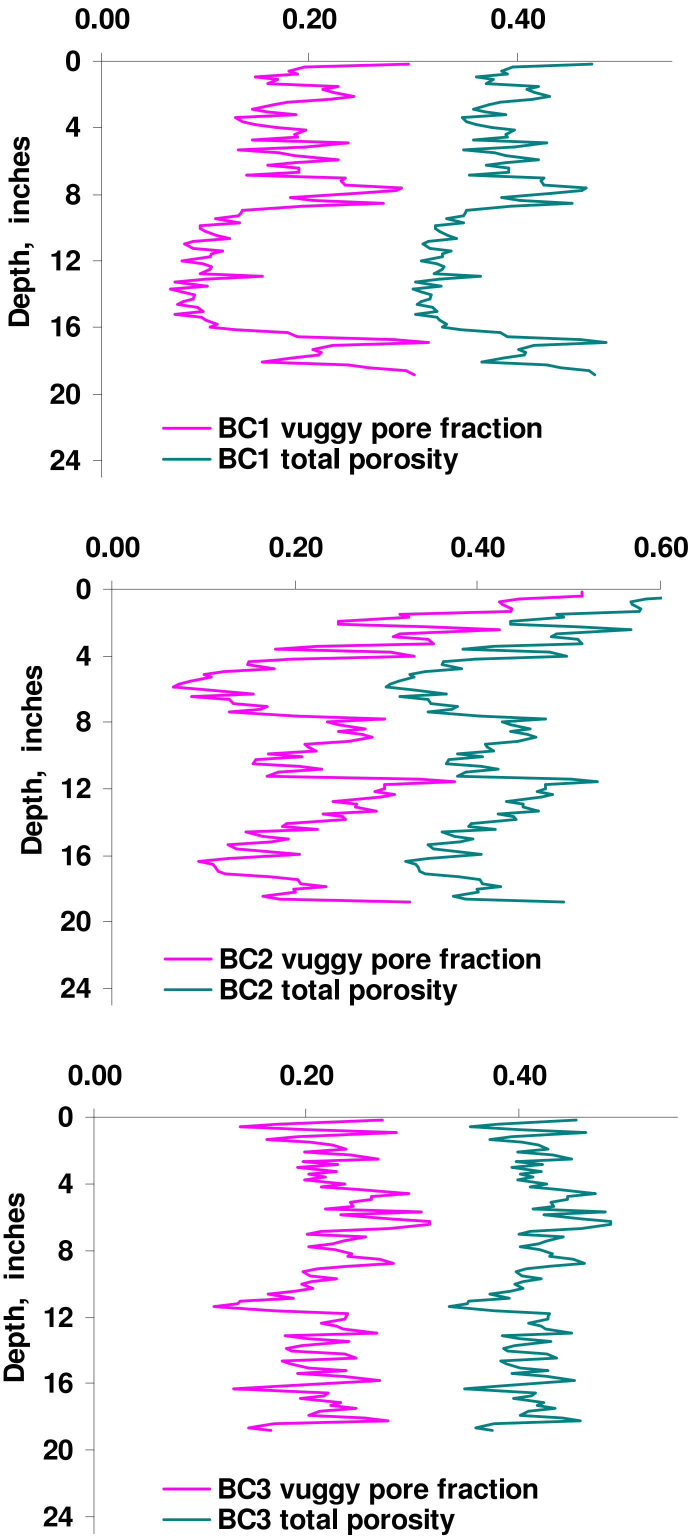

Figure 3. 4 Change of total fraction of vuggy pore space throughout the core

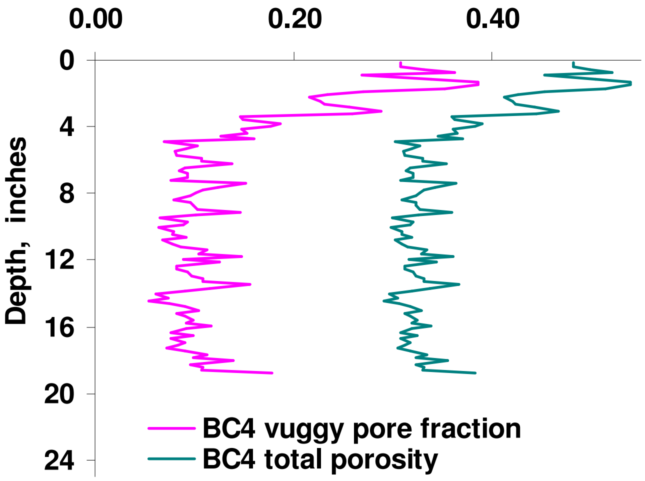

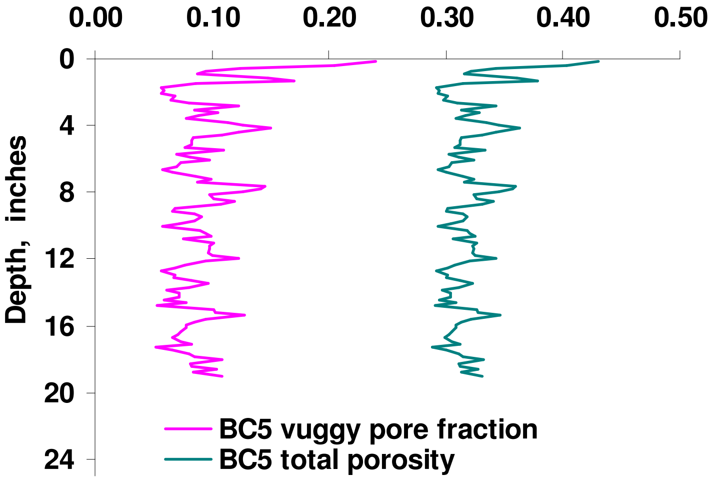

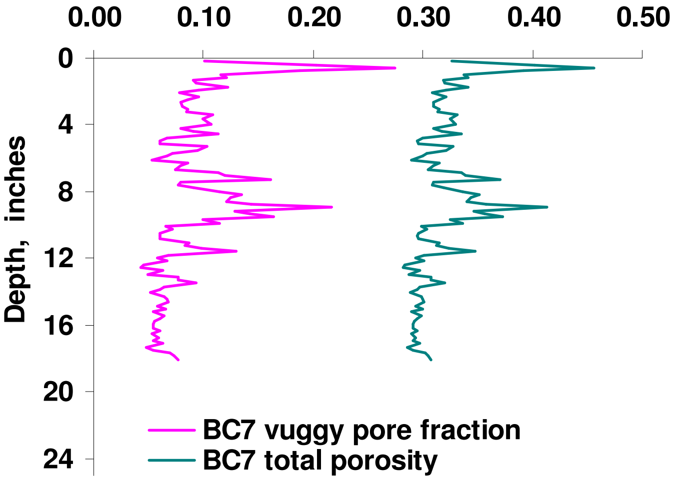

Figure 3. 4 cont.

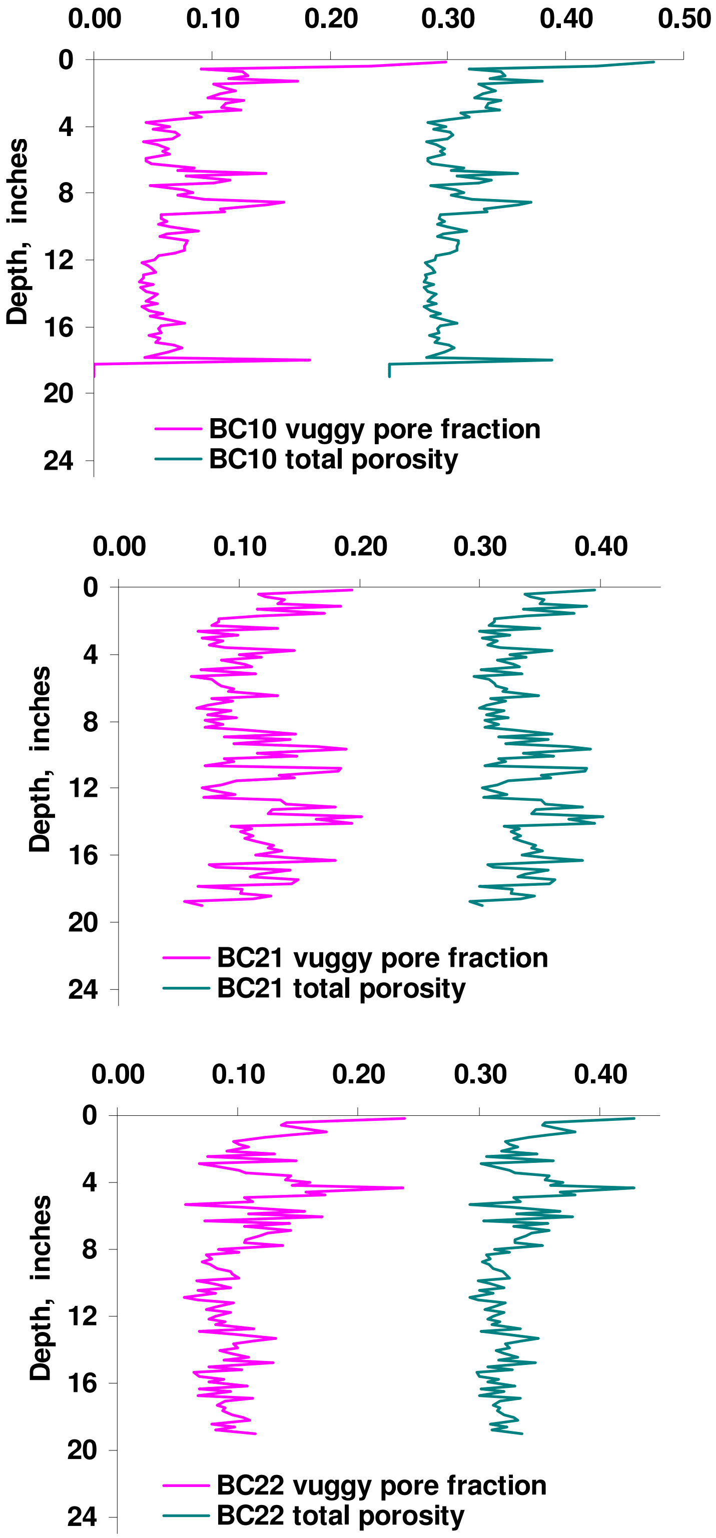

Figure 3. 4 cont.

3.3 VISUALIZATION OF THE CT DATA

Visualization is an important way of understanding the scientific data set. Also it is important for communication, in other words, sharing and transferring the knowledge. Image processing is the art of capturing and manipulating the digital images to enhance and extract information.

Following the geological classification, voxel-based porosity calculation and determination of contribution of vuggy pore space to total pore space, the next step of our characterization methodology is visualization of the CT data. The main objective of pre-injection visualization of the inner structures of the samples is to compare them with post-injection images to obtain clues about wormhole propagation behavior in vuggy carbonates.

Image processing spans a sequence of three steps. First, image is captured and digitized. In this step differences in coloring and shading in the picture is converted into binary values that a computer can process. Second, images can be enhanced and data can be compressed in a processing step. The final step consists of the display or printing of the processed image.

Following transferring the CT data to Windows environment we used a well-known commercial product, VoxelCalc, to process the raw CT data. VoxelCalc is commercial software that is designed for analyzing petrophysical CT-scan data. VoxelCalc incorporates many advanced features such as region of interest (ROI) statistics, selective histogram analysis, slice alignment, pore volume weighted porosity, and density-atomic number calculation. It is capable of reading files generated by various manufacturers of CT equipment. The binary files on single or multiple slices can be exported in the more universal formats such as FLD (developed by Advanced Visual Systems, AVS) and HDF (Hierarchical Data Format, developed at the National Center for Supercomputing Applications) used by three-dimensional image processing software such as OpenDX, AMIRA and AVS-Express. This feature is also the key to obtain data for numerical simulation.

Detailed data processing and evaluation such as ROI based quantitative calculations were done by using the VoxelCalc software. The image data processing with VoxelCalc used in this study involves the following steps: i) read the original data files in CT-scanner's binary format, ii) select region-of-interest within the core material, avoiding the Hassler Sleeve, core holder, and air outside the core iii) generate slice images and slab images, iv) generate statistical data within the ROI (mean, standard deviation, minimum, maximum), and v) export to FLD or HDF format for further processing using 3-D imaging software.

The most pronounced disadvantage of VoxelCalc is its inability to generate good 3-D views based on the CT-data. To cover this inefficiency of the program, we used another commercial package, AVS Express. AVS Express is a powerful 3-D image processing package by Advanced Visual Systems for scientific visualization. AVS-Express is a modular, hierarchical, open and extensible system, with hundreds of built-in predefined components for visualizing the data. AVS uses field-formatted (FLD) data by default but it is possible to import data in many other standard formats.

The slice images of the core were given in **Figs. 3.2** and **3.3**. Using these data, 3D images of the samples studied were constructed using AVS Express **(Fig. 3.5).** In these 3D images vugs can be seen easily. More detailed versions of these models are given in **Appendix B** together with post-acidizing images.

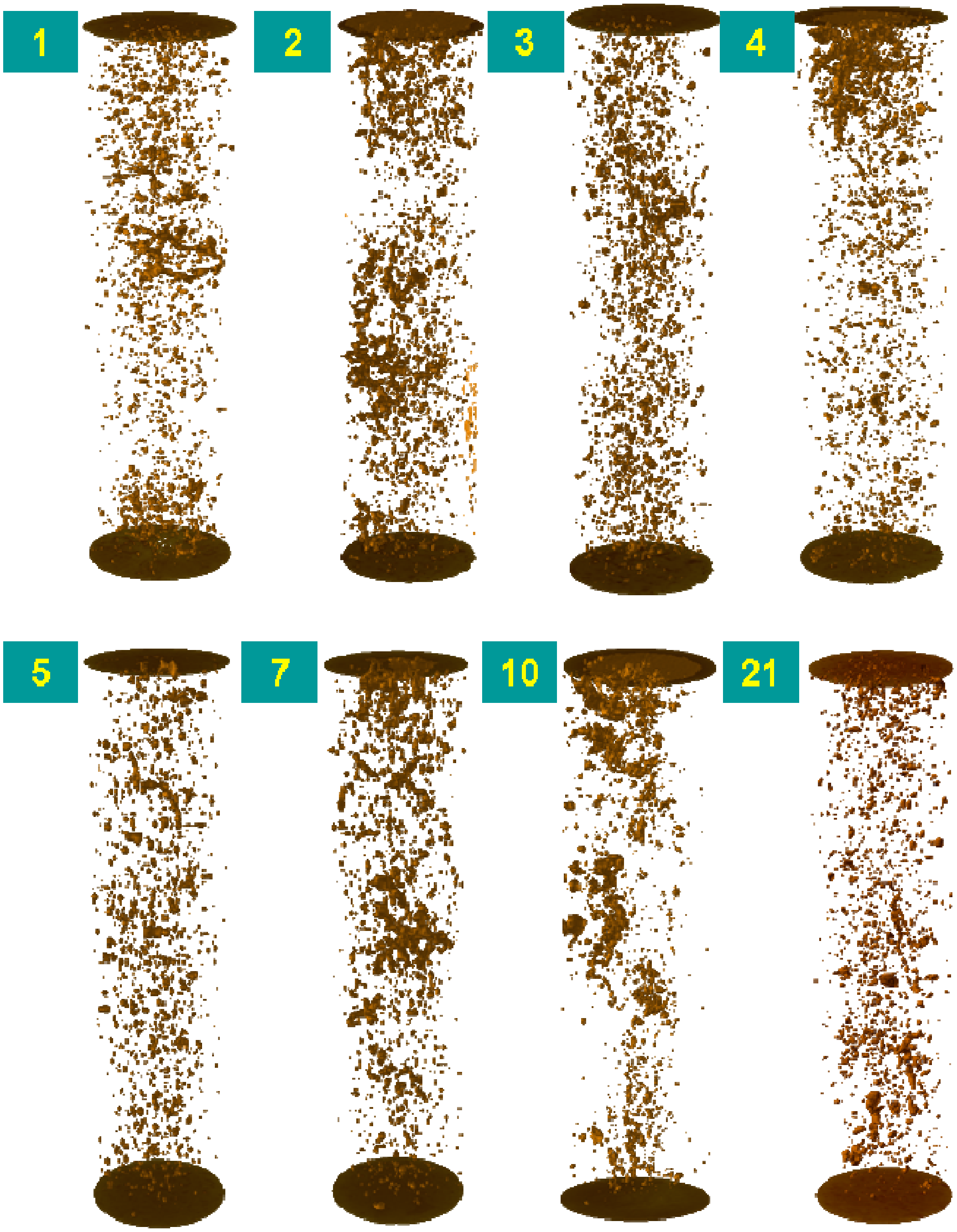

Figure 3. 5 Digitally constructed 3D images of inner structure of the core samples before acidizing (solid parts showing vugs)

One of the techniques used in CT data processing is the image subtraction technique. The core under investigation is scanned at fixed locations prior to the treatment to establish baseline records. After the treatment (acid injection in our study) the core is scanned and the CT signatures of the core are subtracted from the baseline data to quantify the extent of change due to the treatment. In this study, we are interested in the influence of vugs on the wormhole path. Because applying image subtraction method to post- and pre-injection CT images cancels out the vugs we didn't employ this very powerful method. Here this method is mentioned for reference since it is a very powerful method to visualize changes in rock structure during any process. Furthermore this technique can be used to calculate the total amount of rock dissolved in an acidizing experiment.

3.4 CHARACTERIZATION OF CORE LEVEL HETEROGENEITIES: GEOSTATISTICAL APPROACH

Sandstones and carbonate rock invariably have small-scale heterogeneities in mineralogy and flow properties that may cause the effects of injected acids to differ greatly from what is predicted by a model based on a homogenous formation.

Matrix acidizing of carbonates is dominated by the wormholing process, the creation of large flow channels in the rock. It is almost certain that the wormhole pathway through the matrix follows local high permeability pathways. The effect of small-scale heterogeneity is not well studied, both experimentally and in modeling side.

In this study heterogeneity of the core samples were characterized with X-ray CT scans using resolution of 0.3x0.3 mm. This scanner can be used to scan a maximum diameter of 48 cm with a maximum scan time of 4 sec per scan. Using the detailed data obtained from the CT scanner, voxel-based porosities were calculated using Eqs. 2.3, 2.4, and 2.5. This processed data was then used for geostatistical characterization of the core samples.

We used two measures of heterogeneity. A static measure often used in describing the amount of variation in a population is the coefficient of variation (*Cv)*,

$$Cv = \frac{\sqrt{Var(k)}}{E(k)} \tag{3.1}$$

Cv expresses the standard deviation as a fraction of the mean (Jensen et. al 2000). For data from different populations or sources (each CT slice), the mean and standard deviation often tend to change together such that *Cv* remains relatively constant. Any large changes in *Cv* between two samples (CT slices) would indicate a dramatic difference in the populations associated with those samples.

The *Cv* of each slice was calculated and plotted against axial distance along the core. This plot gave us insight about the change in heterogeneity along the core. The results are summarized in **Table 3.2**. **Fig. 3.6** shows the spatial variation of *Cv* throughout the core samples.

Table 3.2 Geostatistical characterization results of CT monitored experiments

		Vuggy porosity %						
ID	**Vuggy porosity %**	**Separate**	**Touching**	**k, mD**	**Corr._main***	**Corr._x***	**Corr._y***	**Coef.Variation****
BC1	17	100	0	2.5	0.20	0.42	0.42	0.43
BC2	23	100	0	1.5	0.18	0.41	0.40	0.43
BC3	22	100	0	1.3	0.17	0.40	0.40	0.42
BC4	13	100	0	1.7	0.17	0.42	0.41	0.11
BC5	10	100	0	2.2	0.36	0.43	0.42	0.42
BC7	8	100	0	1.8	0.19	0.40	0.41	0.45
BC10	7	100	0	23.3	0.20	0.41	0.41	0.36
BC21	11	100	0	25.6	0.19	0.38	0.34	0.41
BC22	11	100	0	2.2	0.20	0.39	0.36	0.45

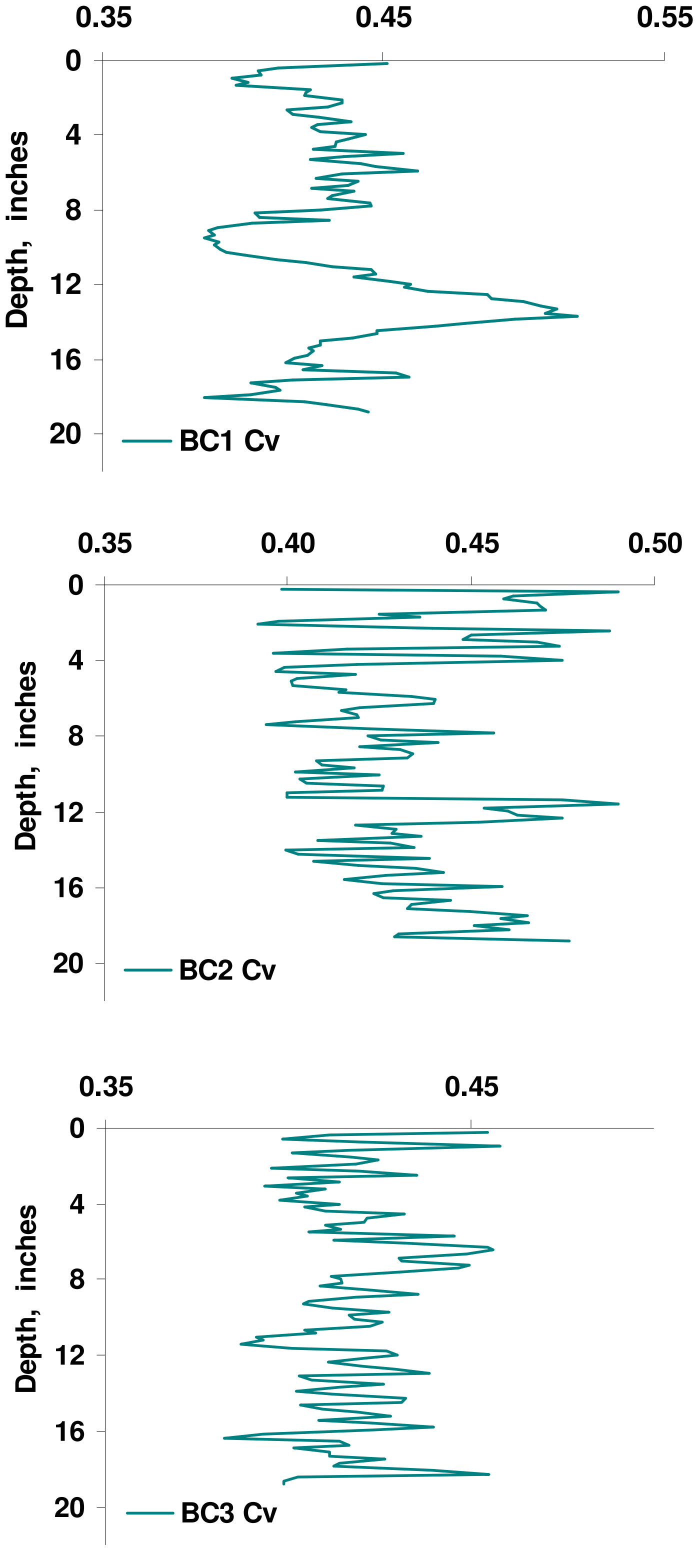

Figure 3. 6 Variation of coefficient of variation throughout the core

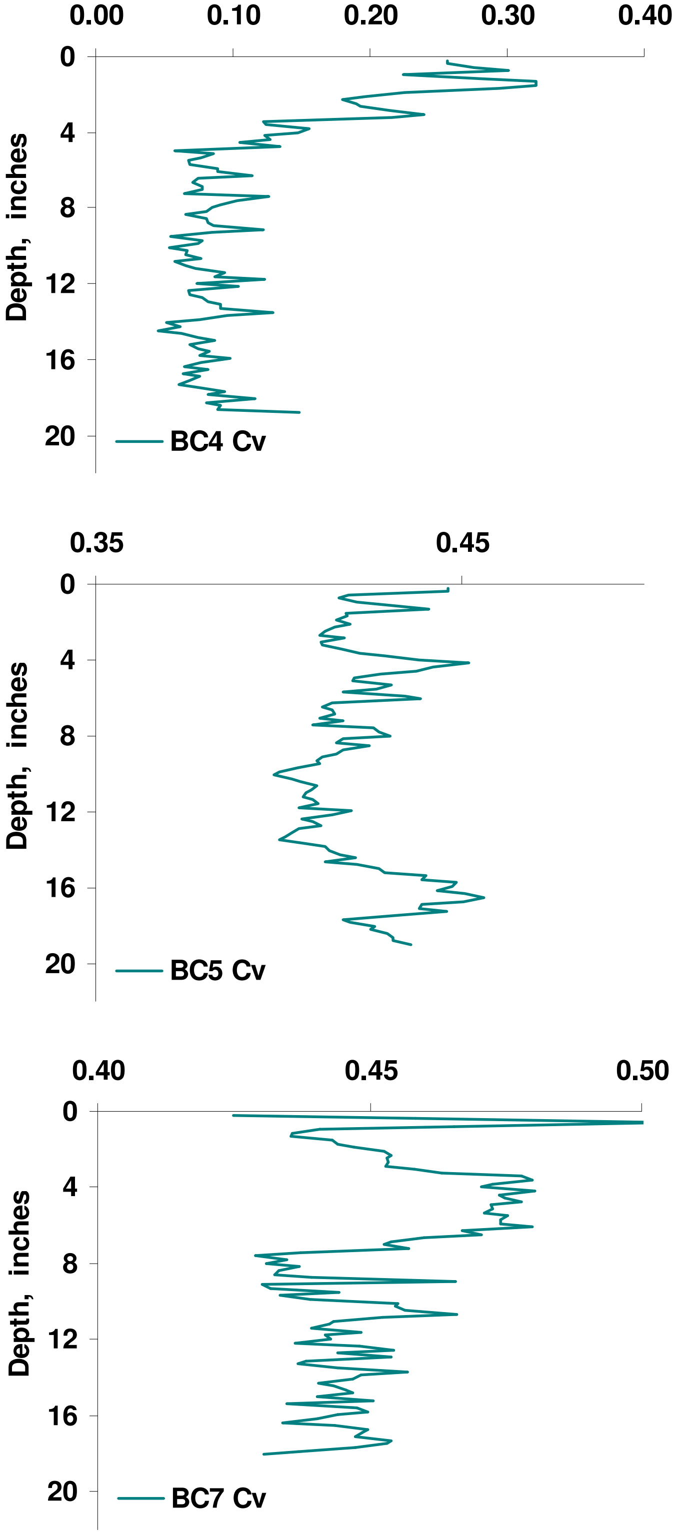

Figure 3. 6 cont.

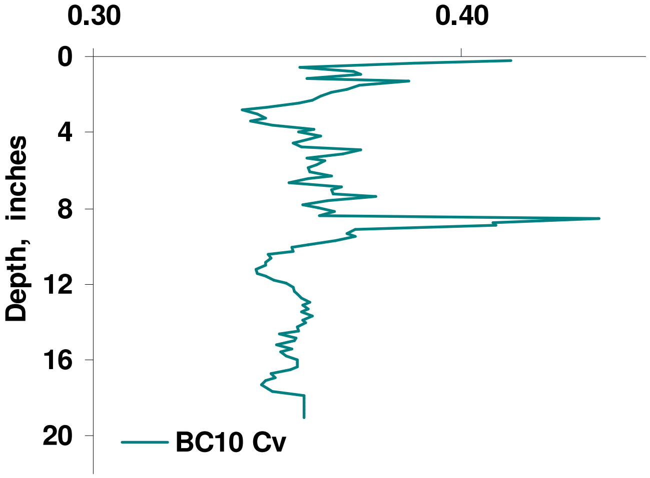

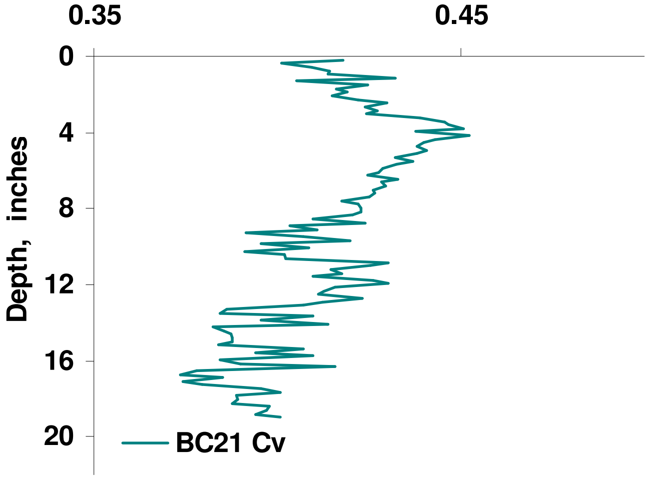

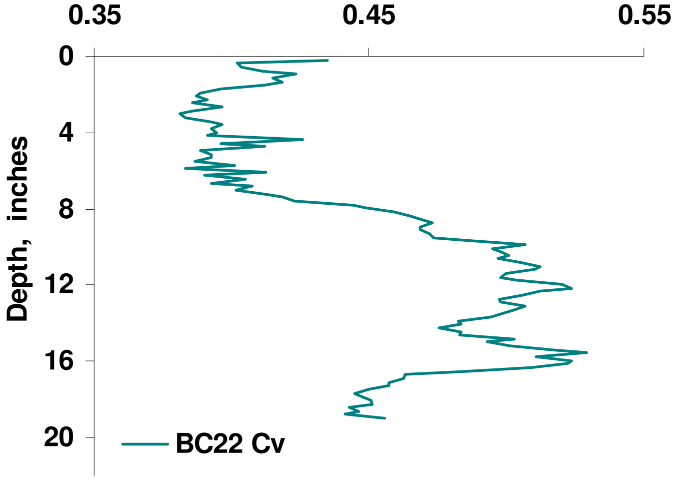

Figure 3. 6 cont.

Although *Cv* gives a general idea about the degree of the heterogeneity of the domain studied, it does not bring any information about the directional variability and spatial correlation (of porosity). To determine the variation of spatial randomness, we use another geostatistcal measure known as variaogram.

The bivariate equivalent of a histogram is a scattergram, where each data pair (x_i,y_i) is plotted as a point **(Fig. 3.7).**

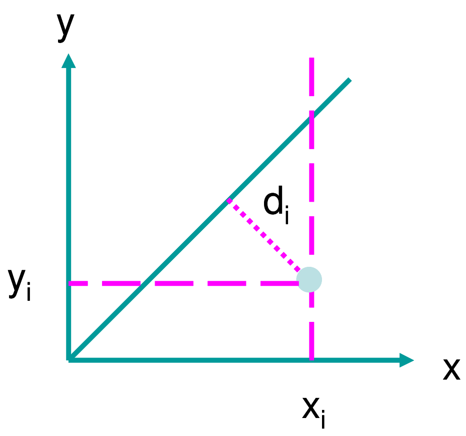

Figure 3. 7 Pair (x_i,y_i) on a scattergram

The degree of the dependence between two variables X and Y can be characterized by the spread of the various scattergrams around any regression line, with perfect linear dependence corresponding to all experimental pairs (x_i,y_i), i=1,……,N plotting on that line. The moment of inertia of the scattergram around e.g. the 45° line would be a characteristic of lack of dependence (Isaaks and Srivastava 1989).

$$\gamma_{XY} = \frac{1}{N}\sum_{i=1}^{N} d_i^{\,2} = \frac{1}{2N}\sum_{i=1}^{N}(x_i - y_i)^2 \tag{3.2}$$

This moment of inertia is called the "semi-variogram" of the set of the data pairs (x_i,y_i). For a domain containing data points (CT data), by changing the separation distance we obtain pairs separated by distance "h", call x_i and x_{i+h}. Generating scattergram for different lag distances h, calculating corresponding semi-variograms and plotting the results we obtain the variogram function **(Fig. 3.8).**

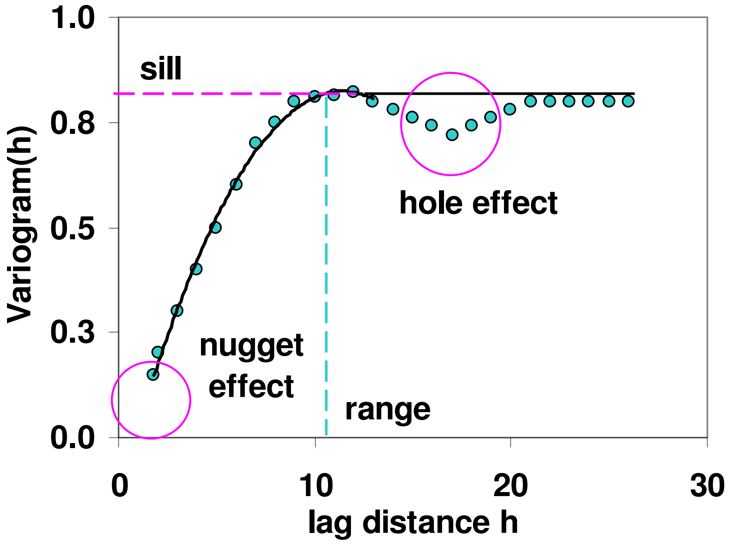

Figure 3. 8 Schematic illustration of concepts used in variogram analysis

A series of h-scatterplots, the variogram function provides the most complete description of spatial continuity by introducing how spatial continuity changes as a function of distance and direction. Before introducing the methodology we followed it is appropriate to introduce at this point some terminology that is used to describe the important features of the variogram (Isaaks and Srivastava 1989).

Range: As separation distance between pairs increases, the corresponding variogram value will also generally increase. Eventually, however, an increase in the separation distance no longer causes a corresponding increase in the average squared difference between pairs of values and the variogram reaches a plateau. The distance at which the variogram reaches this plateau is called the range.

Sill: The plateau where the variogram reaches at the range is called sill.

Nugget effect: Through the value of the variogram for h=0 is strictly 0, several factors, such as sampling error and short scale variability, may cause sample values separated by extremely small distances to be quite dissimilar. This causes a discontinuity at the origin of the variogram. The vertical jump from the value of 0 at the origin to the value of the variogram at extremely small separation distances is called nugget effect.

Tolerance: The problem we may encounter when we try to construct an h-scatterplot from a sample data set is that for any *h* we choose there is enough randomness in our sample locations that very few pairs of samples are separated exactly by *h*. Thus, we have to tolerate this inevitable randomness and accept any pair whose separation is close to *h* on our h-scatter plots. In practice, we specify tolerances both on the distance of h and on its direction.

Omnidirectional variogram: One typically begins the analysis of spatial continuity with an omnidirectional variogram for which the directional tolerance is large enough that the direction of any particular separation vector becomes unimportant.

Variogram model fitting: For a variogram model to be valid, the variogram estimator should be negative-definite. Absence of this property can result in negative mean-squared errors of prediction, which is not acceptable. So, well-known models, such as exponential, Gaussian, spherical, etc., are used for fitting the variogram.

Curious readers should refer to Isaaks and Srivastava (1989), Gringarten and Deutsch (1999), Cressie (1993), and Jensen et. al (2000) for further reading on spatial data analysis.

Using variogram function in conjunction with the CT data we calculated the variogram range of porosity. Dividing variogram range by the length of the cores we obtain the correlation strength (**Table 3.2**). In practice tolerance in both direction and distance is used. Angular tolerance of 45° was used in the analysis, whereas 1 mm tolerance in distance was used. Our analysis started with an omni-directional variogram followed by a directional variogram. Omni directional variogram serves as a useful starting point for establishing some of the parameters required for sample variogram calculations as proposed by Isaaks and Srivastava (1989). Since direction is not a parameter in an omni-directional variogram, we concentrated on finding the distance parameters that produce the clearest structure.

The importance of the correlation length of distribution of vugs is made clear in **Chapter V.** Here we will follow a simpler logic. If the vugs are aligned along the main flow path, injected fluid (reactive or non-reactive) would propagate faster in the domain. Aligned vugs will lead to a variogram function having a large correlation strength. Put an other way, the larger the correlation strength obtained from the variogram study, the easier for fluid to breakthrough at the outlet. This can also be represented by slow and fast streamlines as Moctezuma-Berthier (2000) discussed **(Fig. 3.9).**

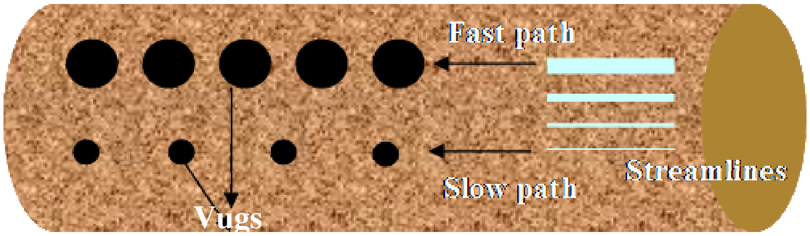

Figure 3. 9 Larger vugs and/or smaller distance between vugs compared to large distance between vugs and/or smaller vugs (bottom). Corresponding streamlines showing small and fast flow path

A core plug is a 3D domain. So, the spatial correlation in each direction should be analyzed. For this purpose we conducted variogram studies on x, y (secondary flow paths) and z (primary flow path) directions. For the main flow direction (z) pseudo tubes were defined as given in **Fig. 3.10.** Using the average data along these 1D tubes spatial continuity in the main flow direction was determined. The number of these pseudo tubes was determined by the degree of heterogeneity of the rock after primary visual observation.

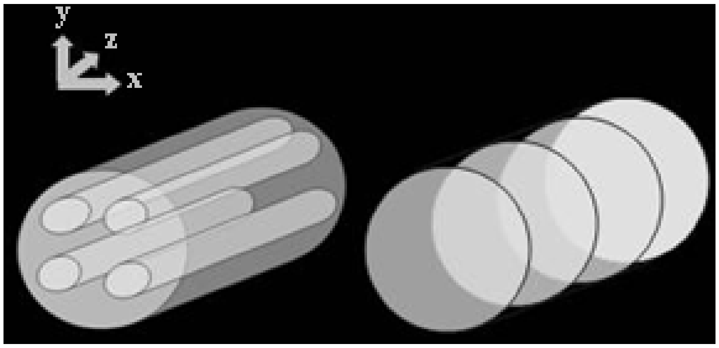

Figure 3. 10 Pseudo tube concept and lateral CT slices for varigoram interpretation

The variogram is a measure of variability; it increases as samples become more dissimilar. The correlation strength is the ratio of the range to the total length of the core (1 is the maximum). The variogram ranges of the samples were determined to be in the range of 3.4-7.2 inches. This means that the vugs are not randomly distributed in the core samples; on the contrary they are spatially correlated (up to variogram range value). To clarify, in the case of randomness the range would be close to zero; on the other hand if the samples (for example vugs) are close to each other and/or following a definite lateral pattern the range would be higher. In the extreme case of layering, fluid would by pass other parts and flow through the most permeable layer and the range is close to the core length.

Individual slices along the cores were analyzed to detect the spatial continuity in x-y plane. CT data is first converted to bulk density (or pseudo bulk density), then to point-wise porosity field using Eqs. 2.3, 2.4, and 2.5. After obtaining the experimental variogram model, correlation strength of the data was determined. Given in **Table 3.2** is the average correlation strength in the main and secondary flow paths.

3.5 CHARACTERIZATION OF VUGGY POROSITY

For highly vuggy samples, it is crucial to understand the contribution of vugs to flow, and thus propagation of a tracer or acid. The geometries, locations and connectivities of vugs greatly affect the flow in reservoirs. As discussed above, vugs can be classified as touching, or separate vugs. One could add one more terminology as dead-end vugs. These are the vugs connected to other vugs, but because they are diverting the fluid from its main flow path, their contribution to total flow is less. So in order to distinguish touching vugs with these vugs we will stick to the term dead-end vug.

A well-known visualization technique named connected component labeling (CCL) was implemented in the 3D domain in order to understand the connectivity, and thus the contribution of vugs to flow of the fluid through the sample. In a highly crowded CT data set **(Fig. 3.11)** it is difficult to see the connections between of vugs. The CCL algorithm enabled us to detect the biggest vugs, as well as the connections between vugs.

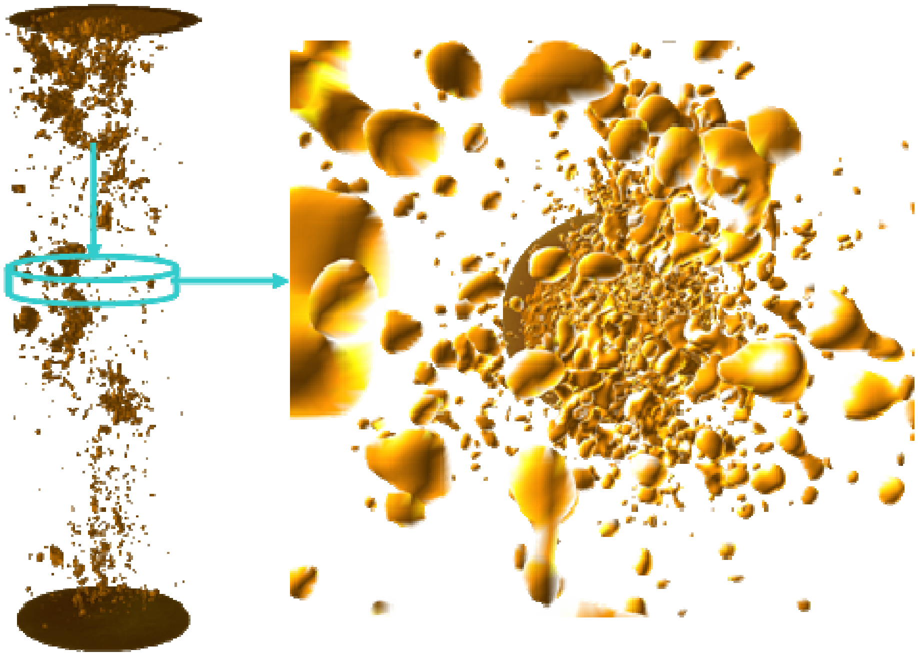

Figure 3. 11 3D (left) constructed image of a core sample showing the heterogeneity of the sample studied, and cross sectional view from top (right)

A common use of connected component labeling is in image analysis for computer vision and image understanding. The CCL algorithm is usually applied on a binary image with two types of pixels. These binary images are usually produced from another image processing step. In the binary image, the two types of pixels are usually referred to as object pixels and background pixels. An object pixel may indicate something of interest, such as a potential tumor in a medical image or a flame in a combustion simulation. These object pixels form objects to be labeled. In the scope of this study, for our vuggy samples we are interested in matrix cells and vug cells in the data obtained from the CT scanner. So the domain of interest is converted to binary data by giving 0 to matrix cells and 1 to vug cells. Then the CCL algorithm was employed in the 3D region of interest in order to find the connected vugs. CCL works by scanning from inlet to outlet of the core, pixel-by-pixel in order to identify connected pixel regions. The algorithm scans the domain by moving along a row until it comes to a point X (where X denotes the pixel to be labeled at any stage in the scanning process) for which the original label is 1 (vug cell). When this is true, it examined the four neighbors of X which have already been encountered in the scan. Based on this information, the labeling of X occurs as follows: i) if all four neighbors are originally labeled 0, assign a new label to X, else ii) if only one neighbor has label 1, assign its label to X, else iii) if more than one of the neighbors have label 1, assign one of the labels to X and make a note of the equivalences. After completing the scan, the equivalent label pairs are sorted into equivalences classes and a unique label is assigned to each class. As a final step, a second scan is made through the image, during which each label is replaced by the label assigned to its equivalence classes. **Figure 3.12** illustrates this concept. The first image shows the raw image. In this image, white grid blocks are representing the background object, matrix; wheras the black regions represent the vugs. The second image represents the domain while the CCL algorithim is running. Note that at this stage of the process, the CCL algorithm detects three separate objects, letters “S”, “P”, and “E”. Finally, the completely processed image can be seen in the last image. Here, the CCL algorithm successfully detects three different objects, and labels all corresponding grid blocks.

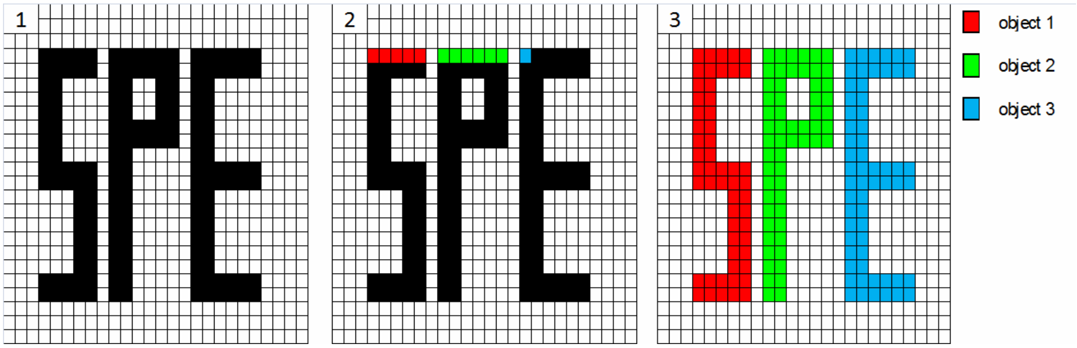

Figure 3. 12 Illustration of CCL algorithm: 1) raw image, 2) image while processing, and 3) final image

In order to illustrate the power and usefulness of the developed 3D CCL algorithm, a 15x5x7 inches piece of carbonate rock was scanned **(Fig. 3.13)**. The processed CT data was imported to the developed code.

In this sample, the CCL algorithm detects two connected vug networks and many separate vugs.

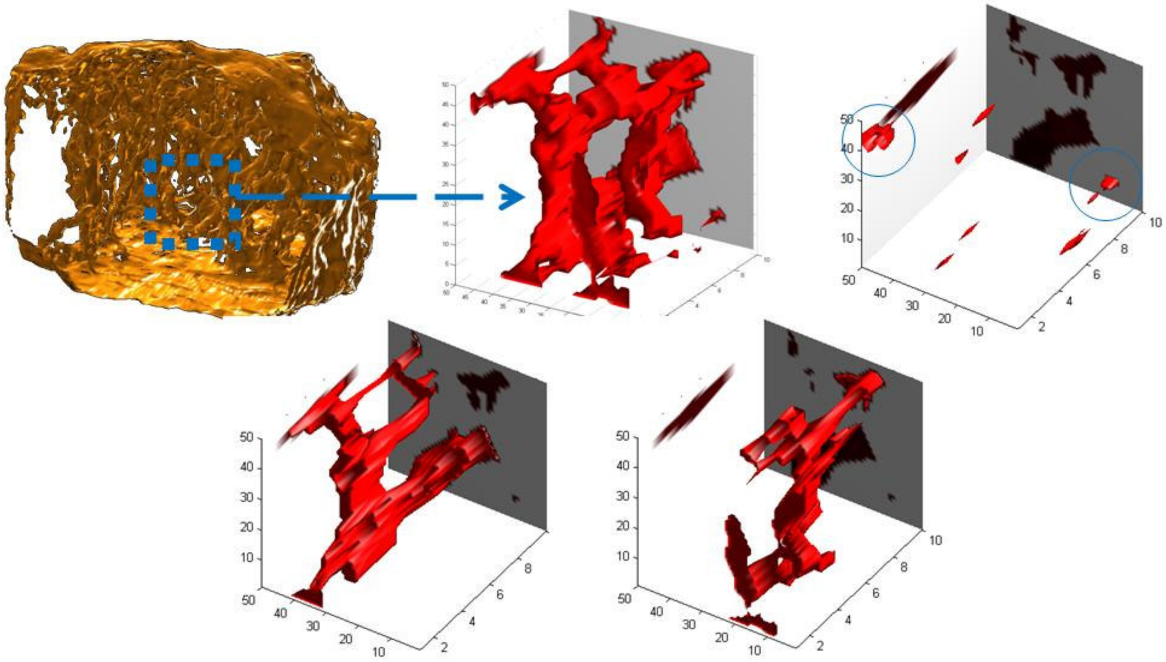

Figure 3. 13 Application of the CCL algorithm on a vuggy rock. From upper left to bottom right: inner structure of the vuggy rock (solid parts are matrix and void parts are vugs), extracted portion of the rock, separate vugs and two vug networks detected by CCL in the region

After verification of the CCL algorithm using this chunk of rock, the algorithm was implemented on the core samples to be acidized.

The final output of employing the CCL algorithm on a sample is the domain consisting of matrix cells, vug network(s), and separate vug(s). This novel application enables us to detect different types of vugs in a highly noisy data set obtained from the CT scanner. It was observed that none of the samples studied in this study has any touching vug network (**Table 3.2).** On the other hand, some relatively big vugs were detected by CCL algorithm. The algorithm finds some connected vugs which are not easy to be detected by the naked eye in a crowded data set. The effect of these relatively big vugs will be discussed in the "experimental results" section. Effects of connectivity of vugs on flow and transport are discussed in the modeling part as well.

3.6 CHAPTER SUMMARY AND OBSERVATIONS

The core samples were geologically classified, then later characterized using the CT scanner in conjunction with the geostatistical functions. A complete work flow was developed from core preparation to 3D CT model construction. The power of this new workflow was demonstrated using different set of data from sandstone acidizing to acid jetting and acidizing core floods experiments (**Appendix B, and C**)

While 3D constructed models give a qualitative insight about the cores studied, geostatistical functions add quantitative measures for the degree of the heterogeneity. Calculated high and varying coefficient of variation of porosity indicates that the number of the vugs is changing from one slice to another. On the other hand, high correlation lengths observed in the samples dictates that the vugs are not randomly distributed; indeed, they are spatially correlated. We will investigate the effect of this analysis on experimental results in the upcoming chapter.

CHAPTER IV

EXPERIMENTAL WORK

Conducting acidizing core flood experiments has been of the main practices to understand wormhole formation and propagation. It has been studied by several researchers for years. In these experiments different systems were studied to understand the wormholing phenomenon. The effects of some parameters were investigated. Among them, the HCl/limestone system is the one most studied. Salt pack/under-saturated salt solution system was introduced as an alternative to study the same problem. The common point of previous studies is presenting *PVbt* (pore volume to breakthrough) as a function of injection rate or interstitial velocity given as:

$$u_i = \frac{q}{\pi r_{core}^2 \phi} \tag{4.1}$$

The important parameters that affect wormhole creation and propagation can be summarized as:

1. Heterogeneity and spatial distribution of mineralogy and petrophysical properties
2. Acid concentration and effective acid diffusion
3. Acid-rock reaction rate
4. Acid injection rate
5. Wetted surface area, existence of natural fractures
6. Acid rheology, dissociation constant (for weak acids)
7. Acid types: emulsified, foams, in-situ viscosified acids
8. Acid additives, and their effect on effective reaction rate and wettability
9. Fluid loss in wormhole

10. Tip splitting

Because of the unstable nature of the process, dissolution type can change from one practice to another. Huang et al. (2000) show the importance of two parameters among others: fluid loss and reaction rate.

The instability is a consequence of the coupled nature of flow and reaction common to all mass transfer limited dissolution processes since the dissolution rate depends on the local fluid rate. Simply, while porosity increases by dissolution, local fluid rate decreases as a consequence of pressure drop behavior. This reduction in local velocity results in local dissolution which does not contribute to propagation of wormhole. In this regime conical wormholes were observed **(Fig. 1.2).** On the other hand, at high injection rates or local velocity because of the high pressure, injected fluid tend to move into the matrix from wormhole. In that case high filtration occurs at the wormhole wall and tip, resulting in branching. Different types of dissolution regimes were proposed by previous investigators (Daccord 1987., Fredd and Miller 2000).

The major findings of the previous studies can be summarized as:

1. The optimal conditions for wormhole formation depend on acid/mineral reaction kinetics, diffusion coefficients of acid species, concentration of acid, temperature and geometry of the system.
2. Fluid loss, and differences observed between acidization of dolomite and limestone is not well understood. It is well-known that the reaction rate of HCl-limestone is greater than that of HCl-dolomite system.
3. The dissolution structures can be collected under 5 different regimes as: Face dissolution, conical wormholes, dominant wormholes, ramified wormholes, and uniform dissolution (**Fig. 1.2**).
4. Transition between these dissolution regimes can be represented by two dimensionless numbers: Damkohler and Péclet number.

In this study we focused on a relatively virgin area: the effect of heterogeneity in matrix acidization of carbonates.

Acidization of vuggy carbonates was studied in a total of 16 experiments. Acid core-flood experiments were conducted using 4x20 inches carbonate cores. The details of the samples studied, the experimental conditions, and the results are given **in Table 3.2**, and **Table 4.1**.

The originality of our experiments is the use of relatively large samples (4-inch by 20-inch). The benefit of using bigger cores is to reduce the geometry effect on wormhole propagation. Clarifying, the core plugs used in the experiments are confined domains. Confining boundaries created a pressure field in such a way that to limit the wormholes' freedom of movement in secondary flow directions. Great majority of the experimental results reported in the literature presented a dominant wormhole. These laboratory results are typically represented as the volume for breakthrough normalized by the pore volume versus the injection velocity. In other representations, the flow rate may be replaced by the Péclet number or the inverse of the Damköhler number. It is often suggested that the optimum conditions for the field are close to the minima of these curves. However, the core geometry can change drastically the dissolution patterns and therefore the optimum conditions. In the case of a fractal behavior, dissolution patterns would be scale-dependent, and so the optimum conditions.

4.1 EXPERIMENTAL SET-UP

A simple schematic of the set-up is given in **Fig. 4.1**.

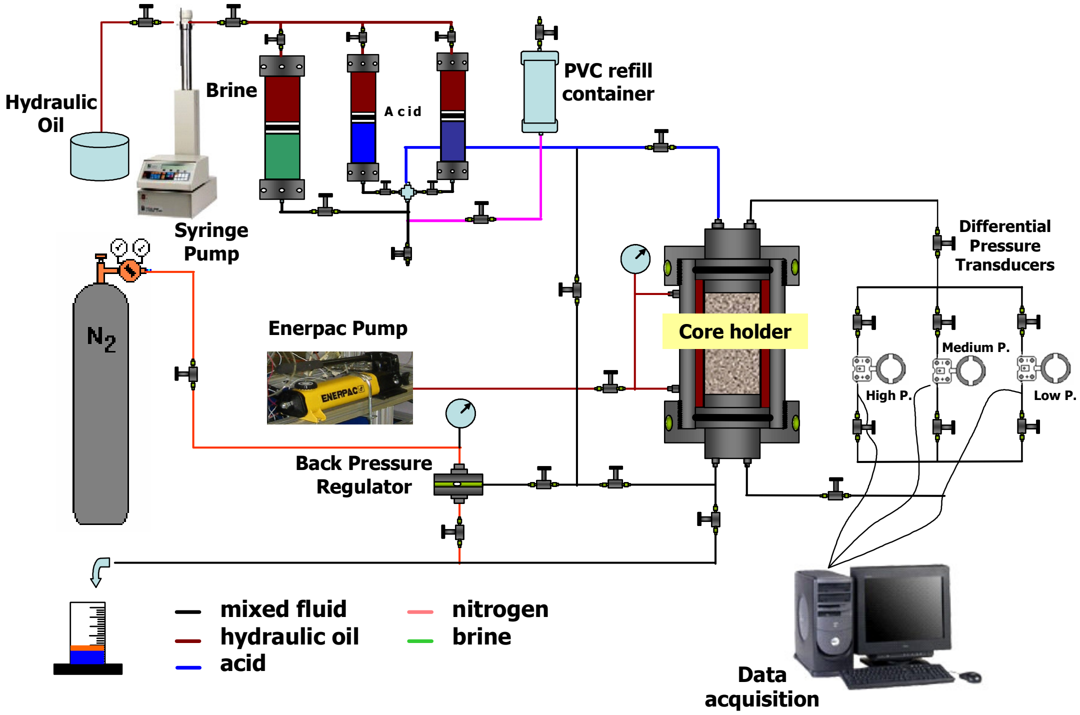

Figure 4. 1 Schematic of the experimental set-up used in acid core-flood experiments

Previously prepared brine and acid stored in the accumulators. The core sample is confined inside the core holder with a Viton sleeve by a hydraulic pump. The back pressure provided by nitrogen supply maintains the CO_2 in solution.

During the matrix acidizing experiments, the flow rate, temperature, confining pressure (overburden), and back pressure are set and maintained constant; the differential pressure across the core during the process is measured by analog pressure transducers and recorded by the LabView software to construct and analyze the acid response curve. All the equipment reside inside a laboratory exhaust system to vent the acid fume.

The details of the set-up were presented by Nevito (2006).

4.2 EXPERIMENTAL PROCEDURE

The cores were weighed for porosity calculation. The cores then were vacuum-saturated with brine using a sealed PVC container and a vacuum pump. Saturated cores were again weighed to calculate the porosity and were then placed in a standard Hassler core holder. During the coreflood and acidizing processes, the overburden pressure was kept at least 300 psi above the initial core inlet pressure so that the fluid did not bypass the core. The desired fluid was stored in an accumulator and was injected at the desired rate using Isco model 500D and 1000D syringe pumps. When the pressure drop across the core stabilized, the core's permeability was calculated using Darcy's Law and known values for pressure drop, flow rate, viscosity, and core geometry. Pressure drops were monitored using differential pressure transducers with varying ranges. The data were recorded using a data acquisition system and commercial software (LabView) on a personal computer. Acid used was 15% (by weight) HCl, and experiments were conducted at room temperature. During the acidizing process, the reacted carbon dioxide was kept in solution with a backpressure of 1000 psi. This backpressure was applied using pressure-regulated nitrogen tanks and backpressure regulators, which did not allow fluid to flow unless the core outlet pressure equaled the applied backpressure. The experiment was terminated when a negligible pressure drop was observed, indicating the presence of a wormhole traversing the whole length of the core. Various flow rates were used to determine the optimal flow rate of the acid; that is, the lowest volume of acid necessary for breakthrough.

4.3 EXPERIMENTAL RESULTS

Experimental results were interpreted by means of pressure drop behavior and comparison of pre- and post-acidizing CT scans. *PVbt* was calculated for each experiment. A study in order to obtain a trend relating geostatistical parameters, vug volume and *PVbt* was conducted. The results were compared and contrasted with the previous studies in which homogenous and small carbonate cores were used.

The results of all experiments are summarized in **Table 4.1**. The details are given in following sections.

Table 4.1 Experimental conditions and results

ID	qinj cc/min	k, mD	*PVbt*	Wormhole type
BC1	12	2.5	0.04	single dominant, 2 significant branches
BC2	12	1.5	0.04	single dominant, some small branches
BC3	12	1.3	0.04	single dominant, some small branches
BC4	8	1.7	0.11	single dominant, 1 significant branch
BC5	8	2.2	0.06	single dominant, no branches
BC6	4	1.9	0.08	single dominant, no branches
BC7	8	1.8	0.08	single dominant, some small branches
BC9	12	8.5	0.09	-
BC10	12	23.3	0.06	single dominant, 2 significant branches
BC11	24	15.0	0.13	-
BC12	24	3.9	0.12	single dominant, some small branches
BC13	12	11	0.15	single dominant, some small branches
BC14	16	17	0.11	single dominant, some small branches
BC15	16	21	0.15	-
BC21	20	25.6	0.08	single dominant, many small branches
BC22	13	2.2	0.08	single dominant, many small branches

4.3.1 Pore volume to breakthrough (*PVbt*) curves

The results from the vuggy carbonate acidizing experiments are summarized in **Table 4.1**. The obvious major finding from these tests is that acid propagates wormholes through vuggy carbonates much more rapidly than occurs in more homogeneous rocks. This is indicated by the very low values of pore volumes to breakthrough observed in all experiments, ranging from a low of 0.04 to a high of 0.15. With a pore volume to breakthrough of 0.04, a wormhole has moved through the core twenty five times faster than a uniform, piston-like displacement front would move. For a wormhole to move through the core so rapidly, the acid must be flowing through only a small portion of the core, guided by the high flow conductivity caused by the presence of vugs.

Another indicator of the manner in which wormholes propagate through a vuggy carbonate rock is the pressure drop response during acid injection. Because the wormholes are so large relative to matrix pore sizes, the pressure drop across the core is almost completely due to the matrix flow ahead of the wormhole. In acidizing experiments with relatively homogeneous carbonates, the Δp across the core often declines almost linearly as the wormhole propagates at a steady velocity through the core.

Fig. 4.2 shows typical Δp behavior from four different experiments with Indiana limestone reported by Wang (1993).

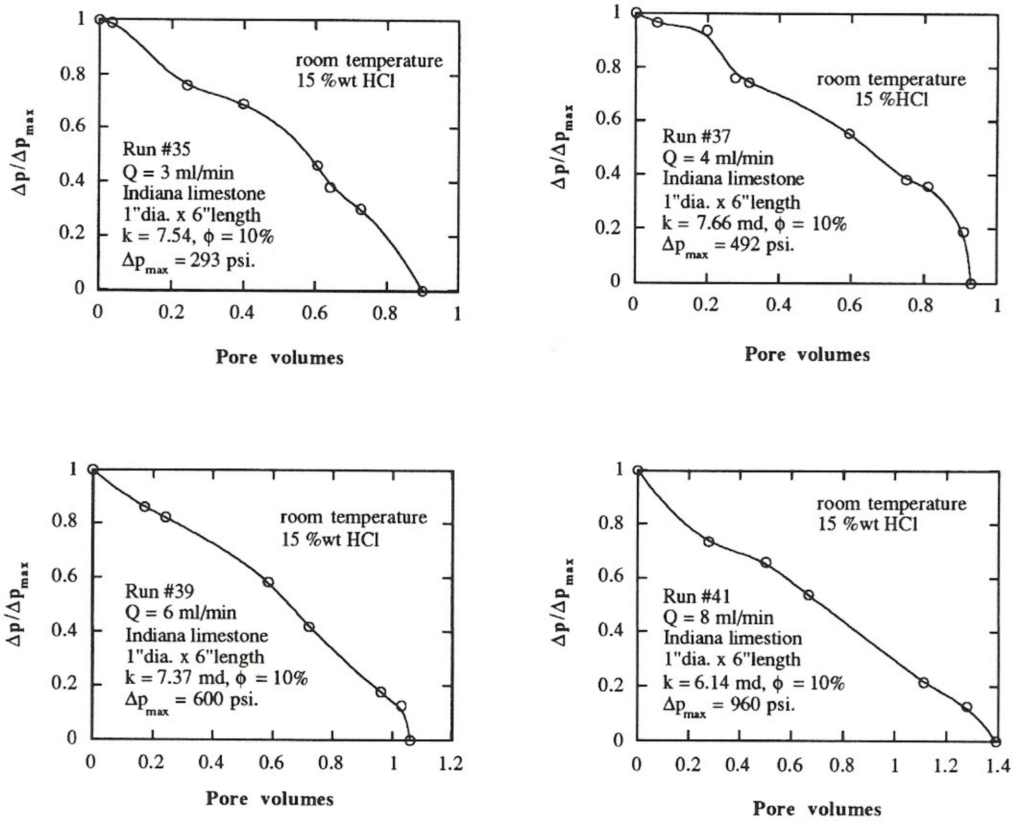

Figure 4. 2 Experimental results reported for homogenous 1-inch by 6-inch carbonate cores (Wang et al. 1993)

In contrast, the pressure drop behavior during acid injection from our experiments is shown in **Fig. 4.3**. In most of the cases the pressure drop remained almost constant for several minutes, dropped sharply for a few minutes, then leveled off again, and finally dropped rapidly to near zero. When the Δp is level or the slope of the plot changes, the wormhole is not propagating axially down the core, so these portions of the pressure record correspond to sections in the core where the wormhole made changes in direction. The periods of rapid Δp decrease are likely a reflection of the acid solution rapidly propagating from one vug to another in a highly vugular part of the core sample.

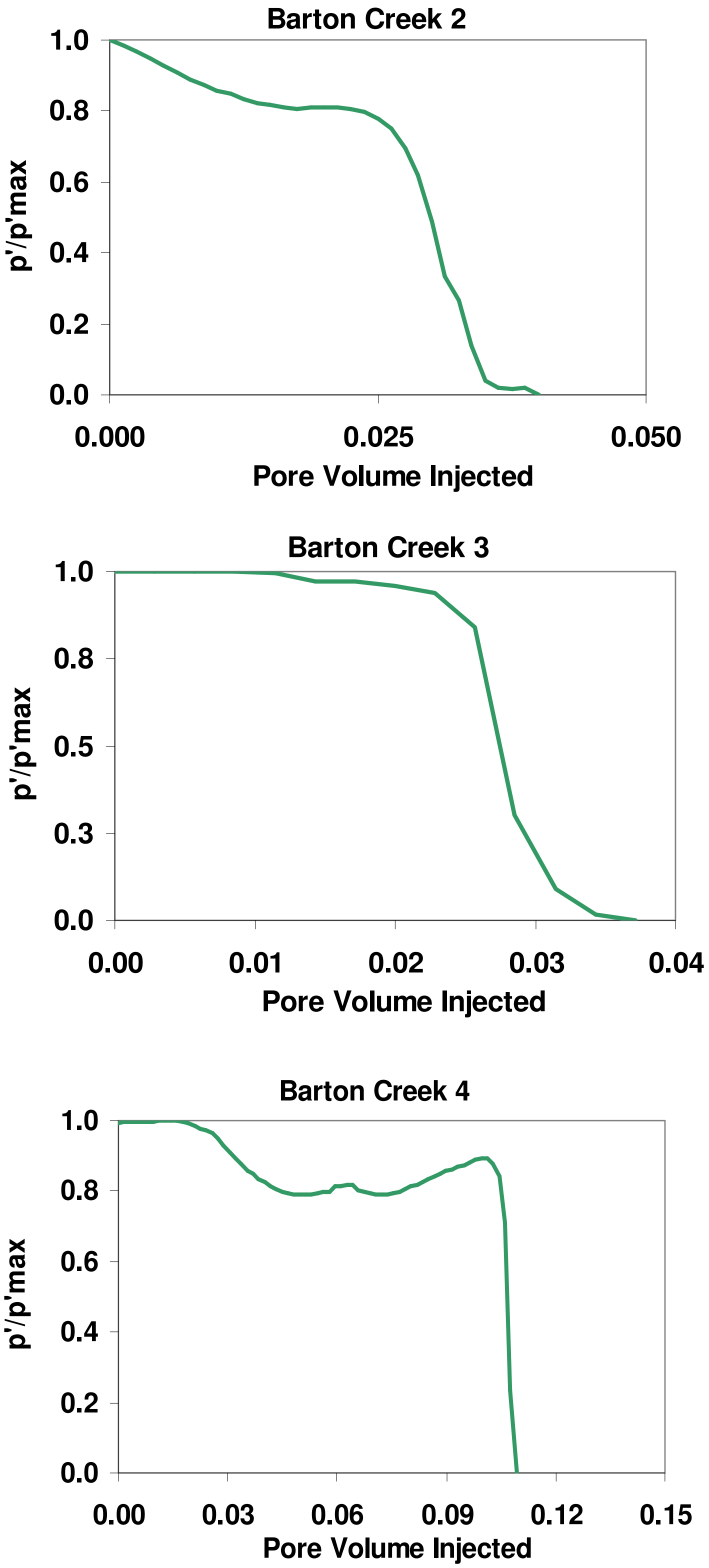

Figure 4. 3 Experimental results with vuggy 4-inch by 20-inch carbonate cores

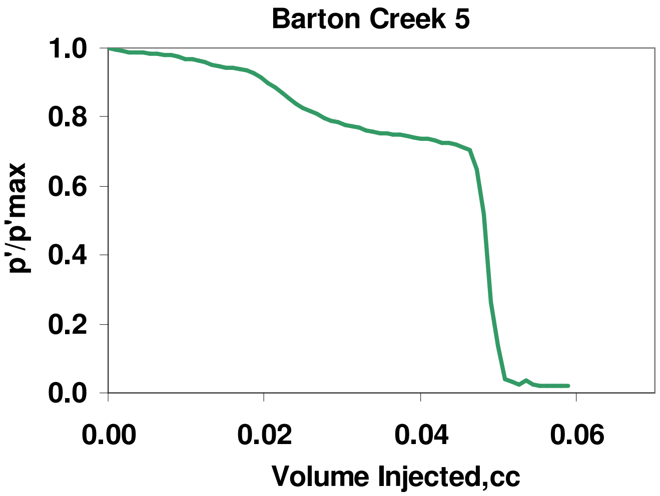

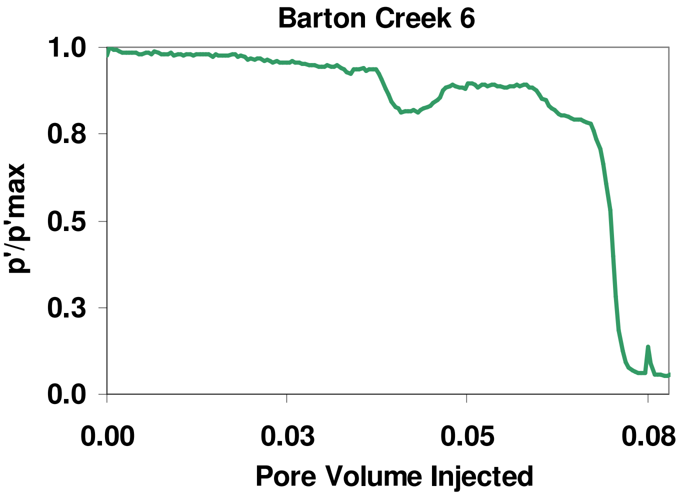

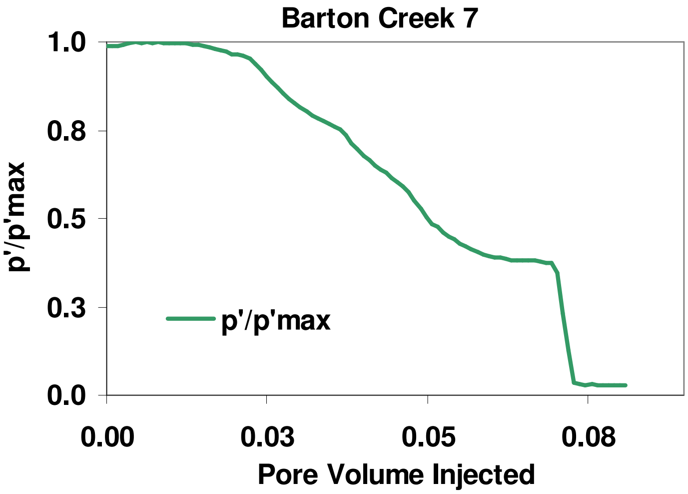

Figure 4. 3 cont.

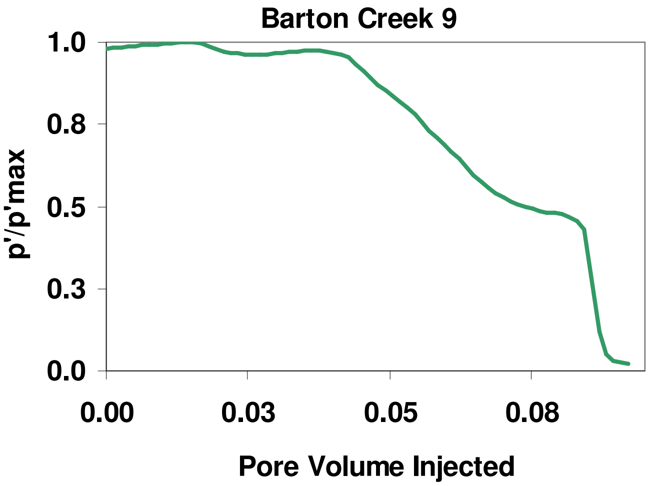

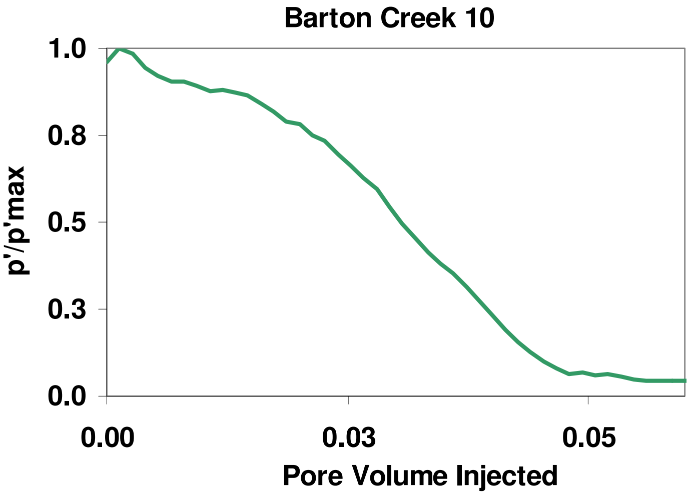

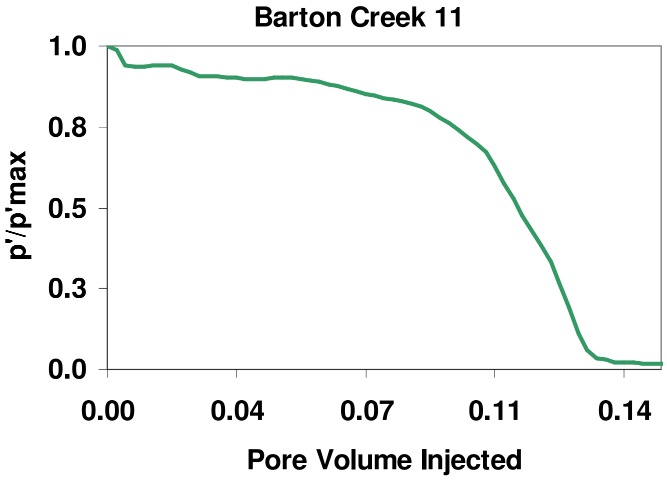

Figure 4. 3 cont.

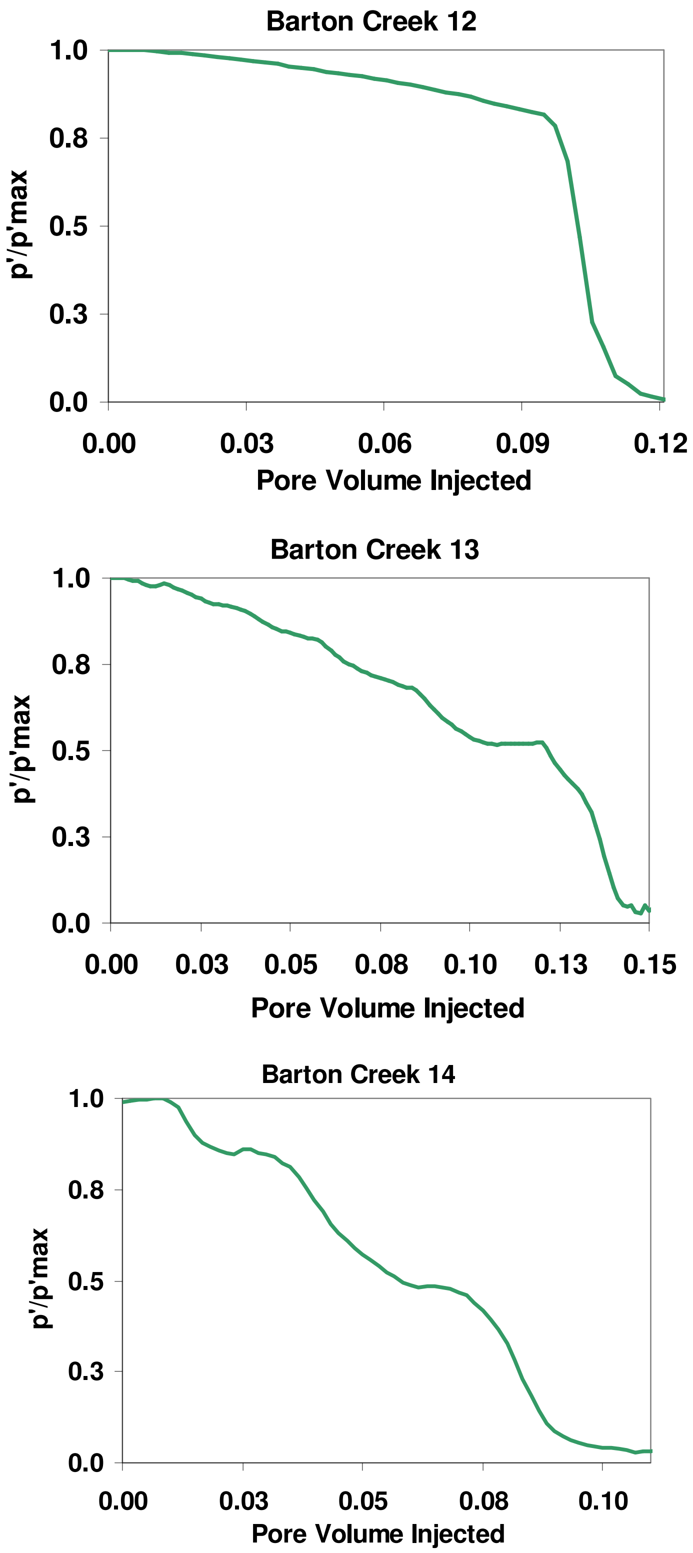

Figure 4. 3 cont.

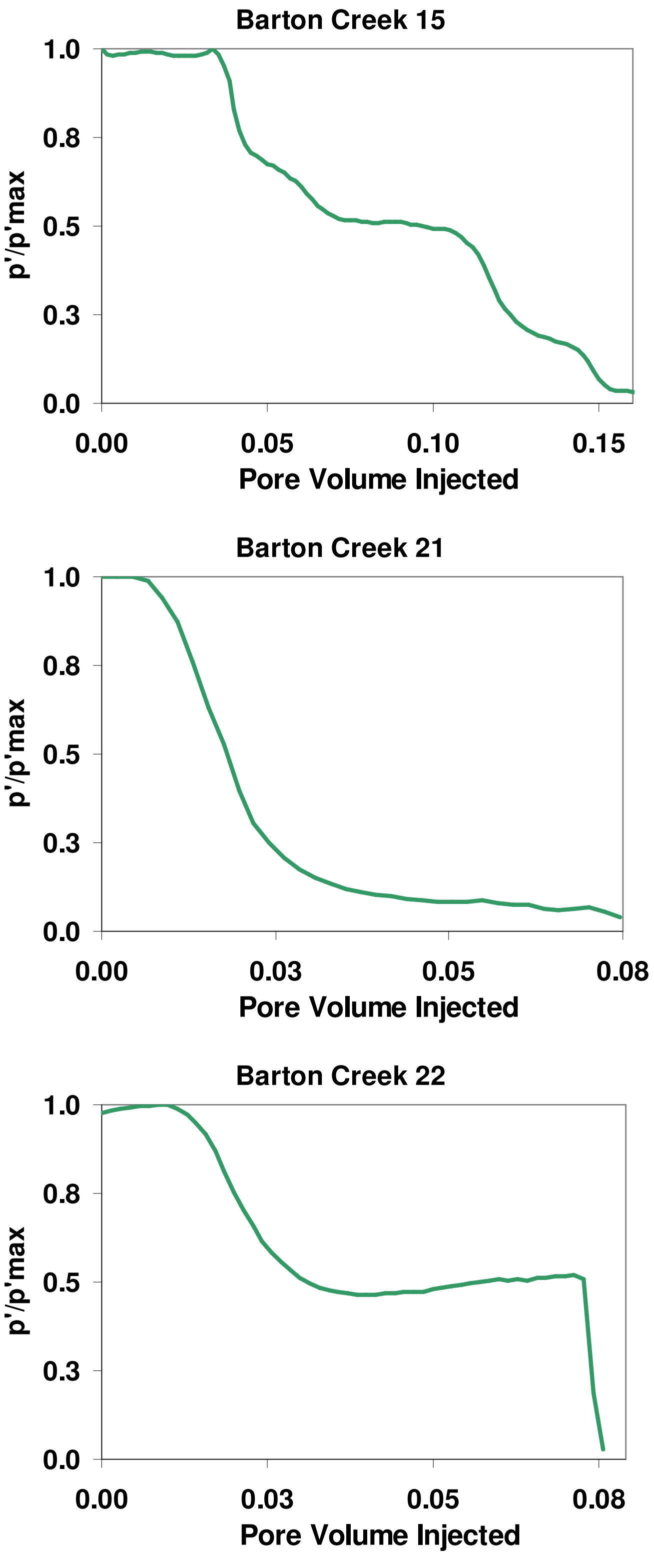

Figure 4. 3 cont.

The dramatic difference between the wormhole propagation behavior in vugular carbonates and numerous previous studies using homogeneous carbonate rocks is illustrated by plotting our results on the pore volumes to breakthrough versus interstitial velocity plot **(Fig. 4.4)** presented by Buijse and Glasbergen (2005). The *PVbt* values for the vugular carbonate experiments are about an order of magnitude lower than those for previously reported experiments for HCl and calcite. Because all of the results shown by Buijse and Glasbergen were for acid concentrations less than the 15 weight % used in our experiments, we also added data from Wang (1993) to the plot to determine if the effects we observe are due to higher acid concentration. This data is from experiments with 15 weight % HCl (4.4 N) in 1 inch diameter by 6 inch long Indiana limestone samples. The Wang data is comparable to the other results with homogeneous rocks.

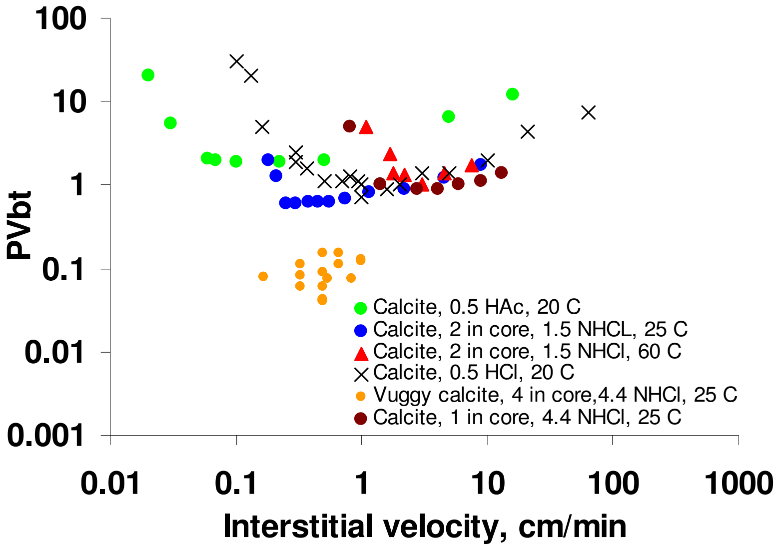

Figure 4. 4 Vuggy carbonate acidizing (this study) and Wang (1993) data on Buijse and Glasbergen plot

We do not have sufficient data from the vugular carbonate experiments to clearly identify the optimal flux for this system. The character of the *PVbt* versus velocity data for these tests suggests that the fluxes tested are above the optimal flux. Apparently, the optimal flux for these vuggy carbonates is much lower than that observed in homogeneous carbonate rocks. This is understandable if the acid is only flowing though a small portion of the rock in the vugular rock case because the interstitial flux for a coreflood is calculated as the injection rate divided by the product of core cross-sectional area and porosity. If the actual cross-sectional area of flow is much smaller than the total core area, the true flux is much higher and may be comparable to that observed on tests with homogeneous cores.

We also plotted the change in *PVbt* as a function of vuggy pore space (**Fig. 4.5**). It is clear from this figure that the presence of vugs contributes to early breakthrough of the acid. We will further investigate this in the numerical modeling part.

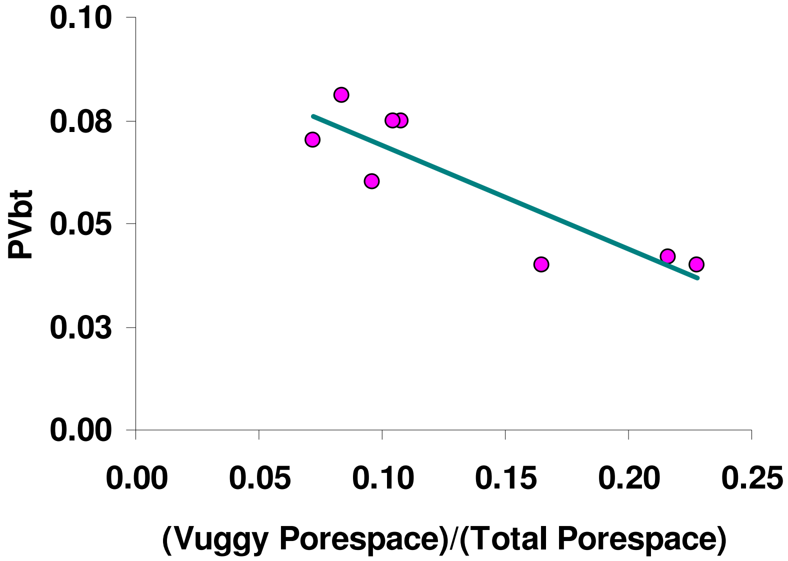

Figure 4. 5 Experimentally observed relation between total vuggy pore space and *PVbt*

Because the calculated directional correlation strengths for all the samples studied are nearly identical we couldn't quantify the effect of correlation strength of vugs on *PVbt*. However it is clear that high correlation strength of vugs contribute to very early breakthrough observed in experiments. We will investigate this point further with the developed model.

4.3.2 Comparison of pre- and post-injection CT scans: Mapping preferential flow path

This study presents a novel workflow for detailed visualization of wormholes via 3D image construction from CT data. The details of the procedure are given in **Appendix A**. Some of the results obtained using the new workflow is presented in **Appendix B** and **C**. Several areas of application from acid fracturing to acid jetting were demonstrated. For this particular work the proposed work flow is used to compare and contrast the pre- and post-acidization inner structure of the cores. Visual description provides an unprecedented description of the effect of acid on the stimulation of heterogeneous carbonates.

The fact that acid channeled through the vugular cores, following the path of the vug system, is supported by the CT scans of the cores before and after acid injection. **Figure 4.6** compares the CT scans before and after acid injection for some of the samples. In these images, the dark color indicates the large voids in the core, either vugs before acid injection or vugs and wormholes after acid injection. The wormhole created by the acid passed through all of the largest vugs, following the most conductive flow path through the core. Most of the core was virtually untouched by the acid, resulting in the very low pore volumes to breakthrough.

Inspired from the post-injection results we focused on a deterministic approach to develop a theory on preferential dissolution of vuggy carbonates. First, the cores were CT-scanned to characterize the spatial correlation of vuggy pore space. The biggest vugs in each CT slice were found and connected to the nearest biggest vug in the next slice. By this method, the “most easy to flow through path(s)” were determined. The results were later compared with the actual wormhole path visualized following the core-flood acidizing. Some results, chosen among seven CT monitored cases, were reported below with the visual representations given in **Fig. 4.6**. In a great majority of the experiments we were able to predict the wormhole path by just combining the biggest and closest vugs in each slice.

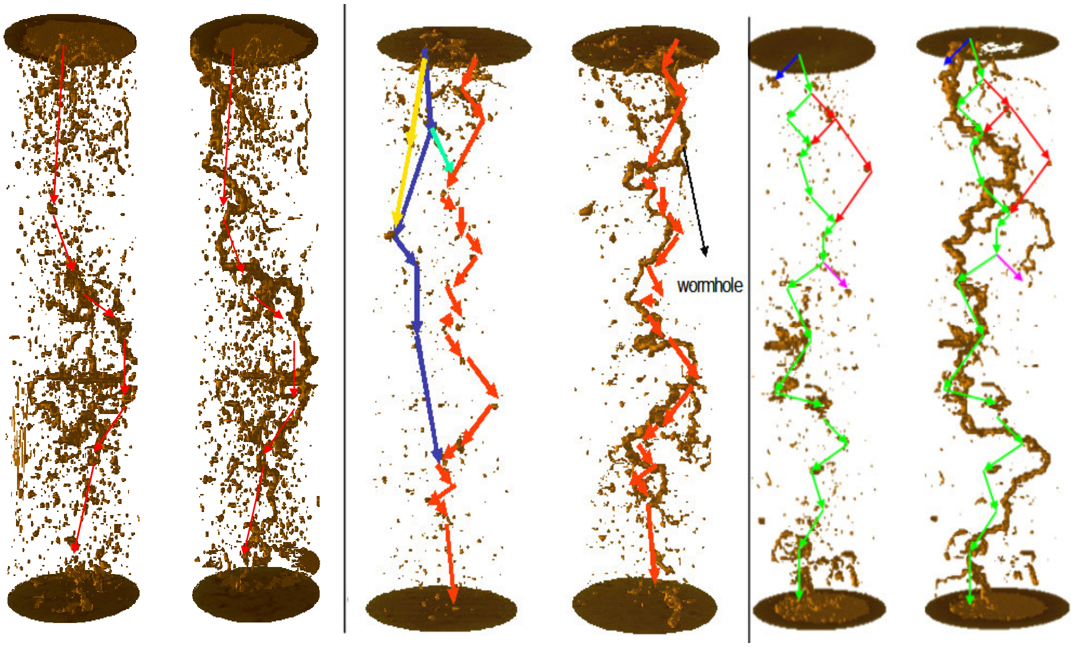

Figure 4. 6 CT derived distribution of vugs and preferential flow paths (left, color arrows) compared to actual wormhole paths (right)

For some of the samples studied, multiple preferential flow patterns were generated from the initial vug distribution. Acid's preferences among different choices can be attributed to mineralogical heterogeneity and/or local matrix permeability. In other words, given two equally probable flow paths (in terms of petro-physical properties) acid would attack the path where the local background (matrix) permeability is high. In the same way, it is obvious that acid flow through more reactive path (mineralogical heterogeneity). The aim of this study is to investigate the effect of petro-physical heterogeneities, so we will leave this discussion with the above conclusions.

Figure 4.7 shows porosity variation along the BC1 sample before and after the acidization. Initial (int.) and post-acidizing (final) porosity is shown. Also shown in this figure is the total separate vug fraction variation through the core. In none of the experiments there exists any trend relating the total number of vugs to change in porosity in a specific CT slice. When acid found a separate vug there are two major possibilities: i) acid would visit other vugs (in the same plane) due to pressure drop created around them or, ii) acid would not visit other vugs on the same plane but move to next slice in main flow path. It appeared and was proven with numerical simulation that due to high pressure drop from inlet to outlet of the core, acid tends to find the vugs in the main flow direction, not in the lateral plane. In other words the pressure drop created by a separate vug is not strong enough to divert acid from its main flow path. This avoids wormhole following a tortuous path. We believe this affect contributes to early breakthrough of the acid. This analysis is in accord with the 3D images created using CT data **(Fig. 4.6).** On the contrary, if wormhole visits other separate vugs (as a function of injection velocity) in the same plan, high branching or/and tortuous path of acid should occur which would lead to high local porosity change. This would affect the pore volume to breakthrough thus the shape of the conventional breakthrough curve.

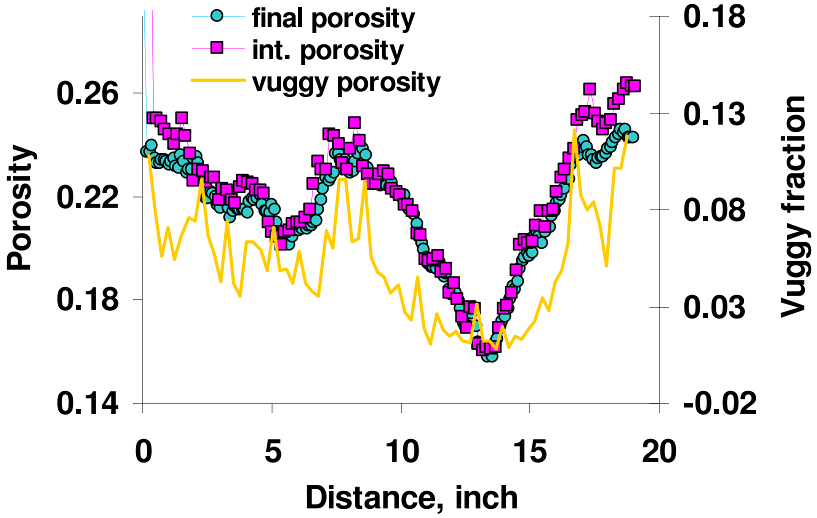

Figure 4. 7 Pre- and post-acidizing porosity and vuggy fraction

4.4 CHAPTER SUMMARY AND OBSERVATIONS

We have studied the acidizing process in vugular limestone using large (4-inch diameter by 20-inch long) samples. In this section, we observed:

1. Acid injected into vuggy limestones follows a preferential pathway guided by the vug network. This path can be predicted from the distribution of vugs in the samples as measured by CT scans on the cores before acid injected. This preferential flow path allows the acid to propagate wormholes though the rock with a very small volume of acid injected.
2. The number of pore volumes of acid solution injected to propagate a wormhole through the entire core sample in our experiments with vugular limestone (the *PVbt*) was very low, ranging from 0.04 to 0.15, an order of magnitude lower than what has been observed with relatively homogeneous limestones.
3. Although we could not clearly identify the optimal acid flux from our experiments with vuggy samples, it appears that the optimal flux is one to two orders of magnitude lower than that measured with the same acid formulation in homogeneous carbonates. This is likely because the acid is flowing through only a small portion of the rock in the vugular limestone case.
4. The *PVbt* for vuggy limestone correlates inversely with the fraction of total porosity comprised by vugs – the higher the vuggy fraction of porosity, the lower the pore volumes to breakthrough. The fraction of the porosity comprised by vugs was readily obtained from analysis of a CT scan of the samples before acid injection.

CHAPTER V

NUMERICAL MODEL

Based on fluid mass balance, resulting continuity equation, Darcy's Law, and Stokes' flow principle, a numerical model was developed. In this flow model some assumptions were made:

1. Single phase flow
2. Laminar flow
3. No inertial terms (slow viscous flow)
4. No body forces
5. No gravity effects
6. Incompressible fluid and rock

The resulting flow model is combined with a transport model. Transport models incorporate velocity dependent dispersion, and convection. Sorption and adsorption were not modeled in this model. Since the aim was to investigate the flow behavior caused by local pressure drops created by vugs, injected fluid was assumed to be a non-reactive one.

In this chapter we start with deriving the continuity equation. A combined Darcy and Stokes flow equation, known as the Darcy-Brinkman formulation (DBF), and solution method was proposed. DBF is combined with the continuity equation and solved numerically.

In the second part a conventional convection dispersion equation (CDE) was solved numerically. The finite difference approximation and solution methodology was detailed.

Use of the model to understand flow in vuggy carbonates was illustrated using several conceptual scenarios.

Outcomes of this numerical study were used to better understand the vuggy carbonate acid core flood experiments.

5.1 CONTINUITY EQUATION

In order to obtain continuity equation we will start with a control volume (CV), shown in **Fig. 5.1**. We can write a mass balance equation for this CV.

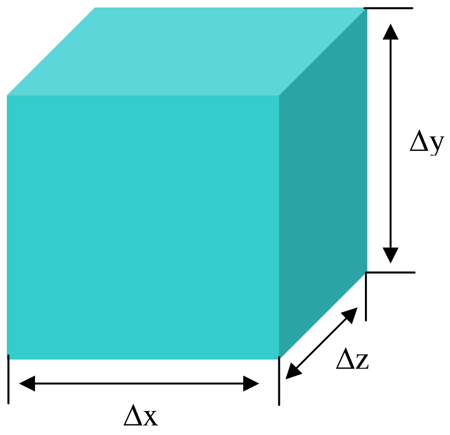

Figure 5. 1. Control volume used in the model

The mass balance equation for injected fluid is:

Fluid in - Fluid out + Source = Accumulation

It is assumed that the only source of fluid is injection.

During a certain time period Δt the mass of fluid flowing into the control volume is:

$$\Delta t\left(\rho u_x \Delta y \Delta z\big|_x + \rho u_y \Delta x \Delta z\big|_y + \rho u_z \Delta x \Delta y\big|_z\right) \tag{5.1}$$

where u_x, u_y, and u_z are the average Darcy velocities across y-z, x-z, and x-y plane respectively and ρ_{fluid} is density of the fluid.

During a certain time period Δt the mass of fluid flowing out of the control volume is

$$\Delta t\left(\rho u_x \Delta y \Delta z\big|_{x+\Delta x} + \rho u_y \Delta x \Delta z\big|_{y+\Delta y} + \rho u_z \Delta x \Delta y\big|_{z+\Delta z}\right) \tag{5.2}$$

If we assume the injected fluid is the only phase in the pore space, the mass change in the control volume during time period Δt is:

$$\Delta x \Delta y \Delta z \left((\rho\phi)^{t+\Delta t} - (\rho\phi)^{t} \right) \tag{5.3}$$

Because there is no source in the control volume, the accumulation of the injected fluid in the control volume equals to the net inflow of the fluid. Thus, the mass conservation equation for the injected fluid can be expressed as

$$\Delta x \Delta y \Delta z \left((\rho\phi)^{t+\Delta t} - (\rho\phi)^{t} \right) = \Delta t \left(\rho u_x \Delta y \Delta z \big|_x + \rho u_y \Delta x \Delta z \big|_y + \rho u_z \Delta x \Delta y \big|_z \right)$$
$$- \Delta t \left(\rho u_x \Delta y \Delta z \big|_{x+\Delta x} + \rho u_y \Delta x \Delta z \big|_{y+\Delta y} + \rho u_z \Delta x \Delta y \big|_{z+\Delta z} \right) \tag{5.4}$$

Dividing Eq. 5.4 by $\Delta x \Delta y \Delta z \Delta t$, we obtain

$$\frac{(\rho\phi)^{t+\Delta t} - (\rho\phi)^{t}}{\Delta t} = \frac{\rho u_x \big|_x - \rho u_x \big|_{x+\Delta x}}{\Delta x} + \frac{\rho u_y \big|_y - \rho u_y \big|_{y+\Delta y}}{\Delta y}$$
$$+ \frac{\rho u_z \big|_z - \rho u_z \big|_{z+\Delta z}}{\Delta z} \tag{5.5}$$

In order obtain a differential equation representing the mass conservation, the limits while Δx, Δy, and Δz approaching zero were taken with the assumption of incompressible injected fluid. This leads to

$$\frac{\partial \phi}{\partial t} = \frac{\partial u_x}{\partial x} + \frac{\partial u_y}{\partial y} + \frac{\partial u_z}{\partial z} \tag{5.6}$$

Writing this equation in vector form and assuming the porosity is not changing during the time step, Eq. 5.6 becomes

$$\nabla.\vec{u} = 0 \tag{5.7}$$

where $\vec{u}$ is the velocity vector $\{u_x, u_y, u_z\}$.

5.2 EQUATION OF MOTION: DARCY-BRINKMAN FORMULATION (DBF)

Vuggy carbonates contain two distinct regions as matrix and vuggy regions. Empirical formulation of Henry Darcy is verified, validated and approved to represent the flow in porous media. But to represent the fluid flow more adequately in the presence of high porosity, a modification to Darcy's Law is needed. In other words, in the presence of vugs and/or fractures special care should be taken employing equation of motion.

Modeling of flow in a dual-porosity porous system (fractured and/or vuggy porous) was traditionally done by using coupled Darcy-Stokes equations. While the porous media was modeled by Darcy's law, Stokes' equation was used to account for the flow in fractures and vugs (free flow). In this approach the domain studied is divided into two regions, Ω^f and Ω^p; the first one representing the free flow region and the second one corresponds to porous media. Darcy's law and Stokes' formulation can be written for these two regions as follows:

$$\nabla p - \mu_e \Delta \vec{u} = f_e \quad \text{in} \quad \Omega^f \tag{5.8}$$

$$\nabla.\vec{u} = 0 \qquad \text{in} \quad \Omega^f \tag{5.9}$$

$$\vec{u} = -\frac{k}{\mu}\left(\nabla p - f_e\right) \quad \text{in} \quad \Omega^p \tag{5.10}$$

$$\nabla.\vec{u} = 0 \qquad \text{in} \quad \Omega^p \tag{5.11}$$

Although this coupled approach seems accurate, the problems arise considering the interface conditions between two medium. The interface of two medium should be treated so that conservation of mass and momentum are honored. Several methods were proposed for this purpose, biased especially in the tangential velocity component at this interface. Each one of the previous studies proposed a different jump condition for the tangential velocities and/or stresses. Unfortunately, these jump conditions introduces additional parameters that needed to be determined. Popov et al. (2007) discussed in detail the difficulties rising with use of coupled Darcy-Stokes formulation.

An alternative approach we used in this study employs the so-called Darcy-Brinkman (1967) formulation (DBF). The power of DBF lies in its natural ability to represent both porous media and free flow in a single equation with variable coefficients. The advantage of this formulation is that there is no need to specify different boundary and interface conditions.

With inertial terms omitted Brinkman's formula takes the form:

$$\nabla p = -\frac{\mu}{k}\vec{u} + \mu_e \nabla^2 \vec{u} \tag{5.12}$$

In this equation two viscous terms appeared. The first is the usual Darcy term and the second one is analogous to the Laplacian term that appears in the Navier-Stokes equation. The second viscosity term is effective viscosity. Brinkman set μ and μ_e equal to each other, but it may not be the case in general. In this study we set μ and μ_e equal. The rationale behind our choice is that, in the porous region for moderately small permeabilities and pore volume fractions, the diffusive term ($\mu_e \nabla^2 \vec{u}$) introduces only a small perturbation of the velocity and pressure fields as compared to pure Darcy's law. So the only condition we are using is *k~infinity* in the vuggy region. Popov et al. (2007) showed the applicability of this assumption by comparing DBF under these conditions with the coupled Darcy-Stokes formulation.

It was pointed out by Tam (1969) that whenever the spatial length is much greater than $(\mu_e k/\mu)^{1/2}$, the $\nabla^2 \vec{u}$ term is negligible in comparison with the term proportional to $\vec{u}$ so that Brinkman's equation reduces to Darcy's equation.

Durlofsky and Brandy (1987), using a Green's function approach, concluded that the Brinkman equation was valid for φ (porosity) >0.95. Rubinstein (1986) concluded that the formulation could be valid for φ as small as 0.8.

DBF has a parameter *k* (the permeability) such that the equation reduces to a form of the Navier-Stokes equation as $k/L^2 \rightarrow \infty$ and to the Darcy equation as $l/L^2 \rightarrow 0$, where L is a characteristic macroscopic length scale of the problem being considered.

DBF was previously used by Golfier et al. to analyze the wormhole formation during reactive porous media flow. In their model, three regions were defined: i) a fluid zone created by complete dissolution, the initial porous media and a transient zone characterized by a porosity gradient which may eventually develop under local non-equilibrium conditions. Fluid and porous zones were modeled using either the Stokes equations or Darcy's law. This approach is only valid if interface velocity is assumed to be small, which is acceptable for most dissolution problems.

Goyeau et al show that the Stokes equations, Darcy's law and boundary conditions can be approximated, for porous media with moderate or low permeability, by a continuous formulation corresponding to DBF.

We will start with the Navier-Stokes' flow equation. Then, we will use assumptions to obtain Stokes' flow equation. Later we will embed the Darcy's law into this equation to come up with Darcy-Brinkman formulation.

The fluid is assumed incompressible and Newtonian as mentioned above. In this case, the equation of motion for a viscous, incompressible, Newtonian fluid is given by Navier-Stoke's equation:

$$\rho\left[\frac{\partial \vec{u}}{\partial t} + (\vec{u}.\nabla)\vec{u}\right] + \nabla p - \mu_e \nabla^2 \vec{u} = f_e \tag{5.13}$$

Flow in vuggy porous medium can be considered as laminar. It is also a reasonable assumption to omit inertial effects since the flow is sufficiently small. The relative importance of inertial and viscous effects is determined by dimensionless number, known as Reynold's numbr, N_{Re}, defined as:

$$N_{\mathrm{Re}} = \frac{\rho \vec{u} L}{\mu} \tag{5.14}$$

In slow viscous flows, because viscous forces arising from shearing motions of the fluid dominate over inertial forces associated with acceleration or deceleration of fluid particles, N_{Re} is small. Hence, the inertial terms, $\rho(\vec{u}.\nabla)\vec{u}$, can be omitted in the absence of any body forces for practical purposes. Thus, the equation of motion for so-called creeping flow, known as Stokes' equation is governed.

$$\frac{\partial \vec{u}}{\partial t} = -\frac{1}{\rho}\nabla p + \frac{\mu_e}{\rho}\nabla^2 \vec{u} \tag{5.15}$$

Adding the Darcian term to Stoke's formulation we have:

$$\frac{\partial \vec{u}}{\partial t} = -\frac{1}{\rho}\nabla p + \frac{\mu_e}{\rho}\nabla^2 \vec{u} - \frac{\mu}{k}\vec{u}\frac{1}{\rho} \tag{5.16}$$

5.2.1 Finite difference solution

Taking divergence of both sides of Eq. 5.16 we have:

$$\frac{\left(\nabla.\vec{u}^{\,n+1} - \nabla.\vec{u}^{\,n}\right)}{\Delta t} = -\frac{1}{\rho}\nabla^2 p^{n+1} + \frac{\mu_e}{\rho}\nabla^2\left(\nabla.\vec{u}^{\,n+1}\right) - \frac{\mu}{k}\nabla.\vec{u}^{\,n+1}\frac{1}{\rho} \tag{5.17}$$

Continuity equation, as derived above, is given by:

$$\nabla.\vec{u}^{\,n+1} = 0 \tag{5.18}$$

Plugging Eq.5.18 into the Eq.5.17 leads to Eq.5.19 which is known as Poisson's equation:

$$\nabla^2 p^{n+1} = \frac{\rho}{\Delta t}\nabla.\vec{u}^{\,n} \tag{5.19}$$

Rewriting Eq.5.19 we obtain:

$$\frac{p_{i+1,j}^{n+1} - 2p_{i,j}^{n+1} + p_{i-1,j}^{n+1}}{(\Delta x)^2} + \frac{p_{i,j+1}^{n+1} - 2p_{i,j}^{n+1} + p_{i,j-1}^{n+1}}{(\Delta y)^2}$$
$$= \frac{\rho}{\Delta t}\left(\frac{u_{x\to i+1/2,j}^{n} - u_{x\to i-1/2,j}^{n}}{\Delta x} + \frac{u_{y\to i,j+1/2}^{n} - u_{y\to i,j-1/2}^{n}}{\Delta y}\right) \tag{5.20}$$

from here:

$$-2(1+\alpha)p_{i,j}^{n+1} + \alpha p_{i,j-1}^{n+1} + \alpha p_{i,j+1}^{n+1} + p_{i-1,j}^{n+1} + p_{i+1,j}^{n+1} = \frac{\beta}{\Delta x}\left(u_{x\to i+1/2,j}^{n} - u_{x\to i-1/2,j}^{n}\right)$$
$$+\frac{\beta}{\Delta x}\left(u_{y\to i,j+1/2}^{n} - u_{y\to i,j-1/2}^{n}\right) \tag{5.21}$$

where $\alpha = \frac{(\Delta x)^2}{(\Delta y)^2}$, and $\beta = \frac{(\Delta x)^2}{\Delta t}$

The velocity field calculated from Darcy's formulation, which is a good approximation for initial conditions, is used in Eq.5.21 to estimate the initial pressure field.

Then this calculated pressure field is used in Eq.5.17 to obtain the updated velocity field. Rearranging Eq.5.17 we obtain:

$$\vec{u}^{\,n+1} - \Delta t\frac{\mu_e}{\rho}\nabla^2\vec{u}^{\,n+1} + \frac{1}{\rho}\frac{\mu}{k}\Delta t\vec{u}^{\,n+1} = \vec{u}^{\,n} - \frac{\Delta t}{\rho}\nabla p^{n+1} \tag{5.22}$$

which can be written for u, and v in finite difference form as:

$$u^{n+1}_{x\to i+1/2,j} - \Delta t\frac{\mu_e}{\rho}\left(\frac{u^{n+1}_{x\to i-1/2,j} - 2u^{n+1}_{x\to i+1/2,j} + u^{n+1}_{x\to i+3/2,j}}{(\Delta x)^2}\right) - \Delta t\frac{\mu_e}{\rho}\left(\frac{u^{n+1}_{x\to i+1/2,j-1} - 2u^{n+1}_{x\to i+1/2,j} + u^{n+1}_{x\to i+1/2,j+1}}{(\Delta y)^2}\right)$$
$$+\frac{1}{\rho}\frac{\mu}{k}\Delta t u^{n+1}_{x\to i+1/2,j} = u^{n}_{x\to i+1/2,j} - \frac{\Delta t}{\rho}\frac{\left(p^{n+1}_{i+1,j} - p^{n}_{i,j}\right)}{\Delta x} \tag{5.23}$$

$$u^{n+1}_{y\to i,j+1/2} - \Delta t\frac{\mu_e}{\rho}\left(\frac{u^{n+1}_{y\to i,j-1/2} - 2u^{n+1}_{y\to i,j+1/2} + u^{n+1}_{y\to i,j+3/2}}{(\Delta y)^2}\right) - \Delta t\frac{\mu_e}{\rho}\left(\frac{u^{n+1}_{y\to i-1,j+1/2} - 2u^{n+1}_{y\to i,j+1/2} + u^{n+1}_{y\to i+1,j+1/2}}{(\Delta y)^2}\right)$$
$$+\frac{1}{\rho}\frac{\mu}{k}\Delta t u^{n+1}_{y\to i,j+1/2} = u^{n}_{y\to i,j+1/2} - \frac{\Delta t}{\rho}\frac{\left(p^{n+1}_{i,j+1} - p^{n}_{i,j}\right)}{\Delta y} \tag{5.24}$$

This new velocity field is used in Eq.5.21 to calculate the updated pressure field.

This set of equations is solved iteratively. This procedure is repeated until the convergence criteria, $\| \vec{u}^{\,n+1} - \vec{u}^{\,n} \|_{\infty} \le \varepsilon$, is met. Here ε is the convergence criteria set by user. The Bi-conjugate gradient method was used in inner iterations.

A schematic representation of the solution algorithm is given in **Fig. 5.2**.

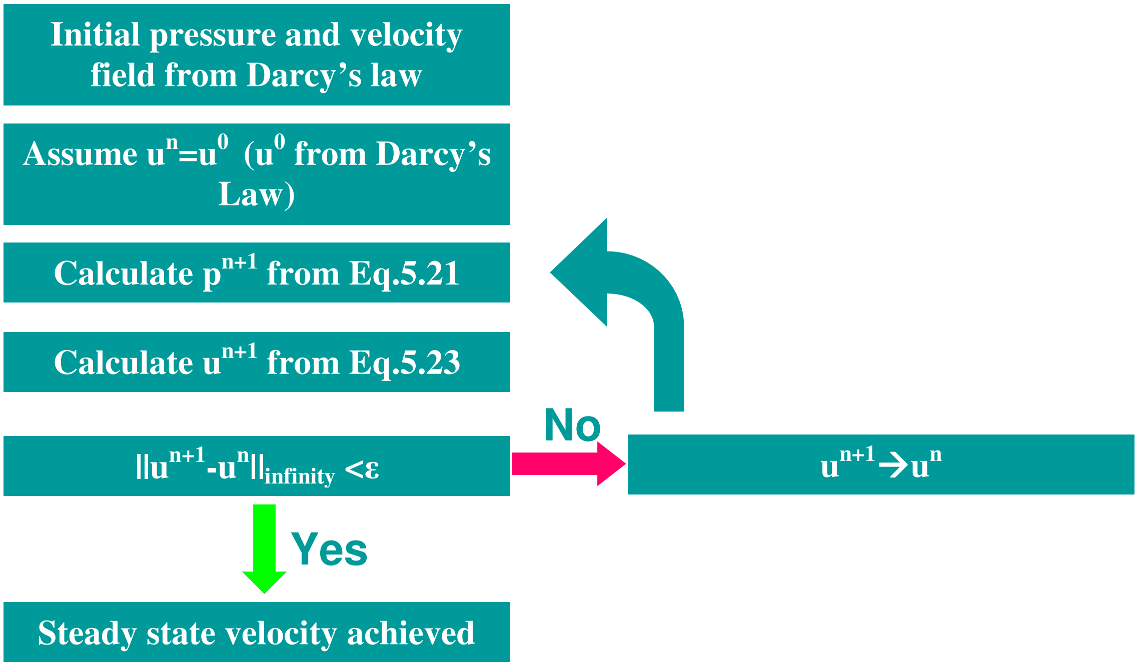

Figure 5. 2. Schematic representation of the finite difference solution algorithm for DBF

Based on the formulation shown above, a set of linear equations is solved to obtain the velocity and pressure fields at each time step. The simulation domain and boundary conditions are given in **Fig. 5.3**. For finite difference approximation we used staggered grid representation as given in **Fig. 5.4.** In this representation, pressure is defined at the center of each finite difference grid-cell, whereas the velocity components are defined on the faces of each cell in a way such that they are perpendicular to each face.

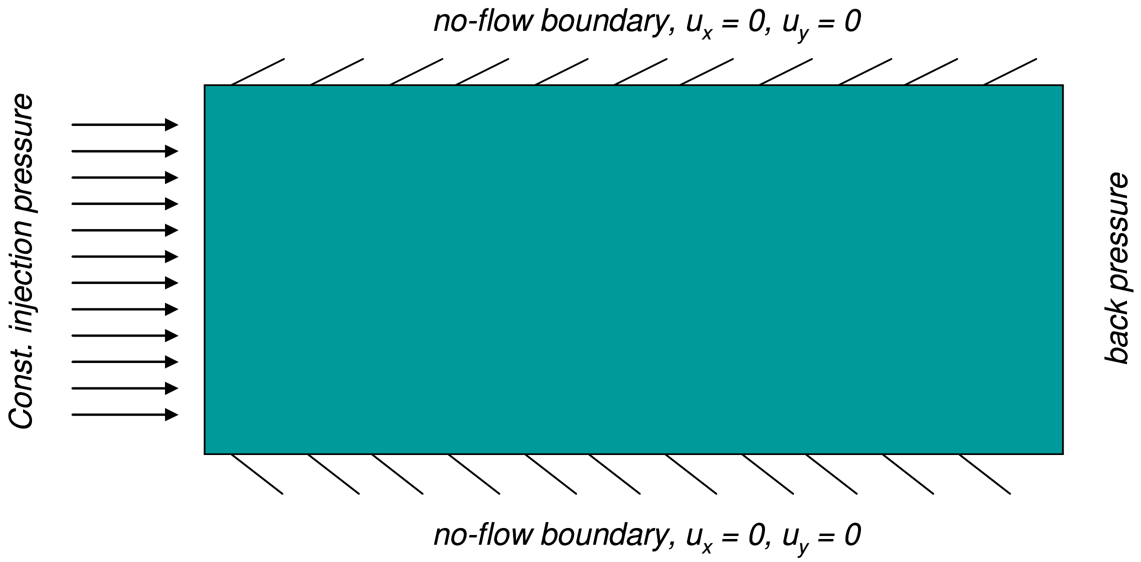

Figure 5. 3 Simulation domain and boundary conditions

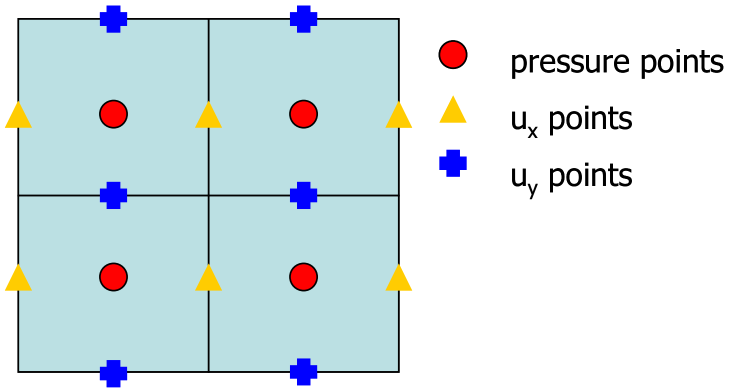

Figure 5. 4 Staggered grid used in finite difference approximation

A schematic grid configuration for the pressure field and corresponding matrix elements are given in **Fig. 5.5**.

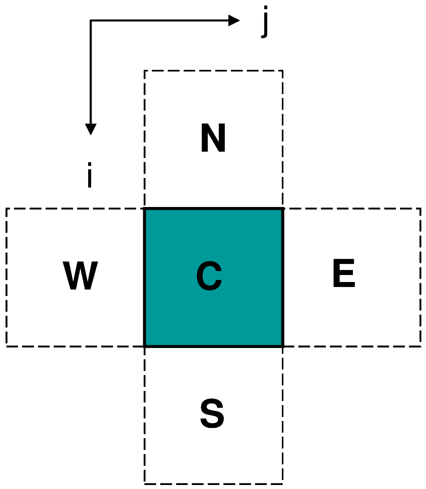

Figure 5. 5 Grid configuration and matrix elements

The coefficient matrix (A) for this problem is a sparse matrix. The general form of the matrix for Eq.5.21 is shown in **Fig. 5.6**.

$$A=\left|\begin{array}{ccccccccccccccccccccc}
C & E & . & . & S &&&&&&&&&&&&&&&& \\
W & C & E & & & S &&&&&&&&&&&&&&& \\
. & W & C & E & & & S &&&&&&&&&&&&&& \\
N & & W & . & . & & & S &&&&&&&&&&&&& \\
& N & & . & . & . & & & S &&&&&&&&&&&& \\
& & N & & . & . & . & & & S &&&&&&&&&&& \\
& & & N & & . & C & 0 & & & S &&&&&&&&&& \\
& & & & N & & 0 & C & E & & & S &&&&&&&&& \\
&&&&& N & & W & C & E & & & S &&&&&&&& \\
&&&&&& N & & W & . & E & & & S &&&&&&& \\
&&&&&&& N & & W & . & . & & & S &&&&&& \\
&&&&&&&& N & & . & . & . & & & S &&&&& \\
&&&&&&&&& N & & . & C & . & & & S &&&& \\
&&&&&&&&&& N & & . & C & 0 & & & S &&& \\
&&&&&&&&&&& N & & 0 & C & E & & & S && \\
&&&&&&&&&&&& N & & W & . & E & & & S & \\
&&&&&&&&&&&&& N & & W & . & E & & & S \\
&&&&&&&&&&&&&& N & & W & . & . & & \\
&&&&&&&&&&&&&&& N & & . & C & . & \\
&&&&&&&&&&&&&&&& N & & . & C & \\
&&&&&&&&&&&&&&&&& N & . & . & C
\end{array}\right|$$

Figure 5. 6. Representative coefficient matrix used in calculation of pressure field from Eq. 5.16

C (Center) is the diagonal of the matrix and represents the coefficient for the block of interest. From Eq.5.21 it can be written as:

$$C_{i,j} = -2(1+\alpha) \tag{5.25}$$

W (West) represents the coefficient for the block interest. From Eq.5.21 it can be written as:

$$W_{i,j} = \alpha \tag{5.26}$$

E (East) represents the coefficient for the block interest. From Eq.5.21 it can be written as:

$$E_{i,j} = \alpha \tag{5.27}$$

N (North) represents the coefficient for the block interest. From Eq.5.21 it can be written as:

$$N_{i,j} = 1 \tag{5.28}$$

S (South) represents the coefficient for the block interest. From Eq.5.21 it can be written as:

$$S_{i,j} = 1 \tag{5.29}$$

And the right hand side vector (B) can be written as:

$$B_{i,j} = \frac{\beta}{\Delta x}\left(u^n_{x\to i+1/2,j} - u^n_{x\to i-1/2,j}\right) + \frac{\beta}{\Delta y}\left(u^n_{y\to i,j+1/2} - u^n_{y\to i,j-1/2}\right) \tag{5.30}$$

The pressure field is calculated using $Ax = B$, where x is the unknown vector of pressure aimed to be calculated.

The same coefficient matrix is constructed and solved for Eqs. 5.23 and 5.24. The only difference is the elements given by C, W, E, N, and S. Dividing Eqs. 5.23 and 5.24 by

$$\gamma = -\frac{\Delta t}{\Delta x^2}\frac{\mu_e}{\rho} \tag{5.31}$$

for Eq. 5.23 we have

$$C_{i,j} = -2(1+\alpha) - \gamma + \frac{\mu}{\mu_e}\frac{\Delta x^2}{k} \tag{5.32}$$

$$W_{i,j} = \alpha \tag{5.33}$$

$$E_{i,j} = \alpha \tag{5.34}$$

$$N_{i,j} = 1 \tag{5.35}$$

$$S_{i,j} = 1 \tag{5.36}$$

$$B_{i,j} = -\gamma u_{x \to i+\frac{1}{2},j} + \frac{\Delta x}{\mu_e}\left(p^{n+1}_{i+1,j} - p^{n+1}_{i,j}\right) \tag{5.37}$$

and for Eq. 5.24 we have

$$C_{i,j} = -2(1+\alpha) - \gamma + \frac{\mu}{\mu_e}\frac{1}{k}\Delta y^2 \tag{5.38}$$

$$W_{i,j} = 1 \tag{5.39}$$

$$E_{i,j} = 1 \tag{5.40}$$

$$N_{i,j} = \alpha \tag{5.41}$$

$$S_{i,j} = \alpha \tag{5.42}$$

$$B_{i,j} = -\gamma u_{x \to i+\frac{1}{2},j} + \frac{\Delta y}{\mu_e}\left(p_{i+1,j}^{n+1} - p_{i,j}^{n+1}\right) \tag{5.43}$$

The velocity field is calculated using $Ax = B$, where x is the unknown vector of the velocity field to be calculated.

Since the simulation domain is a confined domain, at the boundary of this domain boundary conditions, as given in **Fig. 5.3**, are applied as follows.

Constant pressure at inlet

if i=1 then;

For Eq.5.21:

$$N_{i,j} = 0 \tag{5.44}$$

$$B_{i,j} = \frac{\beta}{\Delta x}\left(u_{x \to i+1/2,j}^{n} - u_{x \to i-1/2,j}^{n}\right) + \frac{\beta}{\Delta y}\left(u_{y \to i,j+1/2}^{n} - u_{y \to i,j-1/2}^{n}\right) - p_{inlet} \tag{5.45}$$

For Eq.5.23:

$$N_{i,j} = 0 \tag{5.46}$$

$$C_{i,j} = -2(1+\alpha) - \gamma + \frac{\mu}{\mu_e}\frac{\Delta x^2}{k} + 1 \tag{5.47}$$

For Eq.5.24:

$$N_{i,j} = 0 \tag{5.48}$$

The other elements remain constant.

Constant pressure at outlet

if i=nx then;

For Eq.5.21:

$$S_{i,j} = 0 \tag{5.49}$$

$$B_{i,j} = \frac{\beta}{\Delta x}\left(u^n_{x\to i+1/2,j} - u^n_{x\to i-1/2,j}\right) + \frac{\beta}{\Delta y}\left(u^n_{y\to i,j+1/2} - u^n_{y\to i,j-1/2}\right) - p_{outlet} \tag{5.50}$$

For Eq.5.23:

$$S_{i,j} = 0 \tag{5.51}$$

$$C_{i,j} = -2(1+\alpha) - \gamma + \frac{\mu}{\mu_e}\frac{\Delta x^2}{k} + 1 \tag{5.52}$$

For Eq.5.24:

$$N_{i,j} = 0 \tag{5.53}$$

The other elements remain constant.

No-flow at the side boundaries

If j=1 then;

For Eq. 5.21:

$$W_{i,j} = 0 \tag{5.54}$$

$$C_{i,j} = -2(1+\alpha) + \alpha \tag{5.55}$$

For Eq. 5.23:

Velocity boundary conditions at no-flow boundaries can be put that for no-slip wall, normal velocity remains the same while tangential velocity reverses. Thus:

$$W_{i,j} = 0 \tag{5.56}$$

$$C_{i,j} = -2(1+\alpha) + \alpha \tag{5.57}$$

For Eq. 5.24:

$$W_{i,j} = 0$$

if j=ny then;

For Eq. 5.21:

$$E_{i,j} = 0 \tag{5.58}$$

$$C_{i,j} = -2(1+\alpha)+\alpha \tag{5.59}$$

For Eq. 5.23:

$$E_{i,j} = 0 \tag{5.60}$$

$$C_{i,j} = -2(1+\alpha)+\alpha \tag{5.61}$$

For Eq. 5.24:

$$C_{i,j} = 1$$

$$W_{i,j} = 0 \tag{5.62}$$

$$E_{i,j} = 0 \tag{5.63}$$

$$N_{i,j} = 0 \tag{5.64}$$

$$S_{i,j} = 0 \tag{5.65}$$

$$B_{i,j} = 0 \tag{5.66}$$

We solved these equations in a 2D domain. The same physics and mathematical model are also applied to the 3D domain, where we discussed the benefits of using streamlines for velocity field visualization.

5.3 CONVECTION DISPERSION EQUATION (CDE)

5.3.1 Diffusion, dispersion, and convection

The spreading of a dissolved mass as it moves with a flowing fluid has been traditionally ascribed to two mechanisms:

1. Convection
2. Dispersion

Molecules in the liquid or vapor states are in continuous random motion even if the bulk fluid velocity is zero. This random motion results in net movement of solute particles from regions of high solute concentration to regions having low concentration. This process is a process by which the concentration gradient diminishes by time, and is called diffusion. The diffusive flux is decribed by Fick's law:

$$J = -D_m \frac{dC}{dx} \tag{5.67}$$

where D_m is diffusion coefficient and the derivative is concentration gradient.

From mass conservation we know that:

$$\frac{\partial C}{\partial t} = -\frac{\partial J}{\partial x} \tag{5.68}$$

Differentiating Fick's equation with respect to distance and using the mass balance equation we obtained:

$$\frac{\partial C}{\partial t} = D_m \frac{\partial^2 C}{\partial x^2} \tag{5.69}$$

This equation shows how the solute concentration varies with time and space because of the diffusion.

When the fluid moves through a porous media, there is additional mixing because of the convection. The complex pore structure results in flowing fluid to take a tortuous path. Variations in local velocity in magnitude and direction along tortuous flow paths cause solute particles to spread. This is called convective spreading or mechanical dispersion. By its nature mechanical dispersion is considered to be Fickian (diffusion-like).

Hydrodynamic dispersion is commonly characterized by an empirical relationship (Perkins and Johnston 1963, Fried and Combarnous 1971), in which the dispersion mechanism is described by contributions of molecular diffusion and mechanical dispersion expressed as a function of the Péclet number. Comprehensive summary of over 40 models based on the analytical solution of the 1D advective-dispersive transport equation is given by Genuchten and Alve (1982). Kwok et al. (1994) also gave a great summary on the subject.

The dispersion coefficient, which considers the effects of both molecular diffusion and mechanical dispersion, is usually represented by an empirical function of the Péclet number, $Pe = ud / D_m$ (Perkins and Johnston 1967, Fried and Combarnous 1971, Kwok et al. 1994):

$$\frac{D}{D_m} = \frac{1}{F\phi} + aPe^m \tag{5.70}$$

where F formation resistivity factor, a is a proportionality constant, m is a constant, D_m is the molecular diffusion coefficient within the porous media, u is the characteristic velocity, D is the dispersion coefficient, and d is the characteristic length. Fried and Combarnous (1971) presented five flow regimes defined by the magnitude of Péclet number. These are:

i) Pure molecular diffusion, $Pe \leq 0.6$

ii) Superimposition, $0.6 \leq Pe \leq 6.5$

iii) Predominantly mechanical dispersion, $6.5 \le Pe \le 300$

iv) Pure mechanical dispersion, $300 \le Pe \le 2.1x10^5$

v) Pure mechanical dispersion with turbulence effects (Darcy's Law is no longer applicable), $Pe \ge 2.1x10^5$

Dispersion coefficient can be represented with two terms that quantify both diffusion and hydrodynamic advection as:

$$D_L = D_m + \alpha_L u_x \tag{5.71}$$

$$D_T = D_m + \alpha_T u_y \tag{5.72}$$

where D_L , D_T are the coefficients of longitudinal and transverse dispersion, respectively; α_L and α_T are the longitudinal and transverse hydrodynamic dispersivities, respectively.

If the effect of molecular diffusion is negligible compared to the mechanism of dispersion, the dispersion coefficient can be simplified to a linear relationship, $D = \alpha u$. The dispersivity, α , can be evaluated directly from the time-distribution curve of solute concentration (Hoopes and Harleman 1967). It is well accepted in literature that convective spreading (mechanical dispersion) is orders of magnitude larger than diffusion.

It is important to mention that dispersion coefficient is a lumped parameter; thus, it does not give any information about relative importance of diffusion and dispersion.

With this introduction, we will start with deriving conventional convection-dispersion equation, and state our assumptions. Then the finite difference approximation, boundary conditions and solution approach will be presented.

5.3.2 Derivation of CDE

Using same CV given in **Fig. 5.1**:

The fundamental mass balance equation (for a tracer) is given by:

$$\sum I + \sum P - \sum O - \sum L = \sum A \tag{5.73}$$

where I, O, A correspond to the mass input, output and accumulation respectively, and P, L represents production and losses.

In our problem since we don’t have any production injection or chemical reactions in the control volume this relation reduces to:

$$\sum I - \sum O = \sum A \tag{5.74}$$

Starting with a control volume (CV) during a time period Δt, the total amount of tracer entering into the control volume is:

$$\Delta t(\overline{C}_{x,y,z} u_x \phi_{x,y,z,} \Delta y \Delta z + \overline{C}_{x,y,z} u_y \phi_{x,y,z,} \Delta x \Delta z + \overline{C}_{x,y,z} u_z \phi_{x,y,z,} \Delta x \Delta y$$
$$- D \left.\frac{\partial \overline{C}}{\partial x}\right|_x - D \left.\frac{\partial \overline{C}}{\partial y}\right|_y - D \left.\frac{\partial \overline{C}}{\partial z}\right|_z) \tag{5.75}$$

Similarly the amount of the tracer leaving control volume is:

$$\Delta t(\overline{C}_{x+\Delta x,y,z} u_{x+\Delta x} \phi_{x+\Delta x,y,z} \Delta y \Delta z + \overline{C}_{x,y+\Delta y,z} u_{y+\Delta y} \phi_{x,y+\Delta y,z,} \Delta x \Delta z + \overline{C}_{x,y,z+\Delta z} u_{z+\Delta z} \phi_{x,y,z+\Delta z} \Delta x \Delta y$$
$$- D \left.\frac{\partial \overline{C}}{\partial x}\right|_{x+\Delta x} - D \left.\frac{\partial \overline{C}}{\partial y}\right|_{y+\Delta y} - D \left.\frac{\partial \overline{C}}{\partial z}\right|_{z+\Delta z}) \tag{5.76}$$

The change in the amount of tracer in the control volume during Δt is:

$$\Delta x \Delta y \Delta z \left\{ \left(\overline{C}\phi_{x,y,z}\right)^{n+1} - \left(\overline{C}\phi_{x,y,z}\right)^{n} \right\} \tag{5.77}$$

The mass balance for tracer requires that the change of tracer is equal to difference between mass of tracer entering and leaving the control volume. Thus we obtain:

$$
\begin{aligned}
&\Delta t(\overline{C}_{x,y,z}u_x\phi_{x,y,z,}\Delta y\Delta z+\overline{C}_{x,y,z}u_y\phi_{x,y,z,}\Delta x\Delta z+\overline{C}_{x,y,z}u_z\phi_{x,y,z,}\Delta x\Delta y_x-D\left.\frac{\partial\overline{C}}{\partial x}\right|_x\\
&-D\left.\frac{\partial\overline{C}}{\partial y}\right|_y-D\left.\frac{\partial\overline{C}}{\partial z}\right|_z)-\Delta t(\overline{C}_{x+\Delta x,y,z}u_{x+\Delta x}\phi_{x+\Delta x,y,z}\Delta y\Delta z+\overline{C}_{x,y+\Delta y,z}u_{y+\Delta y}\phi_{x,y+\Delta y,z,}\Delta x\Delta z\\
&+\overline{C}_{x,y,z+\Delta z}u_{z+\Delta z}\phi_{x,y,z+\Delta z}\Delta x\Delta y-D\left.\frac{\partial\overline{C}}{\partial x}\right|_{x+\Delta x}-D\left.\frac{\partial\overline{C}}{\partial y}\right|_{y+\Delta y}-D\left.\frac{\partial\overline{C}}{\partial z}\right|_{z+\Delta z})\\
&=\Delta x\Delta y\Delta z\left\{\left(\overline{C}\phi_{x,y,z}\right)^{n+1}-\left(\overline{C}\phi_{x,y,z}\right)^{n}\right\}
\end{aligned}
\tag{5.78}
$$

Dividing this expression by Δ*x*.Δ*y*.Δ*z*.Δ*t* and taking the limits as $\Delta x \rightarrow 0$, $\Delta y \rightarrow 0$, $\Delta z \rightarrow 0$, and $\Delta t \rightarrow 0$ we obtain:

$$
\begin{aligned}
&\phi\frac{\partial\overline{C}}{\partial t}+\frac{\partial\left(\overline{C}u_x\right)}{\partial x}+\frac{\partial\left(\overline{C}u_y\right)}{\partial y}+\frac{\partial\left(\overline{C}u_z\right)}{\partial z}-D_x\frac{\partial}{\partial x}\left(\frac{\partial\overline{C}}{\partial x}\right)-D_y\frac{\partial}{\partial y}\left(\frac{\partial\overline{C}}{\partial y}\right)\\
&-D_z\frac{\partial}{\partial z}\left(\frac{\partial\overline{C}}{\partial z}\right)=0
\end{aligned}
\tag{5.79}
$$

Adding the velocity dependent dispersion coefficient we obtain

$$
\begin{aligned}
&\phi\frac{\partial\overline{C}}{\partial t}+\frac{\partial\left(\overline{C}u_x\right)}{\partial x}+\frac{\partial\left(\overline{C}u_y\right)}{\partial y}+\frac{\partial\left(\overline{C}u_z\right)}{\partial z}-\alpha_x\frac{\partial}{\partial x}\left(u_x\frac{\partial\overline{C}}{\partial x}\right)-\alpha_y\frac{\partial}{\partial y}\left(u_y\frac{\partial\overline{C}}{\partial y}\right)\\
&-\alpha_z\frac{\partial}{\partial z}\left(u_z\frac{\partial\overline{C}}{\partial z}\right)=0
\end{aligned}
\tag{5.80}
$$

Li (2004) used a similar equation without the dispersion terms to account for the transport of acid in sandstones. Considering the relatively homogenous pore structures of sandstones this may be a reasonable assumption. Under relatively homogenous flow field, diffusion will have little impact on hydrodynamic dispersion or heterogeneous advection because each streamline is relatively similar to the neighboring streamline. In fractured and/or vuggy rocks, however, velocity fields can be so heterogeneous that neighboring streamlines may have vastly different velocities.

Chaudhari (1971) incorporate this effect and with a constant velocity field assumption gave a 1D analytical solution for Eq.5.80.

Here will use finite difference approximation to solve Eq.5.80 in 2D, and 3D simulation domains.

5.3.3 Finite difference approximation

$$
\begin{aligned}
&\phi \frac{\overline{C}^{n+1}_{i,j,k} - \overline{C}^{n}_{i,j,k}}{\Delta t} + \frac{u^{n+1}_{x\to i+1/2,j,k}.\overline{C}^{n+1}_{i+1/2,j,k} - u^{n+1}_{x\to i-1/2,j,k}.\overline{C}^{n+1}_{i-1/2,j,k}}{\Delta x} \\
&+ \frac{u^{n+1}_{y\to i,j+1/2,k}.\overline{C}^{n+1}_{i,j+1/2,k} - u^{n+1}_{y\to i,j-1/2,k}.\overline{C}^{n+1}_{i,j-1/2,k}}{\Delta y} + \frac{u^{n+1}_{z\to i,j,k+1/2}.\overline{C}^{n+1}_{i,j,k+1/2} - u^{n+1}_{z\to i,j,k-1/2}.\overline{C}^{n+1}_{i,j,k-1/2}}{\Delta z} \\
&- \alpha_x \frac{1}{\Delta x}\left(u^{n+1}_{x\to i+1/2,j,k} \frac{\overline{C}^{n+1}_{i+1,j,k} - \overline{C}^{n+1}_{i,j,k}}{\Delta x} - u^{n+1}_{x\to i-1/2,j,k} \frac{\overline{C}^{n+1}_{i,j,k} - \overline{C}^{n+1}_{i-1,j,k}}{\Delta x} \right) \\
&- \alpha_y \frac{1}{\Delta y}\left(u^{n+1}_{y\to i,j+1/2,k} \frac{\overline{C}^{n+1}_{i,j+1,k} - \overline{C}^{n+1}_{i,j,k}}{\Delta y} - u^{n+1}_{y\to i,j-1/2,k} \frac{\overline{C}^{n+1}_{i,j,k} - \overline{C}^{n+1}_{i,j-1,k}}{\Delta y} \right) \\
&- \alpha_z \frac{1}{\Delta z}\left(u^{n+1}_{z\to i,j,k+1/2} \frac{\overline{C}^{n+1}_{i,j,k+1} - \overline{C}^{n+1}_{i,j,k}}{\Delta z} - u^{n+1}_{z\to i,j,k-1/2} \frac{\overline{C}^{n+1}_{i,j,k} - \overline{C}^{n+1}_{i,j,k-1}}{\Delta z} \right) = 0
\end{aligned}
\tag{5.81}
$$

here $\overline{C}_{i+1/2,j,k} = \dfrac{\overline{C}_{i+1,j,k} + \overline{C}_{i,j,k}}{2}$, $\overline{C}_{i,j+1/2,k} = \dfrac{\overline{C}_{i,j+1,k} + \overline{C}_{i,j,k}}{2}$, and

$$\overline{C}_{i,j,k+1/2} = \frac{\overline{C}_{i,j,k+1} + \overline{C}_{i,j,k}}{2}$$

So Eq.5.81 becomes

$$\begin{aligned}
&\phi\left(\overline{C}^{n+1}_{i,j,k} - \overline{C}^{n}_{i,j,k}\right) + \frac{\Delta t}{2\Delta x}\left[\left(\overline{C}^{n+1}_{i+1,j,k} + \overline{C}^{n+1}_{i,j,k}\right).u^{n+1}_{x\to i+1/2,j,k} - \left(\overline{C}^{n+1}_{i,j,k} + \overline{C}^{n+1}_{i-1,j,k}\right).u^{n+1}_{x\to i-1/2,j,k}\right] \\
&+ \frac{\Delta t}{2\Delta y}\left[\left(\overline{C}^{n+1}_{i,j+1,k} + \overline{C}^{n+1}_{i,j,k}\right).u^{n+1}_{y\to i,j+1/2,k} - \left(\overline{C}^{n+1}_{i,j,k} + \overline{C}^{n+1}_{i,j-1,k}\right).u^{n+1}_{y\to i,j-1/2,k}\right] \\
&+ \frac{\Delta t}{2\Delta z}\left[\left(\overline{C}^{n+1}_{i,j,k+1} + \overline{C}^{n+1}_{i,j,k}\right).u^{n+1}_{z\leftarrow i,j,k+1/2} - \left(\overline{C}^{n+1}_{i,j,k} + \overline{C}^{n+1}_{i,j,k-1}\right).u^{n+1}_{z\to i,j,k-1/2}\right] \\
&- \frac{\alpha_x \Delta t}{\Delta x^2}\left[\left(\overline{C}^{n+1}_{i+1,j,k} - \overline{C}^{n+1}_{i,j,k}\right).u^{n+1}_{x\to i+1/2,j,k} - \left(\overline{C}^{n+1}_{i,j,k} - \overline{C}^{n+1}_{i-1,j,k}\right).u^{n+1}_{x\to i-1/2,j,k}\right] \\
&- \frac{\alpha_y \Delta t}{\Delta y^2}\left[\left(\overline{C}^{n+1}_{i,j+1,k} - \overline{C}^{n+1}_{i,j,k}\right).u^{n+1}_{y\to i,j+1/2,k} - \left(\overline{C}^{n+1}_{i,j,k} - \overline{C}^{n+1}_{i,j-1,k}\right).u^{n+1}_{y\to i,j-1/2,k}\right] \\
&- \frac{\alpha_z \Delta t}{\Delta z^2}\left[\left(\overline{C}^{n+1}_{i,j,k+1} - \overline{C}^{n+1}_{i,j,k}\right).u^{n+1}_{z\to i,j,k+1/2} - \left(\overline{C}^{n+1}_{i,j,k} - \overline{C}^{n+1}_{i,j,k-1}\right).u^{n+1}_{z\to i,j,k-1/2}\right] = 0
\end{aligned} \tag{5.82}$$

For practical purposes we solved this set of equations in 2D simulation domain. In this case, the elements of the matrix can be written as follows:

$$\begin{aligned}
C_{i,j} &= \phi + \frac{\Delta t}{2\Delta x}\left(u^{n+1}_{x\to i+1/2,j} - u^{n+1}_{x\to i-1/2,j}\right) + \frac{\Delta t}{2\Delta y}\left(u^{n+1}_{y\to i,j+1/2} - u^{n+1}_{y\to i,j-1/2}\right) \\
&+ \frac{\alpha_x \Delta t}{\Delta x^2}\left(u^{n+1}_{x\to i+1/2,j} + u^{n+1}_{x\to i-1/2,j}\right) + \frac{\alpha_y \Delta t}{\Delta y^2}\left(u^{n+1}_{y\to i,j+1/2} + u^{n+1}_{y\to i,j-1/2}\right)
\end{aligned} \tag{5.83}$$

$$W_{i,j} = u^{n+1}_{y\to i,j-1/2}\left(-\frac{\Delta t}{2\Delta y} - \frac{\alpha_y \Delta t}{\Delta y^2}\right) \tag{5.84}$$

$$E_{i,j} = u^{n+1}_{y\to i,j+1/2}\left(\frac{\Delta t}{2\Delta y} - \frac{\alpha_y \Delta t}{\Delta y^2}\right) \tag{5.85}$$

$$N_{i,j} = u^{n+1}_{x\to i-1/2}\left(-\frac{\Delta t}{2\Delta x} - \frac{\alpha_x \Delta t}{\Delta x^2}\right) \tag{5.86}$$

$$S_{i,j} = u^{n+1}_{x\to i+1/2,j}\left(\frac{\Delta t}{2\Delta x} - \frac{\alpha_x \Delta t}{\Delta x^2}\right) \tag{5.87}$$

$$B_{i,j} = \phi^n_{i,j}\overline{C}^n_{i,j} \tag{5.88}$$

The concentration field is calculated using $Ax=B$, where x is the unknown vector of pressure aimed to be calculated.

Since the simulation domain is a confined domain, at the boundary of this domain boundary conditions, as given in **Fig. 5.3**, are applied as follows.

Constant injection concentration at inlet

if i=1 then;

$$C_{i,j} = \phi + \frac{\Delta t}{2\Delta x}\left(u^{n+1}_{x\to i+1/2,j} - u^{n+1}_{x\to i+1/2,j}\right) + \frac{\Delta t}{2\Delta y}\left(u^{n+1}_{y\to i,j+1/2} - u^{n+1}_{y\to i,j-1/2}\right)$$
$$+ \frac{\alpha_x \Delta t}{\Delta x^2}\left(u^{n+1}_{x\to i+1/2,j} + u^{n+1}_{x\to i+1/2,j}\right) + \frac{\alpha_y \Delta t}{\Delta y^2}\left(u^{n+1}_{y\to i,j+1/2} + u^{n+1}_{y\to i,j-1/2}\right) \tag{5.89}$$

$$N_{i,j} = 0 \tag{5.90}$$

No-flow at the side boundaries

All of the elements are the same.

Based on the above partial differential equations, finite difference approximations and boundary conditions a computer program was developed. Use of the program to understand the flow in vuggy carbonates is illustrated in the following sections.

5.4 BENCHMARKING

In order to test the accuracy of the DBF, the two extremes were tested: i) complete free flow and ii) porous media flow.

The analytical solution for complete free flow region is given as (Fox and McDonald, 1998):

$$u_x = -\frac{1}{2\mu}\frac{dp}{dx}\left[\frac{h^2}{4} - (y - \frac{h}{2})^2\right] \qquad (5.91)$$

The result of the free flow simulation (equation converging to Stokes' formulation) is perfectly matched to the analytical solution (**Fig. 5.7**). The porous media simulation (equation converging to Darcy's Law) gave the homogenous up-scaled permeability with 99.99 % accuracy. Simulation parameters were summarized in **Table 5.1**.

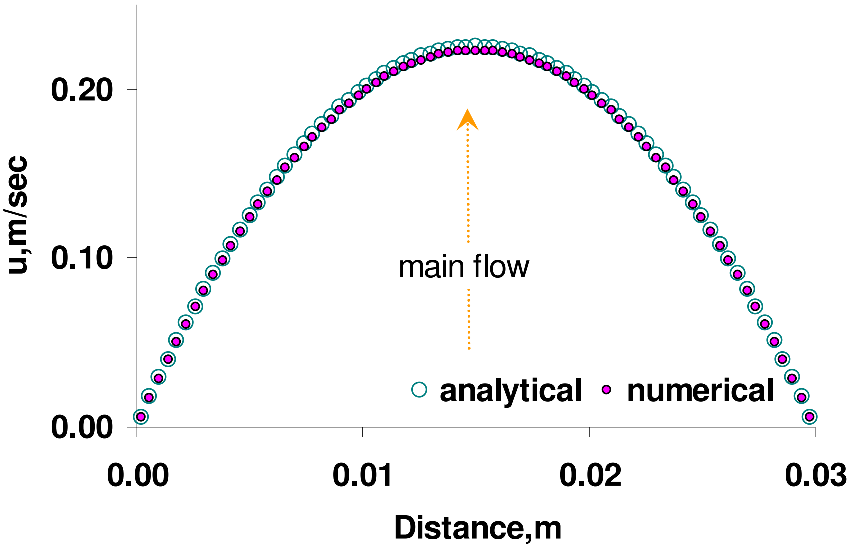

Figure 5. 7 Comparison of analytical solution and numerical simulation of flow between two parallel plates with DB formulation (ana: analytical, num: numerical)

Table 5.1 Simulation parameters used in benchmarking

Pressure gradient, Pa/m	2
μ, Pa-sec	0.001
h, m	0.03
L, m	0.5
ρ, kg/m3	1000
Simulation grid	240x120

5.5 EFFECT OF CONNECTIVITY OF VUGS ON FLOW BEHAVIOR

First we studied the effect of connectivity of vugs on effective (domain or up-scaled) permeability. As discussed previously, vugs can be classified as separate and touching vugs. The aim of this study is to understand the importance of the connectivity between vugs. A setting given in **Fig. 5.8** was used. In this figure, vuggy cells are represented with red, matrix cells with purple. Light blue region shows the connection cells.

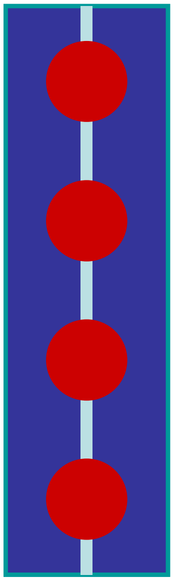

Figure 5. 8 Models used in connectivity investigation

Numerical experiments were conducted with the following manner:

1. Assign permeability to connection cells.

2. Calculate effective permeability of the domain (with the known pressure drop and calculated flux).
3. Increase the permeability of the connection and run the model again. Calculate the effective permeability.
4. Repeat these steps multiple times.

Since $\vec{u}$ is a linear function of ∇p, these two quantities are related by the macroscopic permerability tensor *k* with Darcy's law.

The results of 10 simulation runs are summarized in **Fig. 5.9**. In this figure 3 distinct regions can be identified. The early plateau in this figure corresponds to low connectivity between vugs. In this case all the vugs are separate. Any change in connection cells is hardly reflected to effective permeability of the whole domain. The increasing trend in the middle region corresponds to moderate connectivity between vugs. It can be speculated that in this region vugs are connected with narrow throat or the connections are partially plugged. The second plateu at the right most-end covers the free (tube) flow region. In this part there is good connection between vugs. The connection cells turn red, which means there is a connected vug network from inlet to the outlet of the core. Also, vugs connected with fractures fall into this region. In this case, the middle region can be interpreted as filled, collapsed or plugged fractures. Mathematically, the model converges to Stokes' equation in the second plateau. Steady state velocity fields for these three cases are given in **Fig. 5.10**.

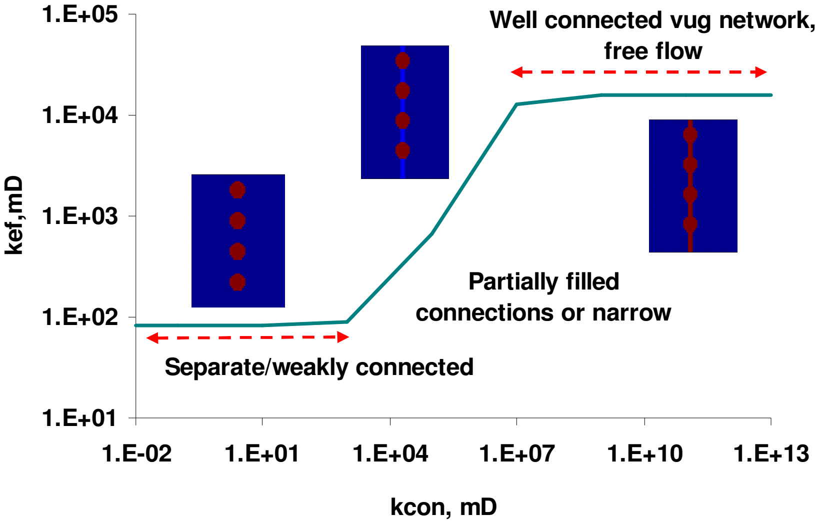

Figure 5. 9 Connectivity investigation: change in effective permeability of the domain (keff) as a function of connectivity permeability (kcon)

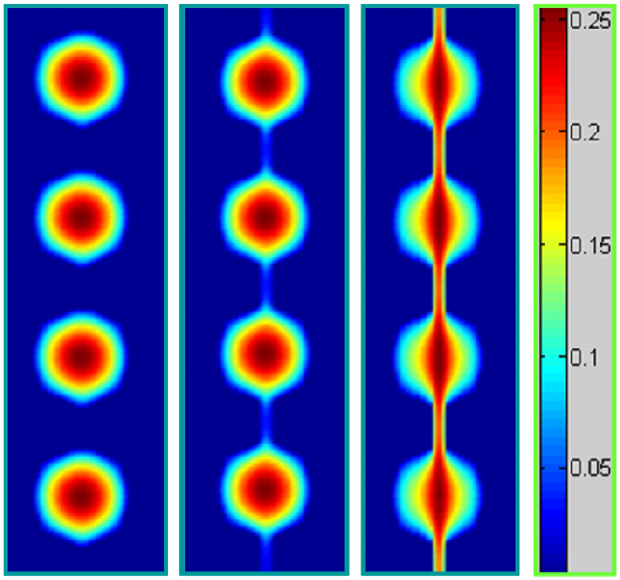

Figure 5. 10 Velocity fields, from left to right increasing connection permeability

There are multiple lessons learned from this numerical investigation:

1. Connectivity between the vugs has a significant effect on velocity field, thus pore volume to breakthrough.

2. Connectivity between the vugs has a significant effect on up-scaled or effective domain permeability.
3. By its nature DBF proposes a transition between flow in matrix and free-flow medium, which covers all the cases that can occur in the presence of vugs (separate, connected, partially-filled, damaged).
4. Removal of damage in a vug network and/or filled fracture would lead to tremendous increase in the permeability (transition from middle region to secondary plateau in the plot). Removal of this kind of damage would lead to a tremendous increase in near-wellbore permeability and rapid decrease in skin.

5.6 SEPARATE VUG SCENARIOS

Previously, we have studied the acidization of vuggy carbonates with acid core flood experiments in 4-inch diameter by 20-inch long cores, high resolution computerized tomography imaging, image processing and geostatistical characterization. The obvious major finding from these tests is that acid propagates wormholes through vuggy carbonates much more rapidly than occurs in more homogeneous rocks. Acid-created wormholes were observed to breakthrough to the end of the cores an order of magnitude more rapidly than occurs in more homogeneous cores, highlighting the necessity of understanding the flow and transport in vuggy carbonates. The fact that acid channeled through the vugular cores, following the path of the vug system, was underlined with computerized tomography scans of the cores before and after acid injection. This observation proposes that local pressure drops created by vugs are more dominant in determining the wormhole flow path than the chemical reactions occurring at the pore level.

It is clear from CT scans (**Appendix C**) and geostatistical characterization that the total amount, size and correlation strength of vugs vary in each sample. We studied the effects of these parameters with the model developed. Several scenarios were created to better understand the effect of the amount of vuggy pore space, their spatial distribution, and size.

First we ran a simple case to understand the effect of a single vug on pressure drop behavior and velocity field around it. **Fig. 5.11** illustrates this point. In this simulation, no flow boundaries are assigned to the top and bottom of the domain. A constant pressure drop was assigned between the inlet and outlet of the domain. The steady state pressure and velocity fields are presented. A screen shot of tracer propagation in an arbitrary time is taken during the simulation to illustrate the non-reactive tracer flow. **Table 5.2** summarizes the simulation parameters.

Table 5.2 Simulation parameters used in single vug simulation

Pressure gradient, Pa/m	160000
μ, Pa-sec	0.001
h, m	0.05
L, m	0.05
ρ, kg/m3	1000
k, mD	220
Simulation grid	240x240

The result of the simulation demonstrates that a single vug acts as a high permeability streak in the region. This leads to channeling of injected fluid through the vug which contributes to early breakthrough of the fluid. Simulation of a domain without the vug gave a fluid velocity of 0.05 cm/sec which is 5 times smaller than that observed at the center of the vug.

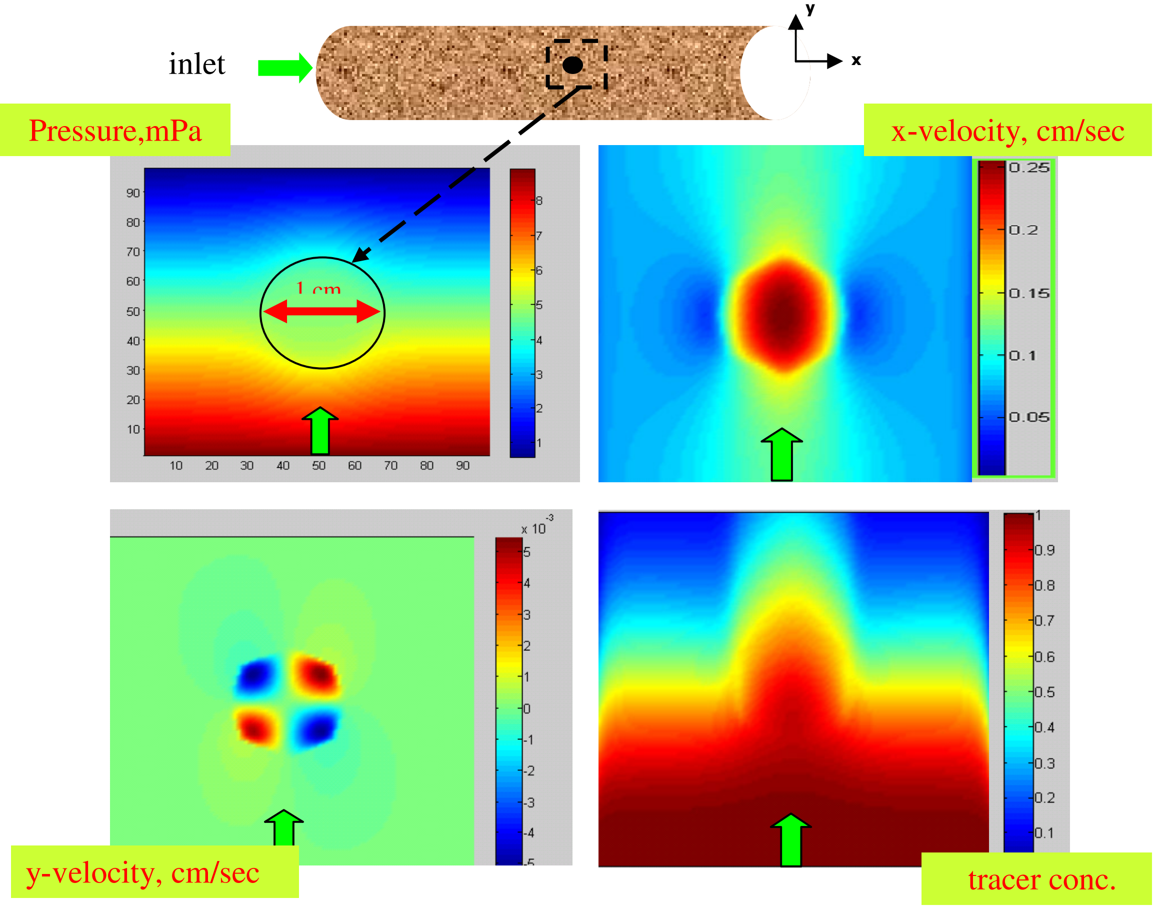

Figure 5. 11 Form left top to right bottom: pressure drop, velocity field in main flow direction, velocity field in secondary flow direction and tracer path (respectively) observed near a 1 cm radius separate vug

5.6.1 Effect of vuggy pore space fraction on PVbt

In section 5.5 we studied the effect of the connection between the vugs on the velocity field. The most important lesson learned from this study is that depending on the connection between vugs, vuggy formations may exhibit very distinct flow behaviors. Existence of separate vugs and touching vug networks makes the difference. Putting that, another question arises: What is the contribution of separate vugs to flow behavior, thus *PVbt*?

Fig. 4.5 clearly illustrates that the total pore volume of acid needed to propagate a wormhole through cores are directly proportional to the amount of space occupied by vugs (in our experiments separate vugs). It is also evident from pressure drop curves observed in experiments. Putting the assumption that "*local pressure drops created by vugs are more dominant in determining the wormhole flow path than the chemical reactions occurring at the pore level*" we investigated this point further with the numerical model developed.

8 different domains were simulated (**Fig. 5.12**). Starting from the highest number, we decreased the number of vugs in these scenarios. Simulations were stopped when the dimensionless effluent concentration (inlet concentration/outlet concentration) reaches to 0.5, which is defined as breakthrough in this study. **Fig. 5.13** summarizes the results of these numerical experiments. The results are in accord with the experimentally observed relationship between total vuggy pore space and *PVbt.*

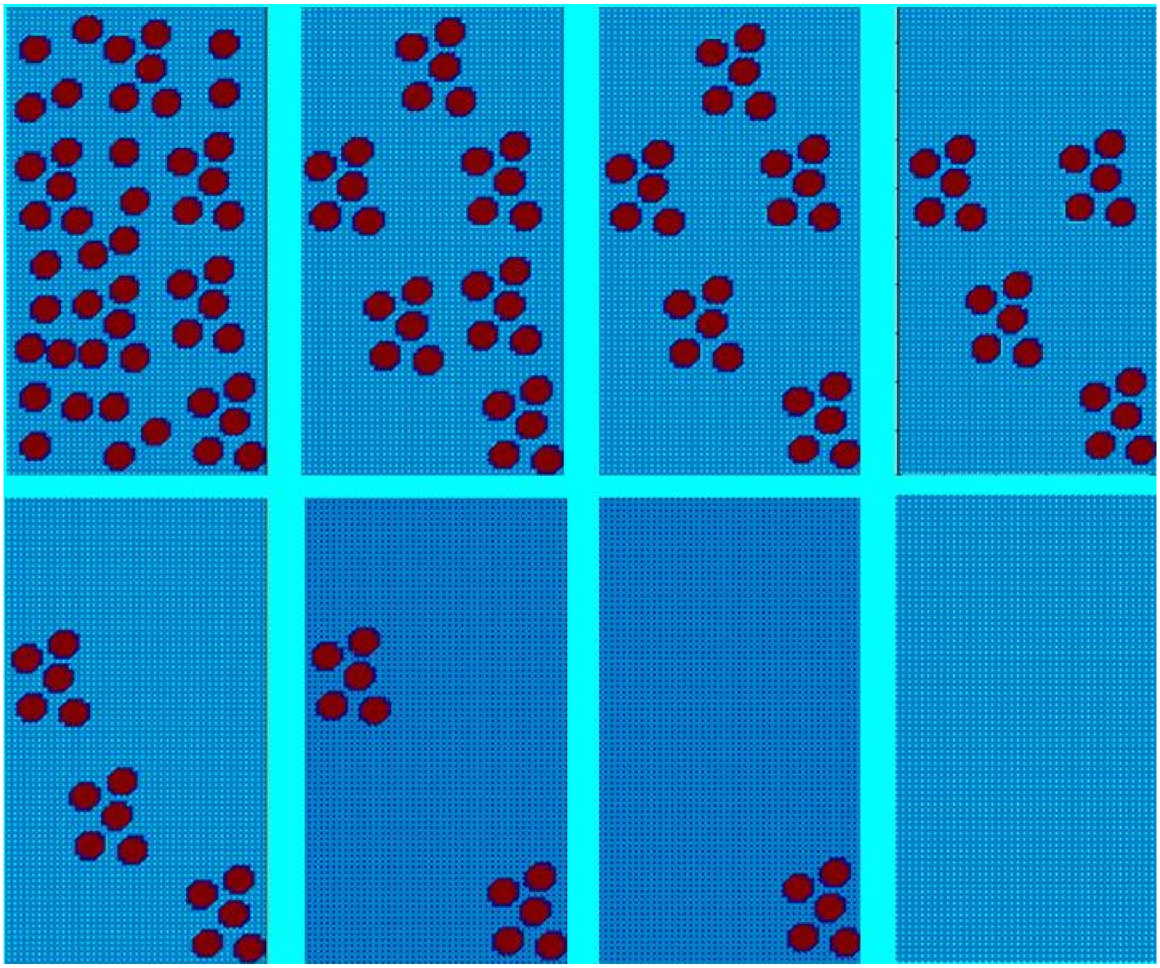

Figure 5. 12 Simulation domains with varying vuggy pore space amout

Also evaluated was the up-scaled domain permeability in each scenario. In the previous section it was illustrated that vugs affect the up-scaled permeability if they are well connected. An interesting finding here is that although the presence and amount of vugs does not change the effective permeability of the formation (1% decrease from case 1 to case 8), it could highly effect fluid diversion. **Fig. 5.13** clearly illustrates this point. We think this is a very important observation for designing of multi layer stimulation.

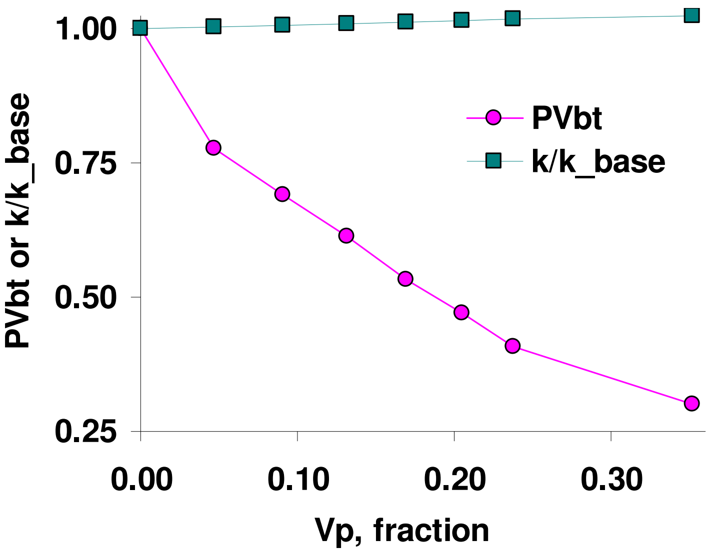

Figure 5. 13 Effect of vuggy pore space fraction on *PVbt*

For clarity we will follow same logic with a simpler domain. **Fig. 5.14** illustrates the domain. The effluent concentration curves for these domains were given in **Fig. 5.15**.

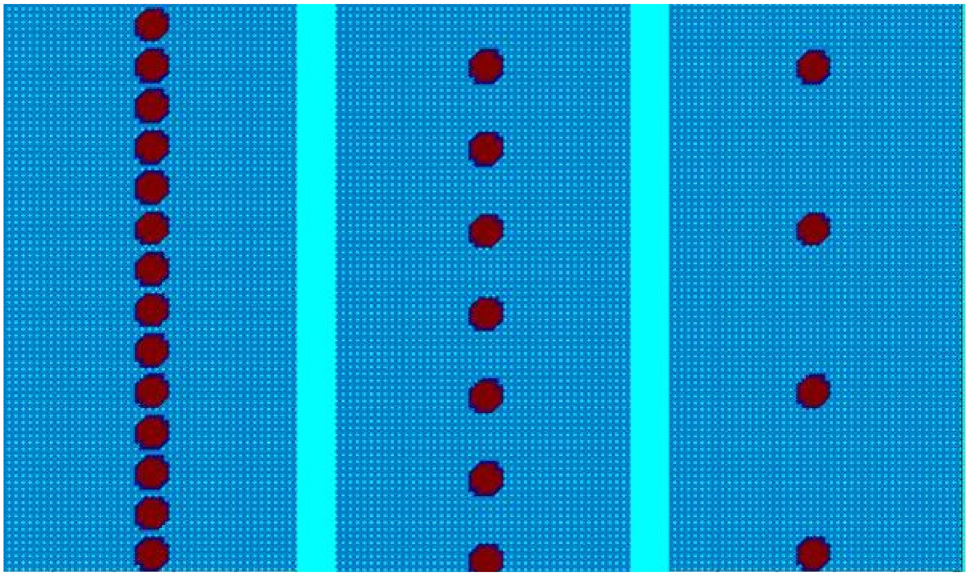

Figure 5. 14 Simplified simulation domains with varying vuggy pore space amout

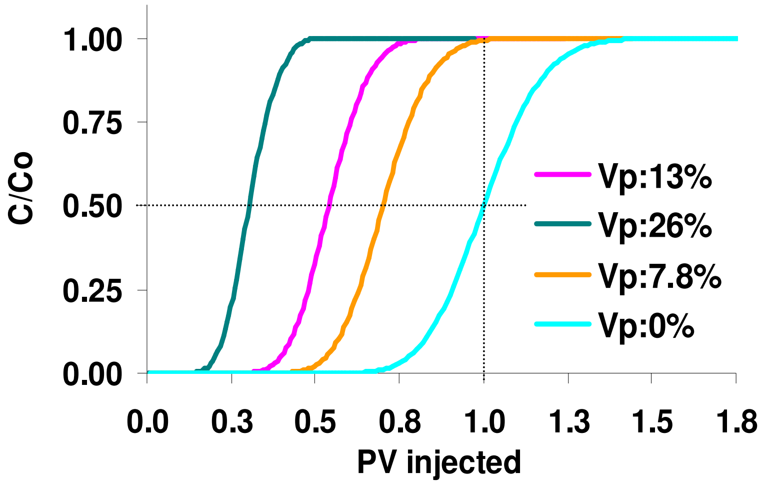

Figure 5. 15 Dimensionless effluent concentration for domains given in Fig. 5.14

These two examples illustrate that the total amount of vuggy pore space has significant impact on *PVbt*. Next we investigated the effect of the spatial distribution of vugs, keeping the total amount of vug constant.

5.6.2 Effect of spatial distribution of vugs on PVbt

When the permeability is highly heterogeneous, or there are vugs and fractures, the injected fluid may tend to proceed following preferential paths, instead of moving in a piston-like fashion (**Fig. 5.16**).

Permeability and porosity are not completely randomly distributed, instead they are spatially correlated. In order to quantitatively analyze the effect of spatial distribution of vugs on *PVbt* we simulated 3 cases by modifying the first domain given in **Fig. 5.14**: i) vugs are spatially well correlated with correlation strength~1 in main flow direction, ii) vugs are less correlated with correlation strength ~0.5 in main flow direction, and iii) vugs are not correlated in main flow direction (**Fig. 5.17**).

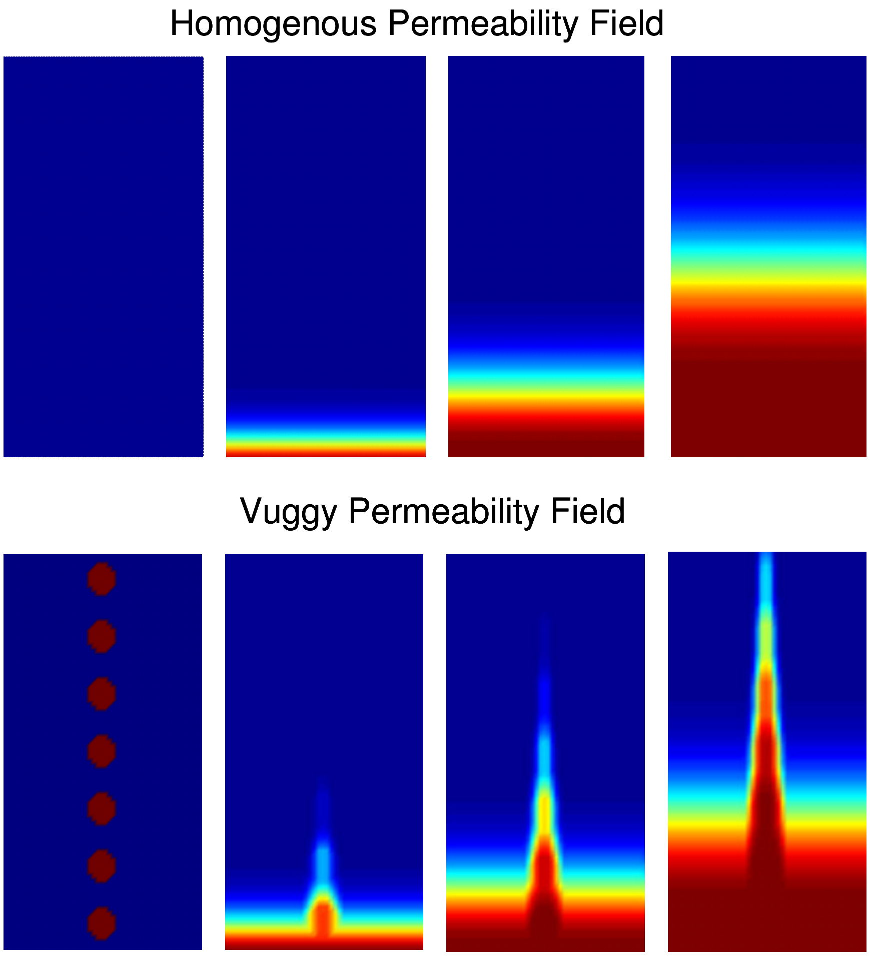

Figure 5. 16 Piston like displacement (homogenous permeability), and preferential flow (vuggy/heterogeneous permeability)

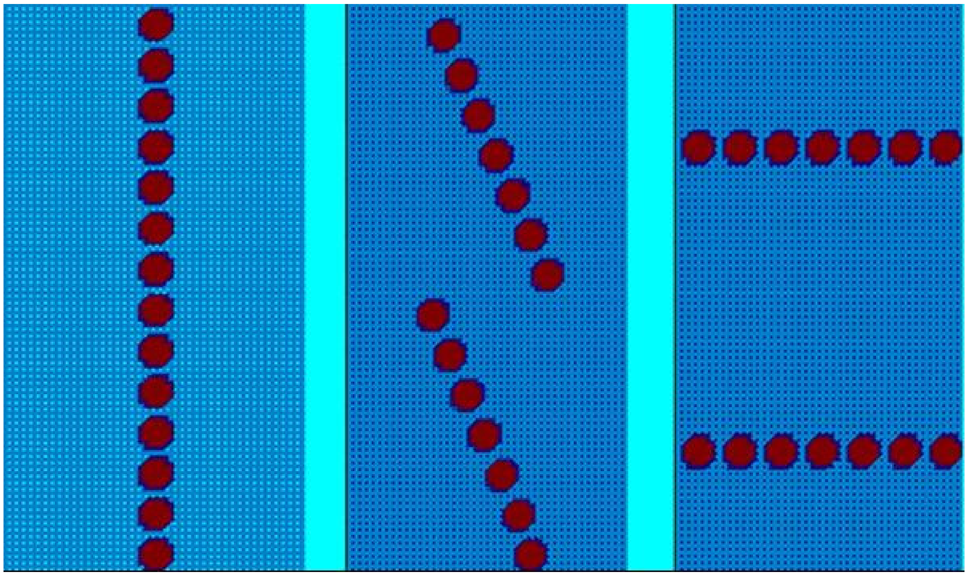

Figure 5. 17 Simulation domains with varying correlation strength of permeability

Fig. 5.18 gives the dimensionless effluent concentration observed in these numerical experiments. The main observation here is that from high correlation strength to low correlation strength *PVbt* decreases (**Fig. 5.19**). This point was made previously with a simple logic presented in **Fig. 3.7**. A single vug acts as a high permeability streak in the region. As the correlation strength of the distribution of theses vugs increases, this highly correlated vug distribution creates a continuous pressure disturbance and a local high velocity path act as a high permeability streak (or a fracture) depending on the distance between vugs.

In these experiments, a 15% increase in domain permeability was observed between lowest correlation and highest correlation cases.

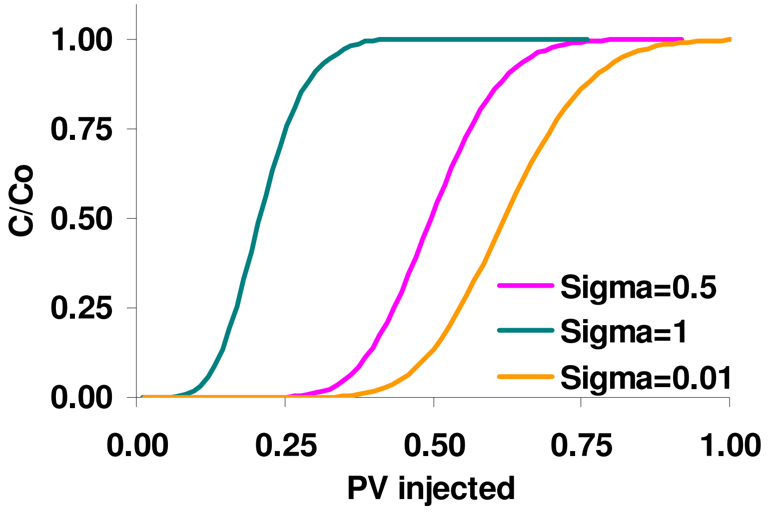

Figure 5. 18 Effluent concentration for domains given in Fig. 5.17

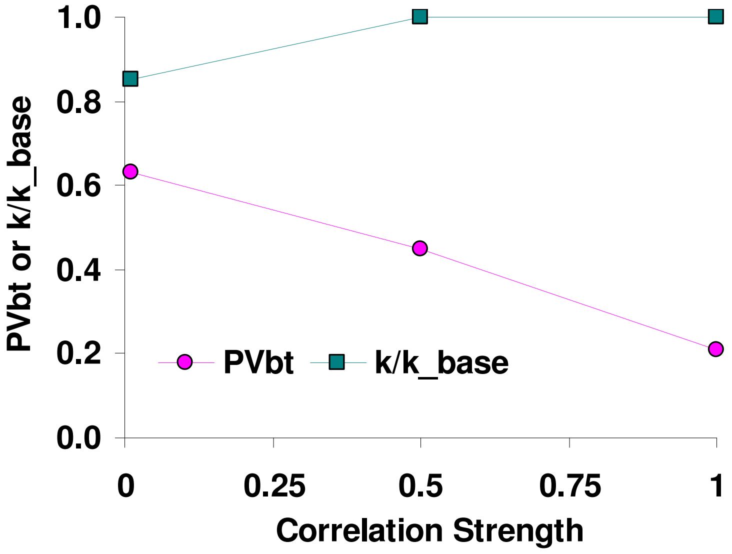

Figure 5. 19 Effect of spatial distribution of vugs on *PVbt*

5.6.3 Effect of size of vugs on PVbt

We also studied the effect of the size of the vugs on *PVbt*. Simply as the size of the vugs increases, the total amount of pore space occupied by matrix and the distance between vugs decreases. One more time we build our analysis on a simple simulation domain given in the previous analysis. 4 simulations were conducted, with vugs having biggest size to smallest sizes (**Fig. 5.20**). The measured effluent concentration histories and observed *PVbts* are given in **Figs. 5.21 and 5.22**. Apparently the size of the vugs brings about a similar effect observed in the number of and distance between the vugs cases.

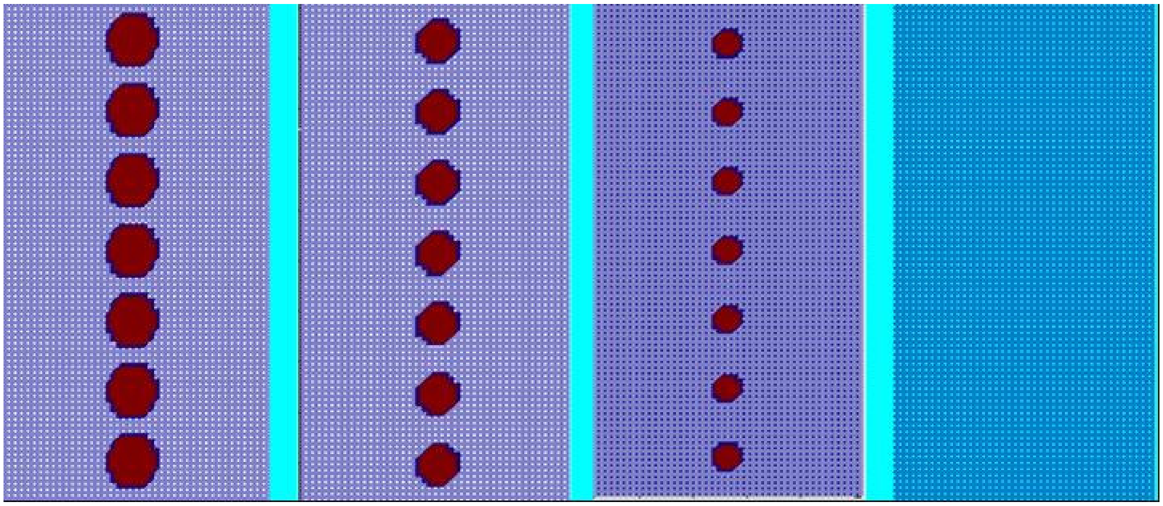

Figure 5. 20 Simulation domains with varying vug sizes

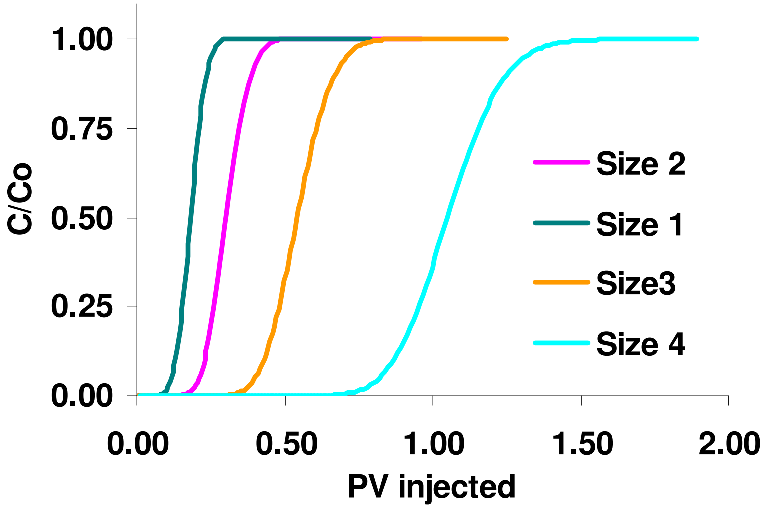

Figure 5. 21 Dimensionless effluent concentration for domains given in Fig. 5.20

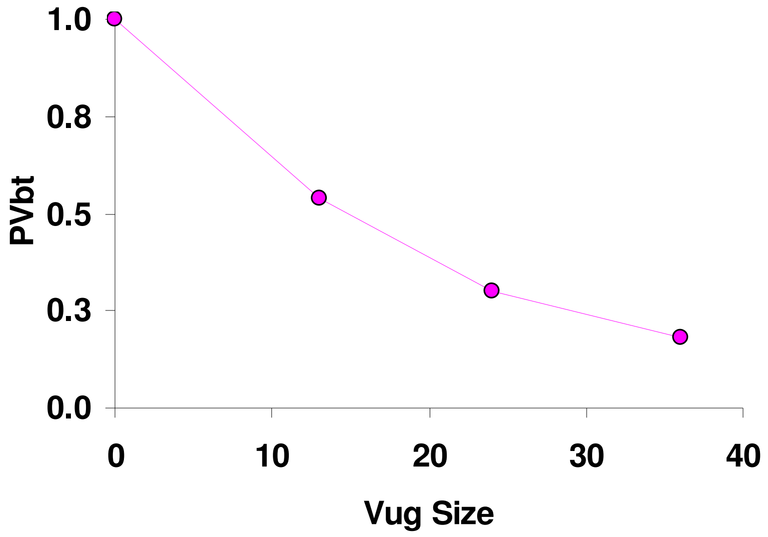

Figure 5. 22 Effect of sizeof vugs on *PVbt*

5.7 USE OF STREAMLINES

We implemented the proposed code in 3D and used streamline visualization to better understand the flow in touching vug network. Below is an example of this study using a vug network extracted from a real vuggy rock using the CCL algorithm. It was observed that in some parts of the network, fluid moved laterally; this is because of the existence of the “dead-end” vugs. Another observation here is that radius of the network has a great effect on fluid velocity.

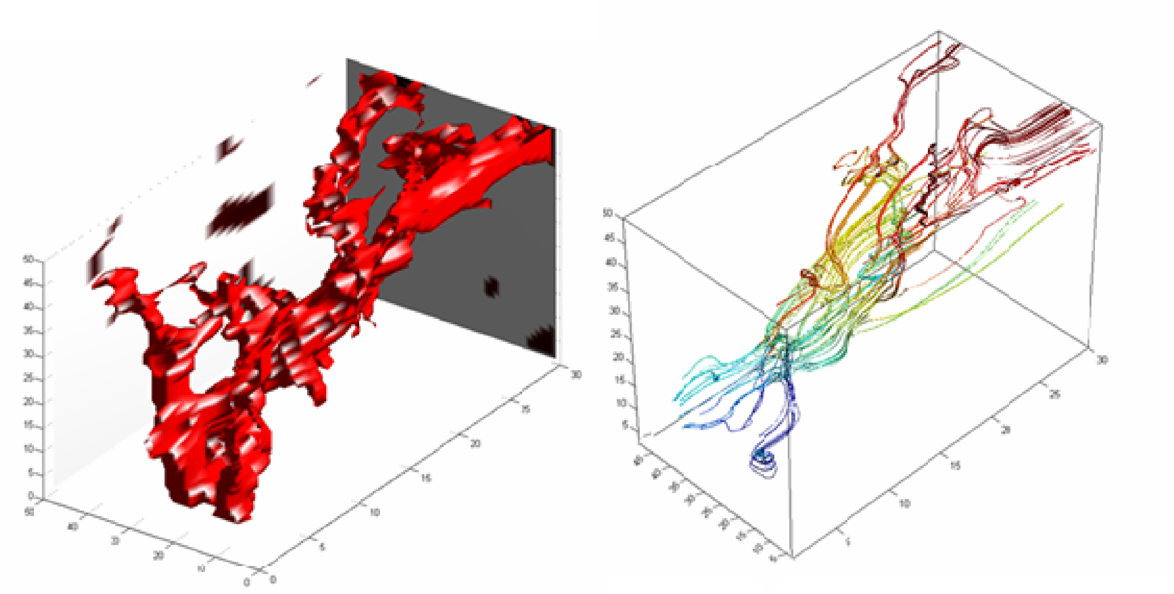

Figure 5. 23 Vug network extracted from a real vuggy carbonate rock (left), and corresponding velocity streamlines (right)

5.8 CHAPTER OBSERVATIONS AND SUMMARY

The effect of the existence of separate vugs on fluid flow was studied using the numerical simulator. It was observed that a single separate vug creates as high flow velocity channel acting as a high permeability streak. Three important parameters, total amount, size, and spatial distribution of vugs, were analyzed.

An interesting finding of this study is that although the presence and amount of vugs does not change the effective permeability of the formation a lot, it could highly effect fluid diversion.

Apparently the size of the vugs brings about a similar effect as it is observed in the number of and distance between the vugs cases.

As previously discussed, vuggy porosity can be divided into separate and touching vugs. While connectivity of the vugs affects storage capacity (porosity) little, its effect on permeability might be drastic. In our separate vug numerical experiments ~15% increase in domain permeability was observed between the lowest correlation and the highest correlation cases, which is in accord with Moctezuma-Berthier et al.'s (2004) study. Moctezuma-Berthier et al. (2004) performed a study on artificial bimodal porous media. They reported that single-phase permeability depended on the correlation of the small pores when the vugs are not percolated (non-touching). In that case, micropores (matrix permeability) are the main percolating system. In the percolated vug case, (touching vug network) effective permeability also depends on density of the vugs (size and amount).

CHAPTER VI

FROM LABORATORY TO FIELD

Laboratory experiments showed that the response of vuggy rocks to acid is different than in carbonate rocks having less heterogeneity. We investigated this issue with geostatistical characterization of cores, laboratory acid core flood experiments, scientific visualization, image processing and numerical simulation. The results indicated the necessity of a detailed study to understand the heterogeneity of the formation. Lack of understanding may lead to poor acid treatment design which may result in creation of high conductive channels through gas or water zones.

Studies show that more than 35% of matrix treatment failed, or did not reach expectations (Sengul and Remisio 2002). In some cases excessive water production was reported because of the aforementioned reason. Another consequence of inappropriate design is pore collapse because of the over treatment. Optimized design gains much more attention when horizontal wells come to picture. Since the volume of acid to stimulate these wells is huge, a well designed acid treatment plan has great importance.

In this section, first we will focus on a volumetric model to scale up the laboratory results to field treatments. We will show the results in terms of improved skin factor with comparison to previous studies. This will clarify the importance of the laboratory studies, and the necessity of an integrated approach to better interpret the experimental results to be used in field scale.

6.1 USE OF LABORATORY RESULTS TO DESIGN FIELD TREATMENTS

As discussed in **Chapter I**, well characterization of type, mineral composition, porosity and permeability has significant importance on success of an acidizing treatment. The above methods are used in industry in addition to core analysis for this purpose.

The next important step for success in treatment design is to understand all the relevant physics and chemistry occurred during flow and transport of acid in the formation. We aimed to do so with acid core-food experiments, high resolution CT scanning, geostatistical characterization, scientific visualization and numerical modeling.

All these efforts would remain worthless if the results are not scaled-up to the field size. In this section we demonstrate the use of a simple volumetric model to understand the importance of our results. First the derivation of the volumetric model is detailed. Following this, wormhole propagation distance will be calculated as a function of injected acid volume. Next, the corresponding skin factor (as a function of injected volume) will be calculated. For this purpose a skin model will be derived based on the well-known Hawkins' formula. In order to compare and contrast, the results will be presented together with the data reported in previous studies.

6.1.1 Volumetric wormhole model

The implication for field acid treatments of the very low pore volumes to breakthrough found for acidizing in vugular carbonates is that wormholes can propagate much farther into the formation in vugular sections of formations than in more homogeneous rocks.

Using the simple volumetric model (Economides et al. 1994) of wormhole propagation in radial flow around a well, the radius penetrated by wormholes for a given volume of acid injected can be calculated.

To begin with, acid capacity number, N_{AC}, is defined as *"the ratio of the amount of mineral dissolved by the acid occupying* ***a unit volume*** *of rock pore space to the amount present in* ***the unit volume*** *of the rock"* (Economides et. al 1994). It can be represented by

$$N_{AC} = \frac{\phi \beta C_{acid}^{0} \rho_{acid}}{(1-\phi) V_{m}^{0} \rho_{\min eral}} \tag{6.1}$$

where;

$\phi =$ *porosity*

$\beta =$ *acid dissolving power on the* min*eral*

$C_{acid}^{0} =$ *initial concentration of the acid*

$\rho_{acid} =$ *density of acid*

$\rho_{\min eral} =$ *density of* min*eral*

$V_{m}^{0} =$ *initial volume fraction of the* min*eral*

so, $N_{AC}.PV_{acid}$ will give the amount of the mineral dissolved behind the acid front where PV_{acid} corresponds to pore volume of acid injected. *PVbt* (the number of pore volumes of acid injected at the time of wormhole breakthrough at the end of the core) can be detected easily from core-flood experiments. We can now define wormholing efficiency, η, as the fraction of the rock dissolved in the region penetrated by acid as:

$$\eta = N_{AC} PVbt \tag{6.2}$$

For a radial system we can write the number of pore volumes of acid injected as:

So;

$$PV_{acid} = \frac{V_{acid}}{\pi(r_{wh}^{2} - r_{w}^{2})h\phi} \tag{6.3}$$

Combining Eqs. 6.2 and 6.3,

$$\eta = \frac{N_{AC} V_{acid}}{\pi(r_{wh}^{2} - r_{w}^{2})h\phi} \tag{6.4}$$

Using Eqs. 6.3 and 6.4, finally we obtain:

$$r_{wh} = \sqrt{r_w^2 + \frac{N_{AC} V_{acid}}{\eta \pi \phi h}} \tag{6.5}$$

or in another form:

$$r_{wh} = \sqrt{r_w^2 + \frac{V_{acid}}{PVbt \pi \phi h}} \tag{6.6}$$

Using the pore volumes to breakthrough from this study and comparing the predictions with the values obtained in homogeneous carbonates gives the comparison shown in **Fig. 6.1.** In these calculations well-bore radius, porosity, damaged region radius and permeability and original permeability was given by 0.328, 0.3, 2, 30, and 80 respectively. **Fig. 6.1** clearly illustrates that much deeper penetration of wormholes is predicted for the vugular rock with low pore volumes to breakthrough compared to the homogeneous cases with *PVbt* close to one.

Using this information and Hawkins' formula evolution of skin by time can be calculated.

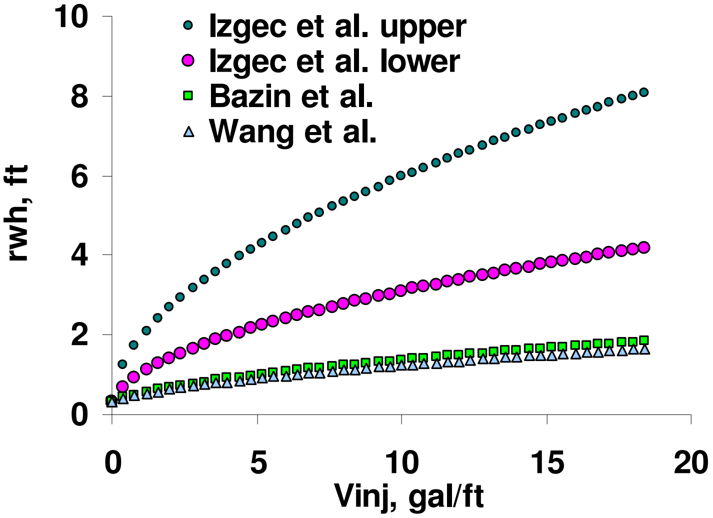

Figure 6. 1 Volumetric model: wormhole radius as a function of injected acid

6.1.2 Skin calculations

Skin is a dimensionless factor calculated to evaluate the production efficiency of a well by comparing actual conditions with theoretical or ideal conditions. A positive skin value indicates some damage or influences that are impairing well productivity. A negative skin value indicates enhanced productivity, typically resulting from well stimulation.

Fig. 6.2 shows the typical regions around a damaged and stimulated well.

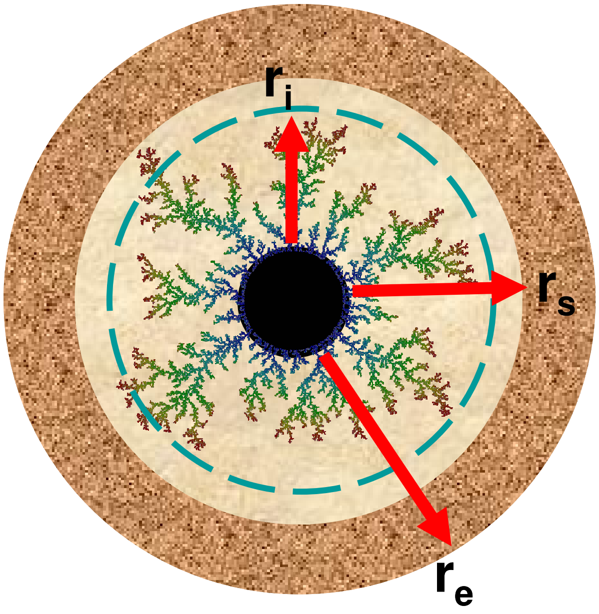

Figure 6. 2 Schematic representation of the near well bore region with damaged, acidized and original formation

In this figure r_s, r_{wh}, and r_e represents radius of damage, improved (wormholed) zone and drainage volume.

If the near-wellbore permeability is the reservoir permeability (i.e., no damage), then a steady-state pressure drop between the outer boundary pressure (p_e) and the well would result in a $p_{wf,\ ideal}$ given by

$$p_e - p_{wf,ideal} = \frac{q\mu}{2\pi kh} \ln \frac{r_e}{r_w} \tag{6.7}$$

If there is damage near the wellbore, a penalty term (skin) should be added to account for extra pressure drop. This leads to

$$p_e - p_{wf,real} = \frac{q\mu}{2\pi kh} \ln\left(\frac{r_e}{r_w} + s \right) \tag{6.8}$$

Considering the **Fig. 6.1** we can write the pressure drop from drainage radius to wellbore as

$$p_e - p_{wf,real} = \frac{q\mu}{2\pi k_{wh} h}\left(\frac{\ln r_{wh}}{r_w}\right) + \frac{q\mu}{2\pi k_s h}\left(\frac{\ln r_s}{r_{wh}}\right) + \frac{q\mu}{2\pi k h}\left(\frac{\ln r_e}{r_s}\right) \tag{6.9}$$

Equating Eqs. 6.8 and 6.9 we obtain

$$\frac{q\mu}{2\pi k h}\ln\left(\frac{r_e}{r_w} + s\right) = \frac{q\mu}{2\pi k_{wh} h}\left(\frac{\ln r_{wh}}{r_w}\right) + \frac{q\mu}{2\pi k_s h}\left(\frac{\ln r_s}{r_{wh}}\right) + \frac{q\mu}{2\pi k\ h}\left(\frac{\ln r_e}{r_s}\right) \tag{6.10}$$

Re-arranging

$$s = \ln\left(\frac{r_{wh}^{k/k_{wh}}}{r_w^{k/k_{wh}}}\right) + \ln\left(\frac{r_s^{k/k_s}}{r_{wh}^{k/k_s}}\right) + \ln\frac{r_e}{r_s} - \ln\frac{r_e}{r_w} \tag{6.11}$$

which can be written by

$$s = \left(\frac{k}{k_{wh}} - \frac{k}{k_s}\right)\ln r_{wh} + \left(\frac{k}{k_s} - 1\right)\ln r_s + \left(1 - \frac{k}{k_{wh}}\right)\ln r_w \tag{6.12}$$

Considering wormholing in carbonate acidizing, we can take improved permeability, k_{wh} , sufficiently large. Then;

$$s = \frac{k}{k_s}\ln\frac{r_s}{r_{wh}} - \ln\frac{r_s}{r_w} \tag{6.13}$$

Eq. 6.13 applies until the radius of wormhole penetration exceeds the radius of damage. Later, as $k_s \sim \infty$ this equation becomes:

$$s = -\ln \frac{r_{wh}}{r_w} \tag{6.14}$$

Using these expressions and the volumetric model (Economides et al. 1994), the evolution of skin as a function of injected acid is plotted for the experimental results obtained in this study compared to previously published ones (**Fig 6.3**). We used previously published data (Wang et al. 1993 and Bazin et al. 1996) together with the data obtained from this study. For clarity we only used the "best" and "worst" *PVbt* values observed in our experiments. Here best corresponds to smallest. This simple calculation and presentation, by illustrating practical field application, underlines the significance of the observed contrast between experimental results using vuggy cores and previously used homogenous ones.

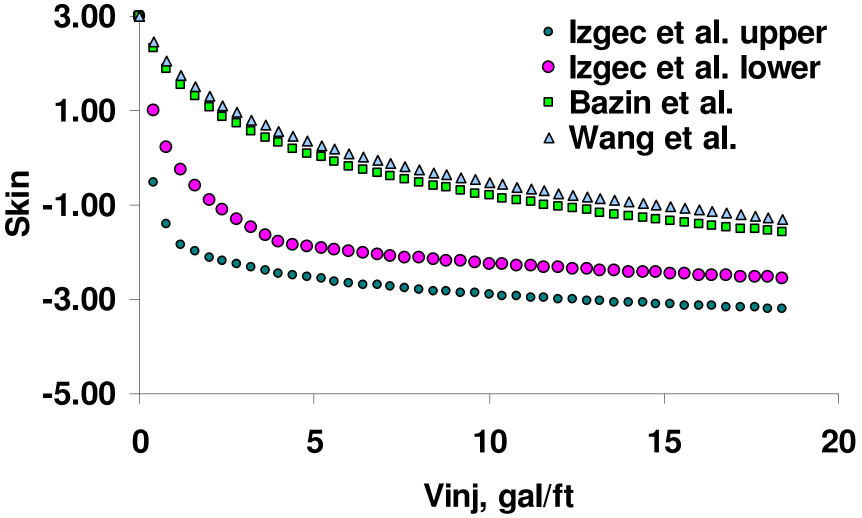

Figure 6. 3 Evolution of skin as a function of injected acid and wormhole radius

6.2 CHAPTER OBSERVATIONS AND SUMMARY

The implication for field acid treatments of the very low pore volumes to breakthrough found for acidizing in vugular carbonates is that wormholes can propagate much farther into the formation in vugular sections of formations. A volumetric model was derived and used to illustrate this point. While previously reported *PVbt* corresponds to 5-6 ft of wormhole propagation distance with 30 gal/ft injection of acid, with same amount of acid 15-35 ft wormhole radius is observed using the *PVbt* observed in our experiments.

An equivalent skin relation, based on Hawkins' formula, was derived using the pressure drop behavior around well bore. This relation was used with calculated wormhole radius (from volumetric model) to quantify the skin factor as a function of acid injection. For the vugular rock with *PVbt* of 0.040, 5 gal/ft injection of acid would result in a skin factor of about ~ -2.56 from original damaged skin of 3 while *PVbt* of 1.000 observed in homogenous cores brings about a improved skin of 0.30 only, under same conditions. Other wormhole models, such as that of Buijse and Glasbergen (2005) would predict somewhat smaller wormhole penetrations for both the vugular and the homogeneous cases compared with the volumetric model, but would predict the same order of magnitude of difference between the vugular and homogeneous cases.

CHAPTER VII

CONCLUSIONS

This study presents an integrated theoretical and experimental study on acidization of vuggy carbonates. The most important technical contribution of this study is development of a new understanding of the effect of large scale heterogeneities in matrix acidizing. Our approach combines core flood experiments with 4-inch by 20-inch vuggy carbonate cores, high resolution computerized tomography scanning, scientific visualization, image processing and mathematical modeling. Important developments and conclusions can be summarized as:

1. A workflow was proposed to characterize the vuggy carbonates prior to the core-flood acidizing experiments. The method incorporates conventional geostatistical functions and an image processing algorithm known as connected component labeling.
2. A complete procedure was presented to efficiently use the data from CT scanner to visualize the inner structure of the core. The method requires use of several commercial programs with the proposed techniques. These procedures result in a very detailed visualization of acid created wormholes via CT scanner. This is the very first study that we can see most of the details of acid created wormholes, and leading preferential paths.
3. Acid injected into vuggy limestones follows a preferential pathway guided by the vug network. This path can be predicted from the distribution of vugs in the samples as measured by CT scans on the cores before acid injected. This preferential flow path allows the acid to propagate wormholes though the rock with a very small volume of acid injected.
4. The number of pore volumes of acid solution injected to propagate a wormhole through the entire core sample (*PVbt*) in our experiments with vugular limestone

was very low, ranging from 0.04 to 0.15, an order of magnitude lower than what has been observed with relatively homogeneous limestones.

5. The *PVbt* for vuggy limestone correlates inversely with the fraction of total porosity comprised by vugs – the higher the vuggy fraction of porosity, the lower the pore volumes to breakthrough. The fraction of the porosity comprised by vugs was readily obtained from analysis of a CT scan of the samples before acid injection.
6. It was observe that the local pressure drops created by vugs are more dominant in determining the wormhole flow path than the chemical reactions occurring at the pore level.
7. A numerical model was developed coupling porous media flow principles (Darcy's law) and tube flow (Stokes' equation). The so-called Darcy-Brinkman formulation was used in the numerical model. The power of DBF lies in its natural ability to represent both porous media and free flow in a single equation with variable coefficients. The advantage of this formulation is that there is no need to specify different boundary and interface conditions.
8. The effect of the existence of separate vugs on fluid flow was studied using the numerical simulator. It was observed that a single separate vug creates as high flow velocity channel acting as a high permeability streak. Three important parameters, total amount, size, and spatial distribution of vugs were analyzed. An interesting finding of this study is that although the presence and amount of vugs do not change the effective permeability of the formation a lot (~1%), they could highly effect fluid diversion. Apparently the size of the vugs brings about a similar effect as it is observed in the number of and distance between the vugs cases. In our separate vug numerical experiments a ~15% increase in domain permeability was observed between the lowest correlation and highest correlation cases.

9. A volumetric model was used to underline the importance of the observed early *PVbt* in our experiments. This analysis clearly illustrated that much deeper penetration of wormholes is predicted for the vugular rock with low pore volumes to breakthrough compared to the homogeneous cases with *PVbt* close to one. For the vugular rock with *PVbt* of 0.040, 5 gal/ft injection of acid would result in a skin factor of about ~ -2.56 from original damaged skin of 3 while *PVbt* of 1.000 observed in homogenous cores brings about a improved skin of 0.30 only, under same conditions.

CHAPTER VIII

RECOMMENDATIONS FOR FOLLOW-UP WORK

Prior to this work acidization of vuggy carbonates was not studied in detail. Still there are some areas to be investigated both experimentally and theoretically. I think the following items have great importance:

1. More experiments are needed to be conducted with varying injection rate to be able to generate *PVbt* curves. Also in order to complete the picture, more experiments should be conducted with vuggy carbonate samples having different degrees of vuggy pore space.
2. All the experiments presented in this study were conducted using samples having separate vugs. We attempted to conduct experiments with highly vuggy samples, having touching vug networks. Mobilization of sediments in these vugs did not let us to reach a steady state flow. A procedure should be developed to avoid particle mobilization, thus plugging. This kind of experiments would help to answer several important questions: What happens when acid flow in a vug network having many dead-end vugs? Are these dead end volumes enlarged by time and divert more acid from the main flow path by becoming thief zones? If it was true, can we avoid this mechanism by injecting the acid with high flow rate? What would happen if we damage the core by injecting drilling fluid to these vug networks and then acidize the samples?
3. Parallel core-flood experiments would be a good extension to this study. Numerical experiments showed that although the amount of vuggy space does not affect effective permeability, it changes *PVbt* drastically. The theory presented here should be helpful in interpreting these kinds of experiments.
4. Use of self diverting acids in vuggy carbonate formation would be a good investigation topic.

5. To represent vugs, artificial holes can be drilled to homogeneous carbonate cores. This would give the experimentalist a control to design experiments and investigate several aspects isolated.
6. The transport model presented here uses a single value for dispersivity, both in the porous media and the vuggy region. Using varying dispersivities would add more physics to the current model, thus leading to better interpretation of effluent concentration.
7. With this study, non-reactive flow and transport in vuggy carbonates were well understood. Adding chemical reactions to the model, reactive dissolution of porous media in the presence of vugs should be studied as an extension.
8. Flow in large vugs would bring about high Reynold's number, thus the necessity to model turbulent effects. This feature should be added to the current model to study the flow in touching vug networks or fractures. In that case, practical difficulty would be necessity for very high computational power.
9. More vuggy porous media scenarios, such as stochastic vug distributions, should be tested to come up with guidelines to acidize vuggy carbonates.

NOMENCLATURE

a=intercept of the linear equation relating CTN and bulk densities, dimensionless

b=slope of the linear equation relating CTN and bulk densities, dimensionless

CTN=computerized tomography number, dimensionless

Cv=coefficient of variation, dimensionless

C=fluid concentration, M/L^3

$\overline{C}$ *=average fluid concentration,* M/L^3

C^0_{acid} *=initial concentration of the acid*

D_m*=molecular diffusion,* L^2/t

D_L*=longitudinal dispersion,* L^2/t

D_T*=transverse dispersion,* L^2/t

d_i*=separation distance between variogram pairs, L*

F=formation resistivity factor

f_e*=external forces acting on unit volume, p/L*

h=distance between parallel plates, thickness of the formation or object, L

I_0*=intensity of the incident, Hounsfield*

I=intensity of the detected X-ray beams, Hounsfield

J=diffusive flux, L/t

k=permeability, mD or L^2

k_s*=damaged region permeability, mD or* L^2

k_{wh}*=stimulated region permeability, mD or* L^2

L=Length in main flow direction, L

m=a constant appeared in dispersion relation

N=number of pairs in variogram, dimensionless

N_{AC}*=acid capacity number, dimensionless*

N_{Re}= Reynolds number, dimensionless

p=pressure, p

p_e=outer boundary pressure, p

$p_{wf,ideal}$=bottom-hole flowing pressure in ideal conditions, p

$PVbt$=pore volume to breakthrough of fluid, dimensionless

Pe=Péclet number, dimensionless

r_w=well-bore radius, L

r_e=drainage radius, L

r_s=damaged region radius, L

r_{wh}=wormhole propagation radius, L

r_{core}=radius of the core, L

s=skin factor, dimensionless

V_m^0=initial volume fraction of the mineral, dimensionless

u_i=interstitial velocity, L/t

u_x=fluid velocity in x-direction, L/t

u_y=fluid velocity in y-direction, L/t

u_z=fluid velocity in z-direction, L/t

$\vec{u}$=fluid velocity vector, L/t

q=fluid flow rate, L^3/t

Δx=distance in x-direction, L

Δy=distance in y-direction, L

Δz=distance in z-direction, L

Δt=time period, t

ξ=mean attenuation coefficient, dimensionless

ξ_w=attenuation coefficient of water, dimensionless

$\emptyset$=porosity, fraction

$\emptyset_{i,j}$=porosity of the voxel i,j, fraction

$\emptyset_s$=porosity of the sample, fraction

μ_e=*effective fluid viscosity, p-t*

μ=*dynamic fluid viscosity, p-t*

ρ_{acid}=*density of the acid, M/L*^{3}

$\rho_{mineral}$=*density of the mineral, M/L*^{3}

$\rho_{matrixl}$=*density of the mineral, M/L*^{3}

ρ_{bulk}=*bulk density, M/L*^{3}

ρ_{fluid}=*fluid density, M/L*^{3}

α_L= *longitudinal hydrodynamic dispersivity, L*

α_T *transverse hydrodynamic dispersivity, L*

β=*a lumped parameter in DBF or acid dissolving power of the mineral*

η=*wormholing efficiency, dimensionless*

γ_{XY}=*variogram function*

SubSubscripts

s=sample

i=position index

j=position index

0=initial condition

n=time index

REFERENCES

Ahr, W.M. 2008. *Geology of Carbonate Reservoirs.* New York, USA: John Wiley & Sons.

Archie, G.E. 1952. Classification of Carbonate Reservoir Rocks and Petrophysical Considerations. *AAPG Bulletin*. 36, 278-298.

Akin, S., Kovscek, A.R. 2003. Computed Tomography in Petroleum Research. In: Mees, F., Swennen, R., Van Geet, M., Jacobs P. (eds.), Application of X-ray Computed Tomography in the Geosciences, 23-28, Geological Society of London, London, UK.

Arbogast, T., Brunson, D.S., Bryant, S.L., Jennings, J.W. 2004. A Preliminary Computational Investigation of a Macro Model for Vuggy Porous Media. *Computational Methods in Water Resources XV.* C.T Miller et al., eds., Elsevier, New York, USA.

Bartko, K.M., Newhouse, D.P., Andersen, C.A., Treinen, R.J. 1995. The Use of CT Scanning in the Investigation of Acid Damage to Sandstone Core. Paper SPE 30457 presented at the 69th SPE Annual Technical Conference and Exhibition, Dallas, TX, 22-25 October.

Auzerais, F.M., Dussan, E.B., Reischer, A.J. 1991. Computed Tomography for the Quantitative Characterization of Flow Through a Porous Medium. Paper SPE 22595 presented at the 65th SPE Annual Technical Conference, Dallas, Texas, 6-9 October.

Bazin, B., Bieber, M.T., Roque, C., Boutéca, M. 1996. Improvement in the Characterization of the Acid Wormholing by “In Situ” X-Ray CT Visualizations. Paper SPE 31073 presented at the SPE International Symposium on Formation Damage Control, Lafayette, Louisiana, 14-15 February.

Brinkman, H.C. 1947. A Calculation of the Viscous Force Exerted by a Flowing Fluid on a Dense Swarm of Particles. *Applied Scientific Research.* A1, 27-34.

Buijse, M.A. 1997. Mechanisms of Wormholing in Carbonate Acidizing. Paper SPE 37283 presented at SPE Int. Sym. On Oilfield Chemistry. Houston, Texas. 18-21 February.

Buijse, M.A., Glasbergen, G. 2005. A Semi-empirical Model to Calculate Wormhole Growth in Carbonate Acidizing. Paper SPE 96892 presented at SPE Annual Technical Conference and Exhibition, Dallas, Texas, 9-12 October.

Chaudhari, N.M. 1971. An Improved Numerical Technique for Solving Multidimensional Miscible Displacement Equations. *SPEJ* **3**(11): 277-284.

Crary. S., Dennis, R., Denoo, S. 1987. Fracture Detection with Logs. *Tech. Rev.* **35**, 22-34.

Cunningham, K.J., Carlson, J.I., Hurley, N.F. 2003. New Method for Quantification of Vuggy Porosity from Digital Optical Borehole Images as Applied to the Karstic Pleistocene Limestone of the Biscayne Aquifer, Southeastern Florida. *Journal of Applied Geophysics.* **55**(1): 77-90.

Daccord, G. 1987. Chemical Dissolution of a Porous Medium by a Reactive Fluid. *Physical Review Letters* **58** (5): 479.

Durlofsky, L. Brandy, J.F. 1987. Analysis of the Brinkman Equation as a Model for Flow in Porous Media. *Phys. Fluids* **30**: 3329-3341.

Economides, M.J., Nolte K.G. 2000. *Reservoir Stimulation,* John Willey & Sons, West Sussex, England.

Economides, M.J., Hill, A.D., Ehlig-Economides, C.E. 1994. *Petroleum Production Systems.* New Jersey, USA: Prentice-Hall.

Fox, R.W., McDonald, A.T. 1998. *Introduction to Fluid Mechanics*, 5th ed., New York, USA: John Wiley & Sons.

Frick, T.P., Kurmary, M., and Economides, J.M. 1994. Modeling of Fractal Patterns in Matrix Acidizing and their Impact on Well Performance. *SPE Production&Facilities.* 61-68, February.

Fried, J.J. and Combarnous, M.A. 1971. Dispersion in Porous Media. *Adv. Hydro. Sci.* **7**:169-282.

Genty, C., Jensen, J.J., Ahr, W.M. 2007 Distinguishing Carbonate Reservoir Pore Facies with Nuclear Magnetic Resonance Measurements. *Natural Reseources Research* **16**(1), 45-54.

Genuchten, M.T., and Alves, W.J. 1982. Analytical Solutions of the One-dimensional Convetive-Dispersive Solute Transport Equation. *U.S Department of Agriculture, Technical Bulletin No.1661.*

Golfier, F., Zracone, C., Bazin, B., Lenormand, R., Lasseux, D., Quintard, M. 2002. On the Ability of a Dracy Scale Model to Capture Wormhole Formation During Dissolution of a Porous Medium. *Journal of Fluid Mechanics.* **457**: 213-254.

Goyeau, B., Benihaddadene, Gobin, D., Qunitard, M. 1997. Averaged Momentum Equation for Flow through a Non-homogenous Porous Structure. *Transport in Porous Media* **28**: 19-50.

Hidajat, I., Mohanty, K.K., Flaum, M., and Hirasaki, G. 2004. Study of Vuggy Carbonates Using NMR and X-Ray CT Scanning. *SPE Reservoir Evaluation and Engineering* October: 365-377.

Hoefner, M.L. 1988. Pore Evolution and Channel Formation During Flow and Reaction in Porous Media. *AIChE J.* **34:** 1: 45-54.

Honarpour, M.M., Cromwell, V., Hatton, D., Satchwell, R. 1985 Reservoir Rock Descriptions Using Tomography (CT). Paper SPE 14272 presented at the 60th SPE Annual Technical Conference and Exhibition, Las Vegas, NV, 22-25 September.

Hoopes, J.A., and Harleman, D.R.F. 1967. Dispersion in Radial Flow from a Recharge Well. *J.Geophys. Res.* **22:** 3595-3607.

Hounsfield, G.N. 1972. A Method of and Apparatus for Examination of a Body by Radiation such as X- or Gamma-Radiation. *British Patent No. 1,283,915.*

Huang, T., Hill, A.D., Schechter, R.S. Reaction Rate and Fluid Loss. 1997. The Keys to Wormhole Initiation and Propagation in Carbonate Acidizing. Paper SPE 37312 presented at SPE Int. Symposium on Oilfield Chemistry, Houston, TX, 18-21 February.

Hung, K.M., Hill, A.D., and Sepehrnoori, K. 1989. A Mechanistic Model of Wormhole Growth in Matrix Acidizing and Acid Fracturing. *Journal of Petroleum Technology,* **59** (1).

Isaaks, E.H., Srivastava, R.M. 1989. *An Introduction to Applied Geostatistics*. New York, USA: Oxford University Press.

Ketcham, R.A., Carlson, W.D. 2001. Acquisition, Optimization, and Interpretation of X-ray Computed Tomographic Imagery: Applications to Geosciences, *Computers and Geosciences* **27**(2001), 381-400.

Kwok, W., Hayes, R.E., Nasrl-El-Din, H.A. 1995. Dispersion in Consolidated Sandstone with Radial Flow. *Transport in Porous Media* **19:** 37-66.

Li, C., Xie, T., Pournik, M., Zhu, D., Hill, A.D. 2005. Fine-scale Simulation of Sandstone Acidizing, Journal *of Energy Resources Technology* **127**(3), 225-233.

Lucia, F.J. 1999. *Carbonate Reservoir Characterization.* Berlin, Germany: Springer-Verlag.

Lucia, F.J. 1983. Petrophysical Parameters Estimated from Visual Description of Carbonate Rocks: A Field Classification of Carbonate Pore Space. *Journal of Petroleum Technology* 2(35): 626-637.

Mostafizadeh, B., and Economides, M.J. 1994. Optimum Injection Rate from Radial Acidizing Experiments. Paper SPE 28547 presented at the 69th Annual Technical Conference and Exhibition, New Orleans, LA, 25-28 September.

Moctezuma-Berthier, A., and Fleury, M. 2000. Permeability Mapping on Vuggy Core Samples Using Tracer Experiments and Streamline Simulations. Paper SPE 58992 presented at the 75th SPE Annual Technical Conference, Villahermosam, Mexico, 1-3 February.

Moctezuma-Berthier, A., Vizika, O., Thovert, J.F., Adler, P.M. 2004. One- and Two-Phase Permeabilities of Vugular Porous Media. *Transport in Porous Media*. **56**(1), 225-244.

Nevito, J. 2006. Design, Set-up, and Testing of A Matrix Acidizing Apparatus. *MSc Thesis*, Texas A&M Univeriesty, College Station, USA.

Perkins, T.K., and Johnston, O.C. 1963. A Review of Diffusion and Dispersion in Porous Media, *SPEJ* **3**: 70-84.

Rubinstein, J. 1986. Effective Equations for Flow in Random Porous Media with a Large Number of Scales. *J.Fluid Mech* **170**: 379-383.

Schechter, R.S. 1992. *Oil Well Stimulation,* Prentice Hall, New Jersey, USA.

Sengul, M., Remisio, L.H.A. 2002. Applied Carbonate Stimulation – An Engineering Approach. Paper SPE 78560 presented at the 10th Abu Dhabi International Petroleum Exhibition and Conference, Abu Dhabi, 13–16 October.

Siddiqui, S., Khamees, A.A. 2004. Dual-energy CT-scanning Applications in Rock Characterization. Paper SPE 90520 presented at the 79th SPE Annual Technical Conference and Exhibition, Houston, TX, 26-29 September.

Tam, C.K. 1969. The Drag on Cloud of Spherical Particles in Low Reynolds Number Flow. *J.Fluid Mech.* **38**: 537-546.

Tardy, P.M.J., Lecf, B., Christanti, Y. 2007. An Experimentally Validated Wormhole Model for Self-Diverting and Conventional Acids in Carbonate Rocks Under Radial Flow Conditions. Paper SPE 107854 presented at the European Formation Damage Conference, Scheveningen, The Netherlands, 30 May-1 June.

Van Geet, M., Swennen, R. 2001. Quantitative 3D-fracture Analysis by Means of Microfocus X-ray computer Tomography (μCT): An example from Coal. *Geophysical Research Letters,* **28**: 3333-3336.

Van Geet, M., Swennen, R., Wevers, M. 2001. Towards 3D Petrography: Application of Microfocus Computer Tomograhy in Geological Science. *Computers&Geosciences* (**27**): 1091-1099**.**

Wang, Y., Hill, A.D., and Schechter, R.S. 1993. The Optimum Rate for Matrix Acidizing of Carbonate Formations. Paper SPE 26578 presented at the 68th SPE Annual Technical Conference, Houston, TX, 3-6 October 1993.

Wellington, S.L. and Vinegar, H.J. 1987. X-ray Computerized Tomography. *JPT* 1987, 885-898.

Withjack, E.M., Graham, S.K., Yang, C.T. 1991. CT Determination of Heterogeneties and Miscible Displacement Characteristics. *SPE Formation Evaluation* December 1991. 447-452.

Xu, B., Kamath, J., Lee, S.H. and Yortsos, Y.C. 1998. Use of Pore Network Models to Interpret Laboratory Experiments on Vugular Rocks. *Journal of Petroleum Science and Engineering* **4**(3):179-186.

Ziauddin, M., Bize, E. 2007. The Effect of Pore-Scale Heterogeneties on Carbonate Stimulation Treatments. Paper SPE 104627 presented at the 15th SPE Middle East Oil & Gas Show and Conference, Bahrain, Kingdom of Bahrain, 11-14 March.

Zhang, L., Bryant, S.L., Jennings, J.W., Arbogast, T.J., Paruchuri, R. 2004. Multi-scale Flow and Transport in Highly Heterogeneous Carbonates. Paper SPE 90336 presented at the 79th SPE Annual Technical Conference, Houston, Texas, 26-29 September.

Zhang, L., Nair, N., Jennings, J.W., Bryant, S.L. 2005. Models and Methods for Determining Transport Properties of Touching-Vug Carbonates. Paper SPE 96027 presented at the 80th SPE Annual Technical Conference, Dallas, Texas, 9-12 October.

APPENDIX A

PROCEDURE FOR CT SCANNING AND HIGH RESOLUTION 3D IMAGE CONSTRUCTION

From core preparation to 3D visualization CT scanning consist of 8 main steps:

1. Core preparation
2. Powering up CT scanner
3. Scanning core
4. Transferring data
5. Deleting files
6. Powering down CT scanner
7. Pre-processing the data and slice-based statistics
8. 3D visualization

CORE PREPARATION

For consistency the cores should be saturated with brine prior to the pre- and post-acidizing CT scanning. This will ensure that the pores, fractures, and vugs are filled with same fluid during both scanning. Be sure that you know the total length of the core to be scanned. You should know its length in terms mm. We will come to necessity of this step later.

POWERING UP CT SCANNER

1. Turn key to right on CPU (Computer on)
2. Wait until body icon appears on ELTP
3. Press any key when “press any key to continue” message appears
4. Wait 30 seconds.
5. Turn key to right again on SYST., and hold., view ready light and release the key. This will operate the Gentry.
6. Select SCANNER UTILITIES on touch pad.

7. This step is not compulsory. To check storage capacity, select IMAGE STORAGE STATUS. This will basically give you idea about the storage place left on the hard disk.
8. Select WARMUP, and then select START WARMUP. Warming up the device is required if the tube heat is less than 10% (can be read from the touch pad)
9. Wait until the WARMUP COMPLETE message appears
10. Select WARMUP, and select START WARMUP (anytime below 10% tube heat)
11. Wait until WARMUP COMPLETE message shows up

SCANNING CORE

If you know the length of the scanned sample, you can use the multiple scan option as follows:

1. Select return to SCANNER UTILITIES
2. Select TEST PROTOCOLS
3. Select HALF WATER
4. Select PROCEED WITH NEW STUDY
5. Press “ENTER TEXT” key in keybords
6. Type PATIENT NAME. This is the name you would like to give to this specific study.
7. Put ‘n’ in CONTRAST section. You can move directly to CONTRAST by hitting F1 key. Do not question, this is the way it works.
8. Hit F1 key to save data
9. Move core into the scanning plane.
10. Operate marker by hitting “marker” button. This red line showed the location to of the first CT slice. The table will move backwards, so be sure that you start scanning core from the desired initial point.
11. Close the door.
12. Select PROCEED TO PROTOCOL PARAMETERS

    Change SCAN PARAMETERS. These are the values you should define depending on the size of the object you would like to scan. My recommendation would be using 140 for 4-inch cores.

INDEX (Table movement) – 2 mm (device will take a slice, proceed 2 mm, and then take another slice)

THICKNESS (Slice thickness) – 2 mm (thickness of the X-ray. Should be close to INDEX value)

SCAN TIME – 4 sec

SCAN MA – 100

SCAN KV - 130

ii) For 4 inched core:

INDEX (Table movement) – 2 mm (device will take a slice, proceed 2 mm, and then take another slice)

THICKNESS (Slice thickness) – 2 mm (thickness of the X-ray. Should be close to INDEX value)

SCAN TIME – 4 sec

SCAN MA – 100

SCAN KV – 130

13. Select PROCEED TO PRE-SCAN
14. Select SCANNING MODE and type CURRENT VALUE (number of scans)
15. Select READY FOR SCAN
16. After MULTI-SCAN SERIES appear on the screen, hit START
17. You can check scanned images with PRIOR and NEXT keys

Let me illustrate these concepts with an example.

Suppose that we have 4x20 inches core sample. We want to scan this core with slices separated with 3 mm distance. 20 inches equals to 508 mm. Then we need 508/3~170 CT scans to cover the core. Your INDEX will be 3 mm and current value should be 170.

TRANSFERRING DATA FROM CT SCANNER TO SUN COMPUTER

1. Hit PT.DIR
2. Note the name of the study
3. Open the SUN computer in the room
4. Make a directory below Home/ct01/PROJECTS with the same name on PT.DIR.

Here are some useful commands:

cd.. – to go upper directory

cd *directoryname* – go to directory named *directoryname*

mkdir *directoryname* – make an directory named *directoryname*

pwd – print the working directory (the directory we are currently in)

ls – list the filed in the directory we are working in

So in order to create a directory you should type

mkdir *directoryname*

5. Go to directory you created in previous step

cd *directoryname*

6. Type HDTAMU_TRANSFER *directoryname*

TRANSFERRING DATA FROM SUN TO PC

You can use any FTP program to access the folders in the SUN. The IP of the computer, username and password are written on the computer. Don't expect me to give them here!

DELETING FILES IN THE CT SCANNER HARD DISK

1. Hit MAIN MENU and select Image Maintenance
2. Select delete images (F7)
3. Set mark (F3) on studies you want to delete
4. Select proceed (F1)
5. Select delete+go (F6)
6. Hold down Shift key + press PT.DIR to return
7. Hit PREV PAGE

CHANGING NAME OF A STUDY

1. Select RETURN TO SELECT PROTOCOL
2. Choose protocol (HALF WATER) and PROCEED WITH NEW STUDY
3. Hit PT.DIR and select the study

4. Select MAIN MENU and EDIT DATA PAGE
5. Type new name and press SAVE DATA (F1)

POWERING DOWN CT SCANNER

1. Select SCANNER UTILITIES
2. Select SYSTEM SHUTDOWN
3. Select SYSTEM POWERDOWN WITH DAILY MAINTENANCE
4. Wait till message "TURN KEY OFF TO COMPLETE SHUTDOWN SEQUENCE" appears
5. Turn OFF key

VISUALIZATION

This section is aimed to present the workflow developed in the scope of this study to construct 3D image of cores. Obtaining quality and detailed images (as given in **Appendix B** and **C**) require the use of multiple software and techniques. The first step is the pre-processing of the CT image. For this purpose VoxelCalc 9.56 was used in this study.

Pre-processing and slice-based statistics

1. Open VoxelCalc.
2. Go to file browser, choose the directory of CT scans (transferred from SUN) .
3. Click on the first CT slice, and shift+left mouse button on the last image to choose all images. Hit "Read" button.
4. In the the main workspace change "Order" from "Single Slice" to "Tile Horizontal". This will show all CT slices chosen.
5. Go to "ROI" menu and choose "Define ROI".
6. Using the left mouse button, draw the smallest circle inside the core.
7. Click "Clip" and "Fill Background".
8. Follow this sequence to create images for display: "Apply ROI", "Accept", and "Apply".

9. Go to “Color” menu and choose “Load Image Colors”.
10. Choose “Red Temperature” and hit dismiss. This is the best color table to use for carbonates and sandstones. Try other colors for individual preferences.
11. Refer to the VoxelCalc manual for slice-based statistics (histogram, orhoslab, cross plot).
12. Go to “Image File” menu and choose “Write fld volume”. Choose an appropriate name and folder to generate a FLD file. This file will be used to generate a 3D model of the rock.
13. And finally the most important step! Trial and error. Spend sometime with the software, use manual, and investigate every item in the menus.

3D Model generation

AVS Express is a powerful 3-D image processing package. The program is a modular, hierarchical, open and extensible system, with hundreds of built-in predefined components for visualizing the data. Curious readers are encouraged to go to the program website. Here, instead of giving all the boring steps (and, of course their meanings) to create an AVS Express architecture, I will give a screenshot of the final network; so that you can create the same architecture using the menus, and buttons in the main menu. See the **Fig. A.1.** All the models given in **APPENDIX B and C** are generated using this network.

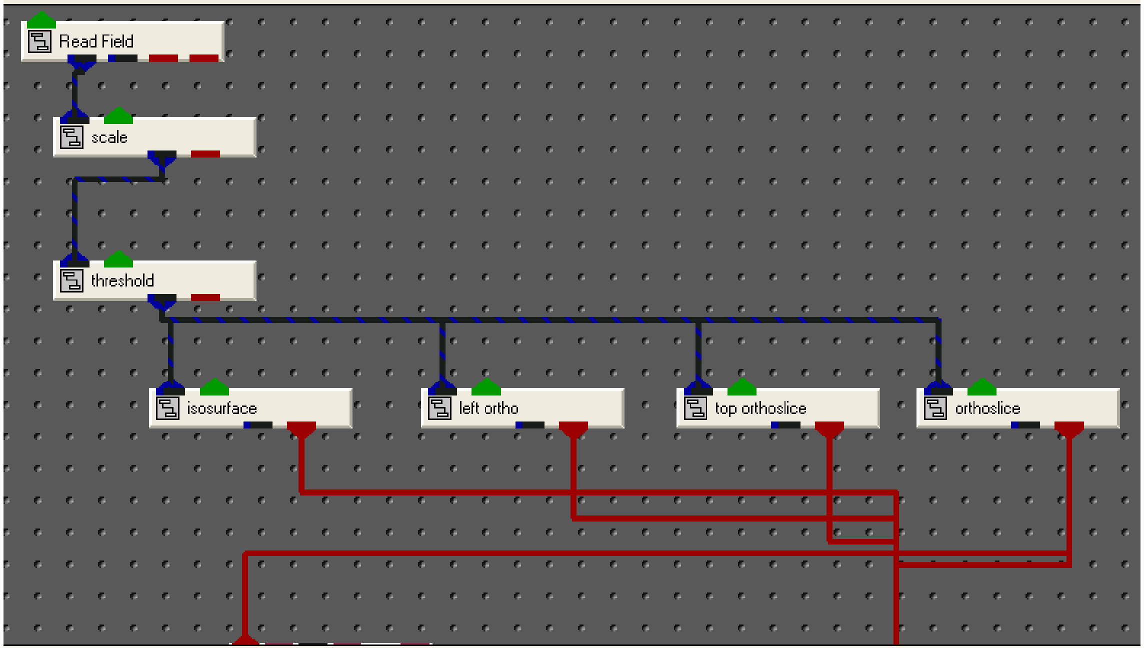

Figure A. 1 Network created in AVS Express for 3D Visualization

Having this network in the hand, only thing you need is to follow these steps:

1. Open AVS Express (Viz Edition).
2. From the menu, choose "File", "Load Application".
3. Choose the file where the network given in **Fig. A1** is saved.
4. A couple of new windows while be opened; go to "SingleWindowApp#1".
5. From the "Module" drop list, choose "ReadField" and find the fld file you would like to load.
6. There are some choices in "Module" drop list. These are "isosurface", "threshold", "scale" and "orthoslice". Simply, "isosurface" is used to visualize pixels having desired CT number. It is a good way to visualize wormholes. "Threshold" option enhances this future by putting upper and lower limits to isosurface values. The size (in 3D) of the model can be changed using "scale". Using orthoslice one can add original CT slice to specific location of the model.

This feature is also useful for visualization to mark reference points (inlet and outlet of the core etc.)

APPENDIX B

SOME 3D MODELS CONTRUCTED USING CT SCANNER DATA AND PROPOSED WORKFLOW

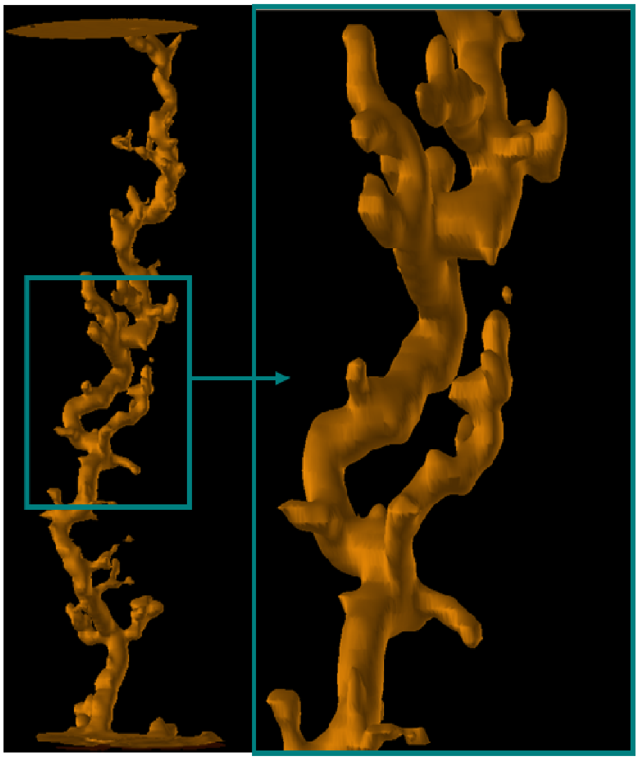

Figure B. 1 Detailed visualization of a wormhole created after acidizing of 1.5x20 inches carbonate core

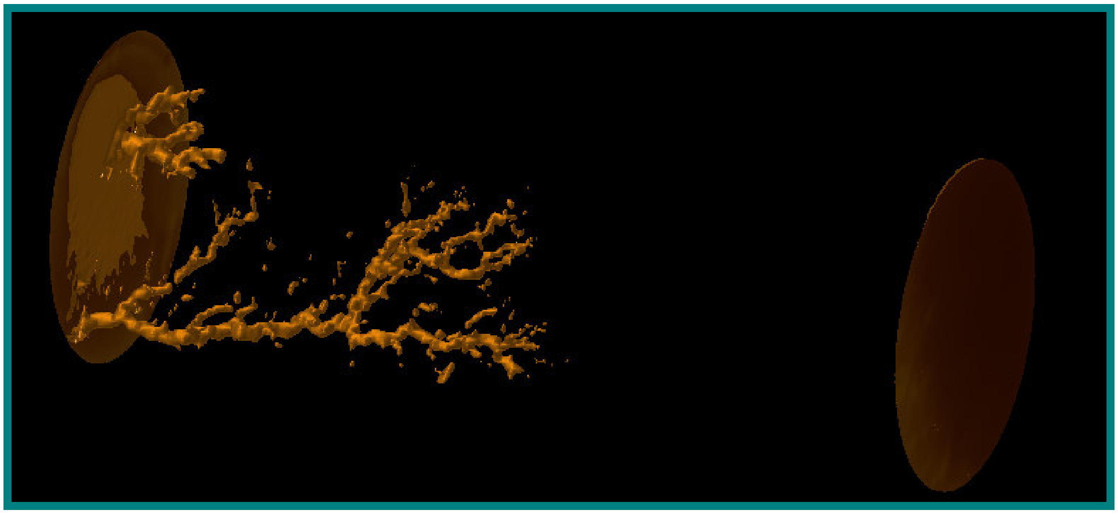

Figure B. 2 Wormhole created during an acid jetting experiment with 4-inch by 20-inch core

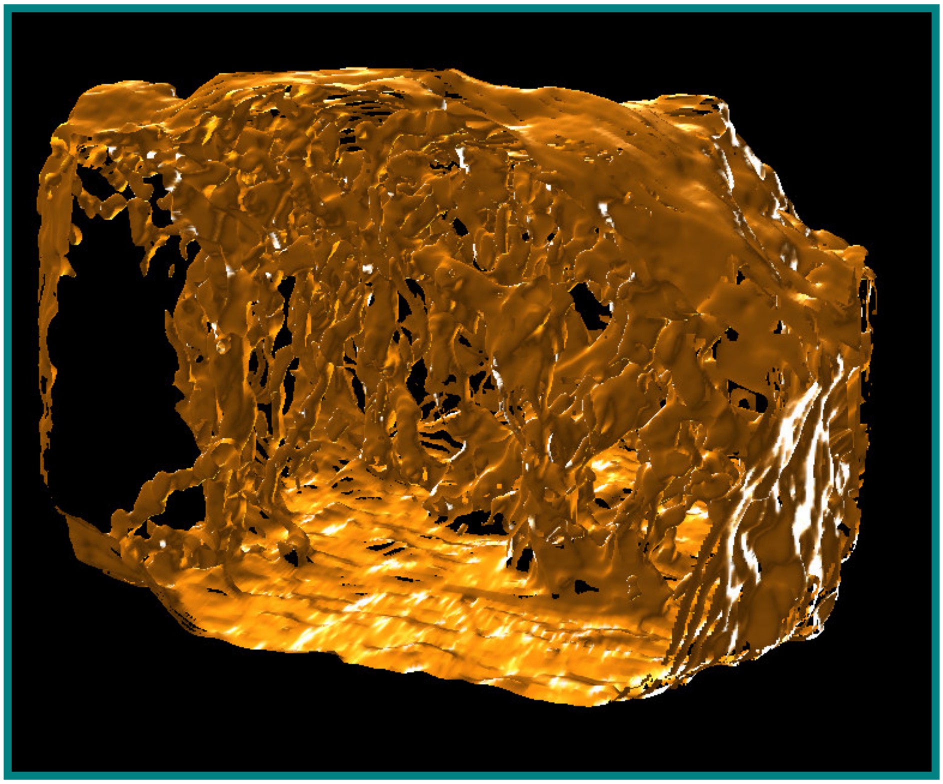

Figure B. 3 Inner structure of a highly vuggy carbonate rock (solid parts showing vug network)

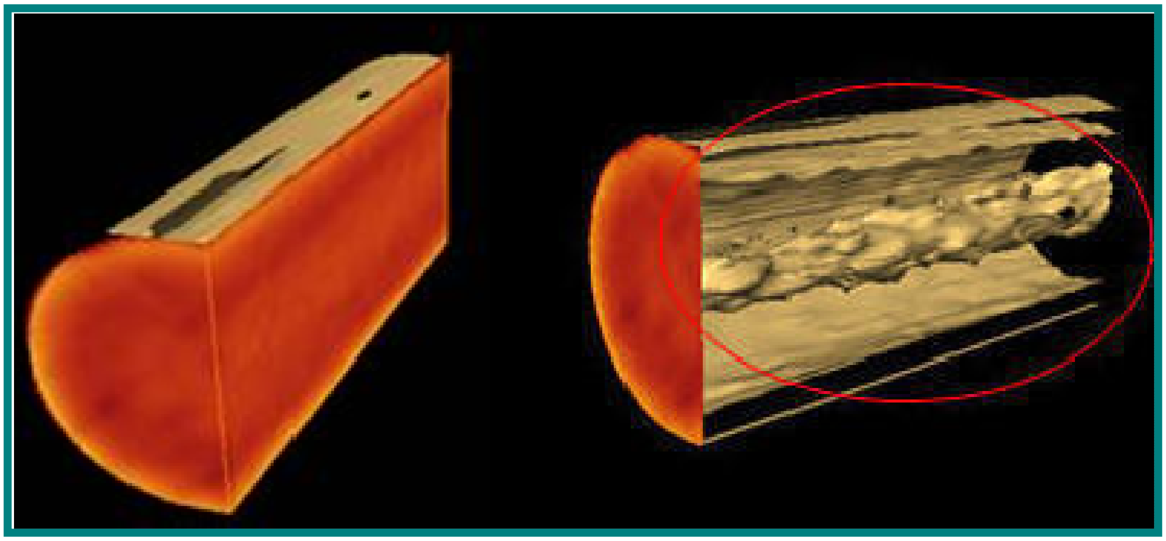

Figure B. 4 Acid flow path observed in 1x6 inches sandstone core, the area in red circle emphasize the altered permeability region following the acid treatment

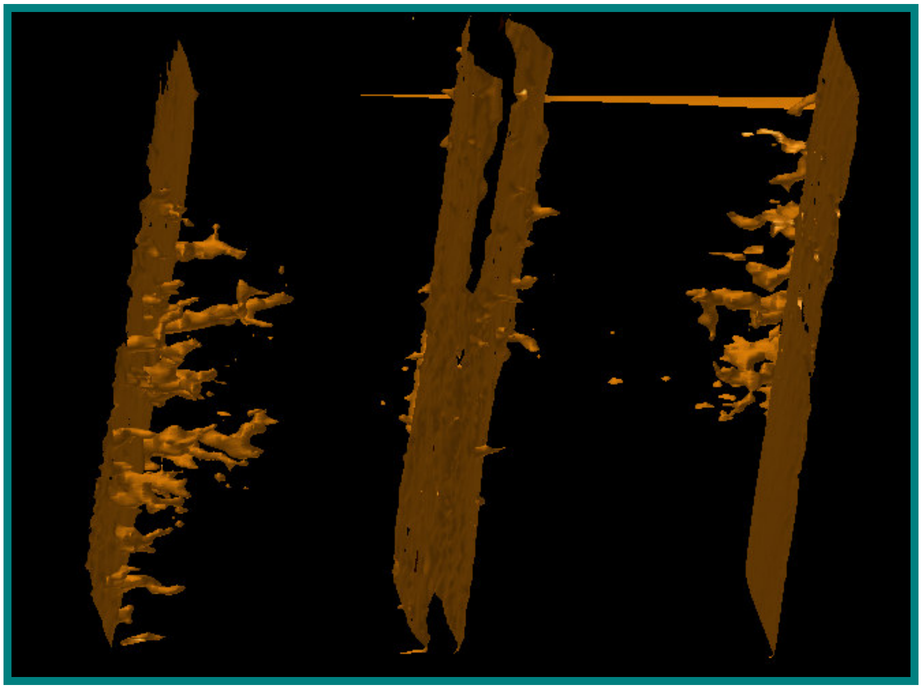

Figure B. 5 Wormholes created during acid fracturing experiments

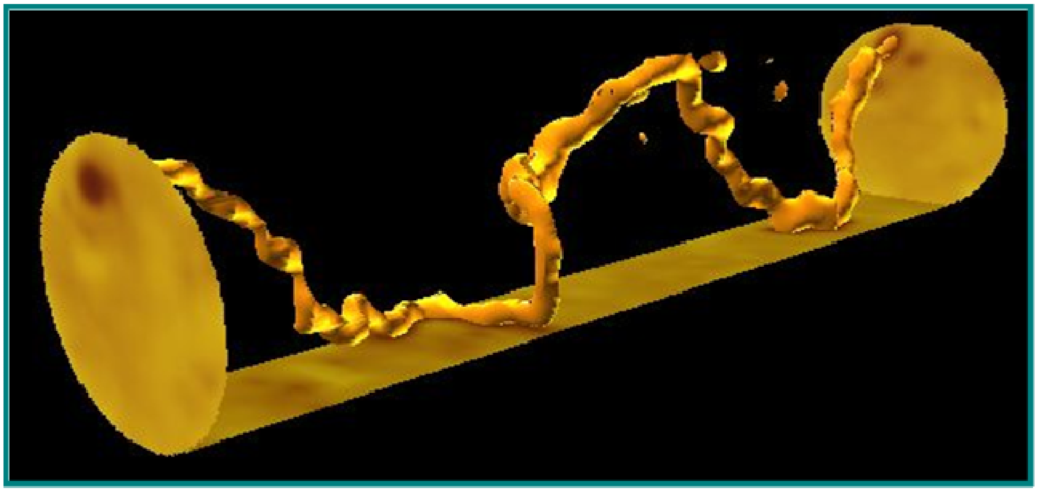

Figure B. 6 Wormholes created during acidizing experiment using a 1-inch by 6-inch cream chalk core

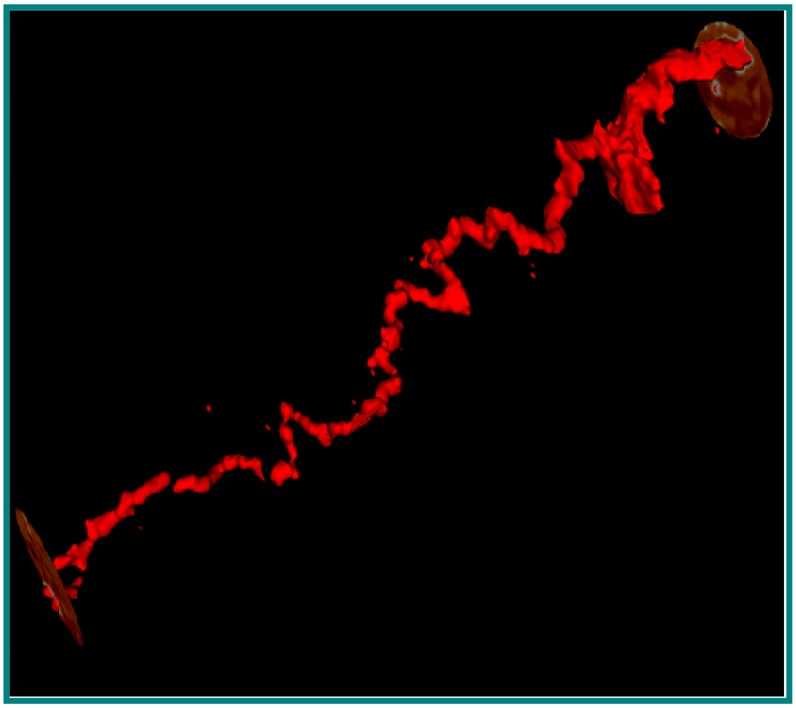

Figure B. 7 Wormholes created during acidizing experiment using a 1-inch by 6-inch cream chalk core. Method of image subtraction used

APPENDIX C

COMPARISON OF PRE- AND POST-ACID INJECTION CT MODELS

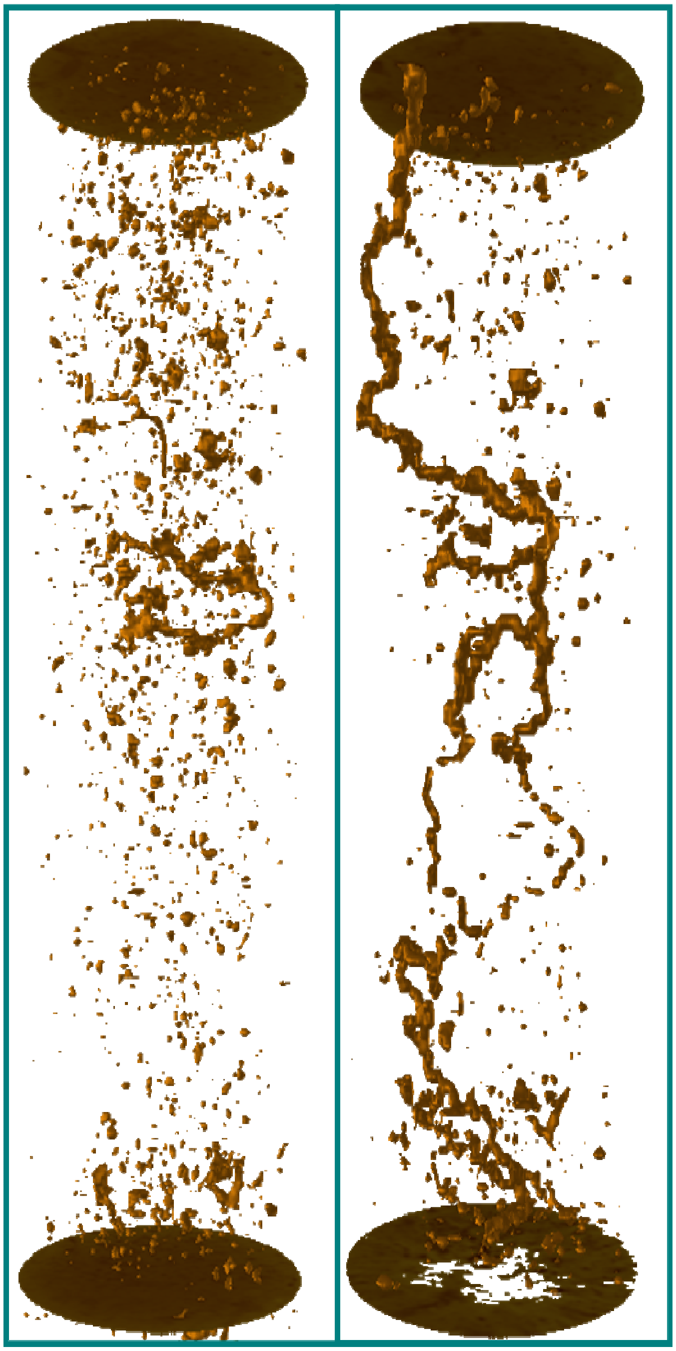

Figure C. 1 Inner structure of BC1 (solid parts showing vugs and/or wormholes)

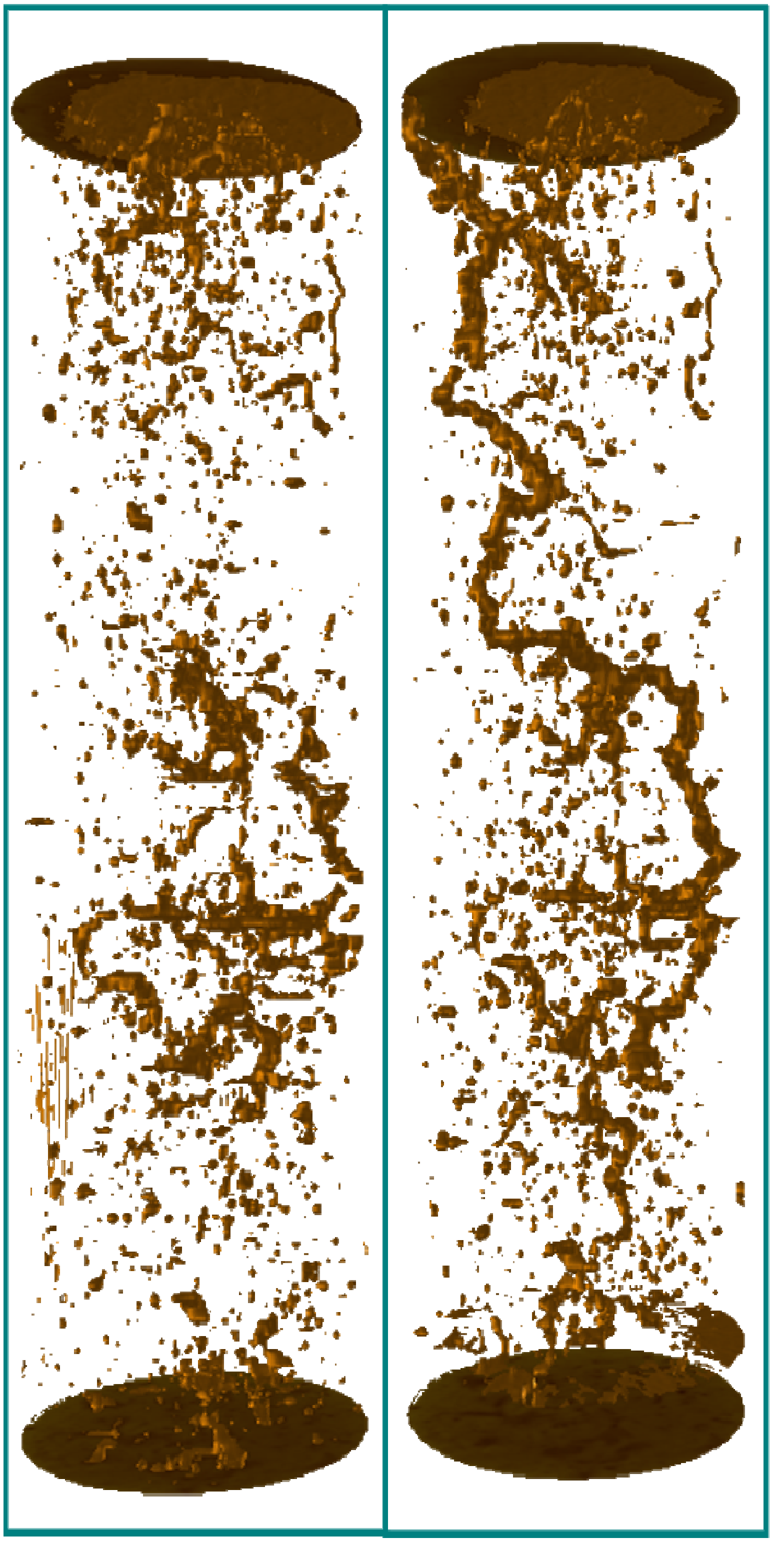

Figure C. 2 Inner structure of BC2 (solid parts showing vugs and/or wormholes)

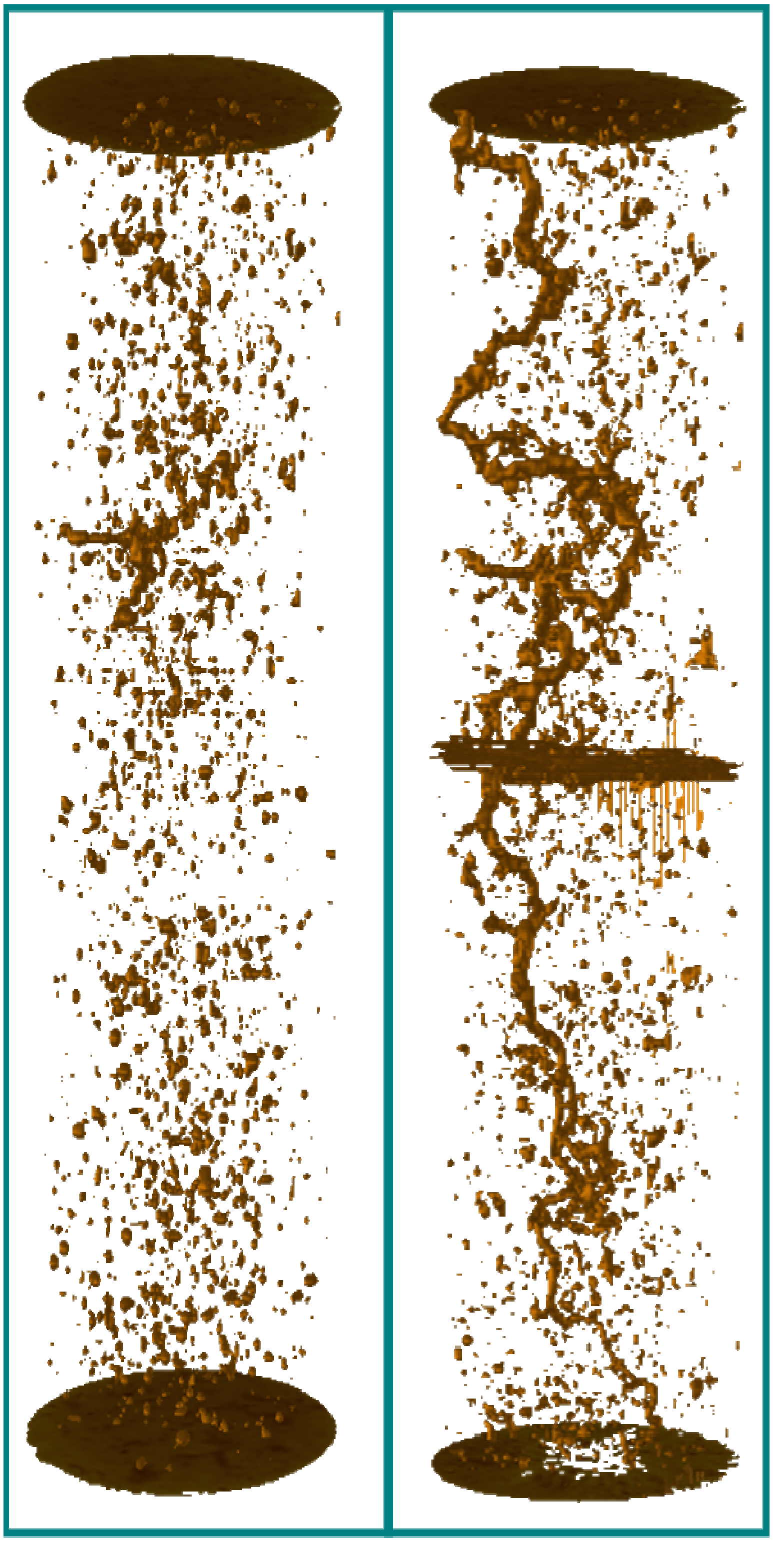

Figure C. 3 Inner structure of BC3 (solid parts showing vugs and/or wormholes)

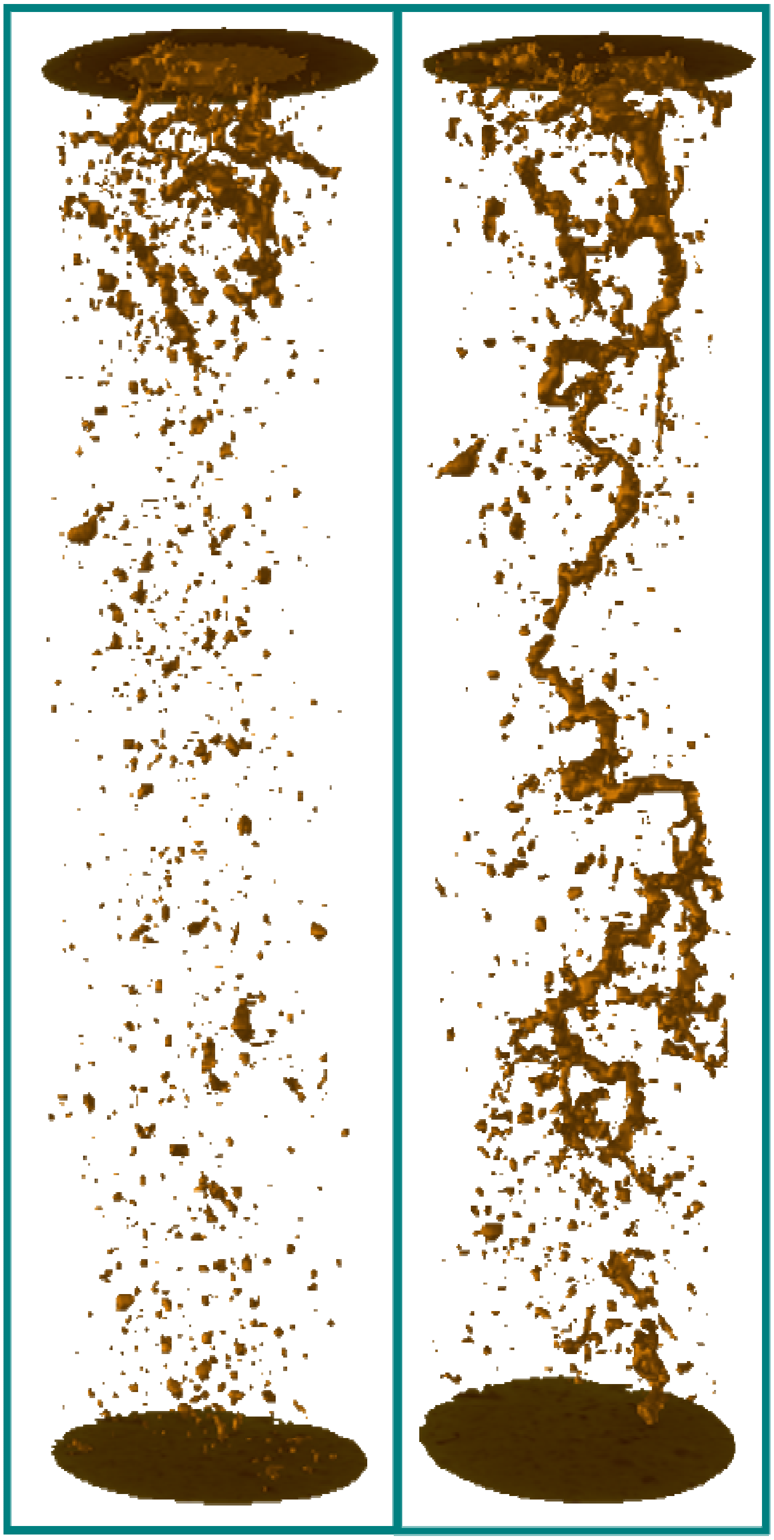

Figure C. 4 Inner structure of BC4 (solid parts showing vugs and/or wormholes)

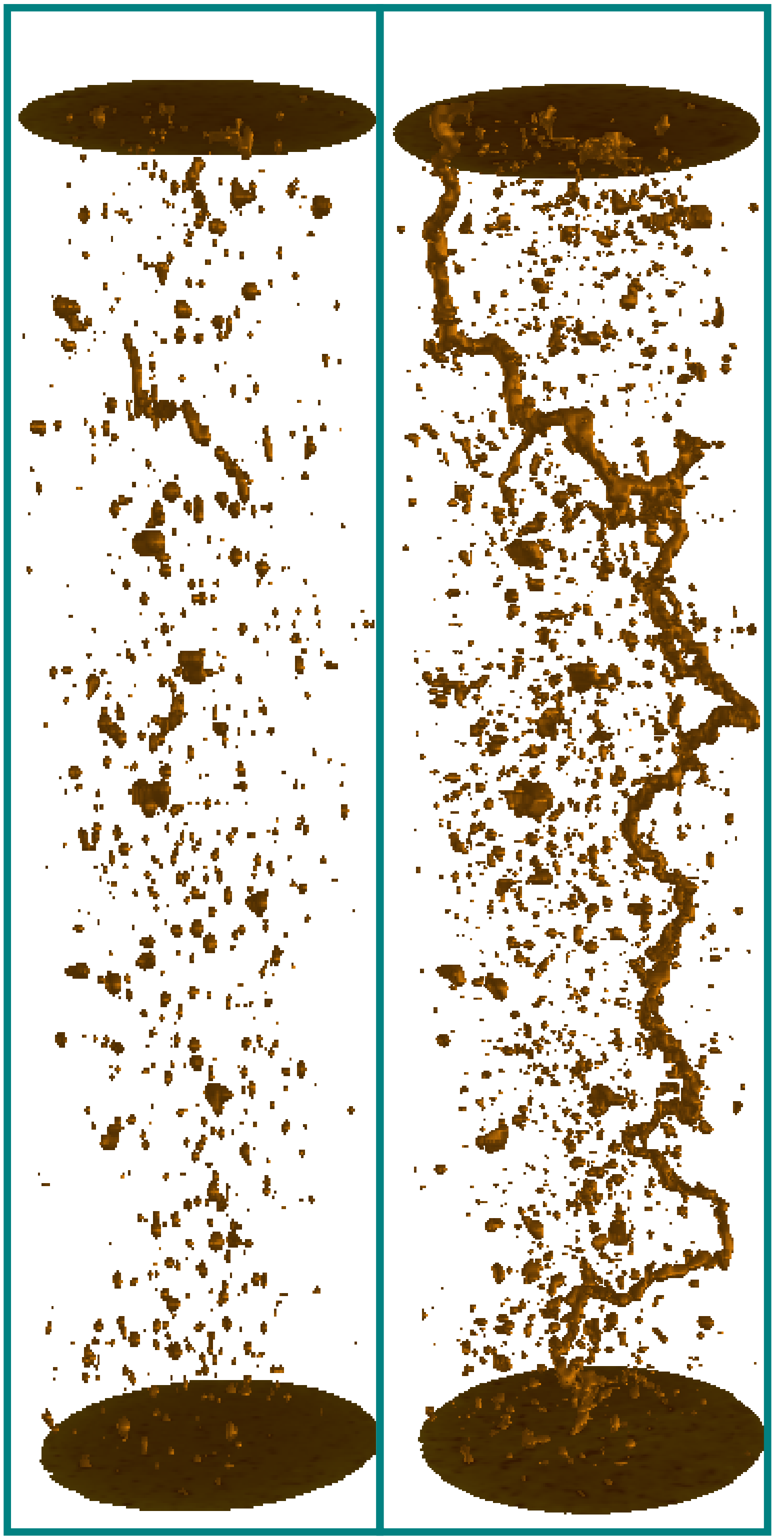

Figure C. 5 Inner structure of BC5 (solid parts showing vugs and/or wormholes)

Figure C. 6 Inner structure of BC6 (solid parts showing vugs and/or wormholes)

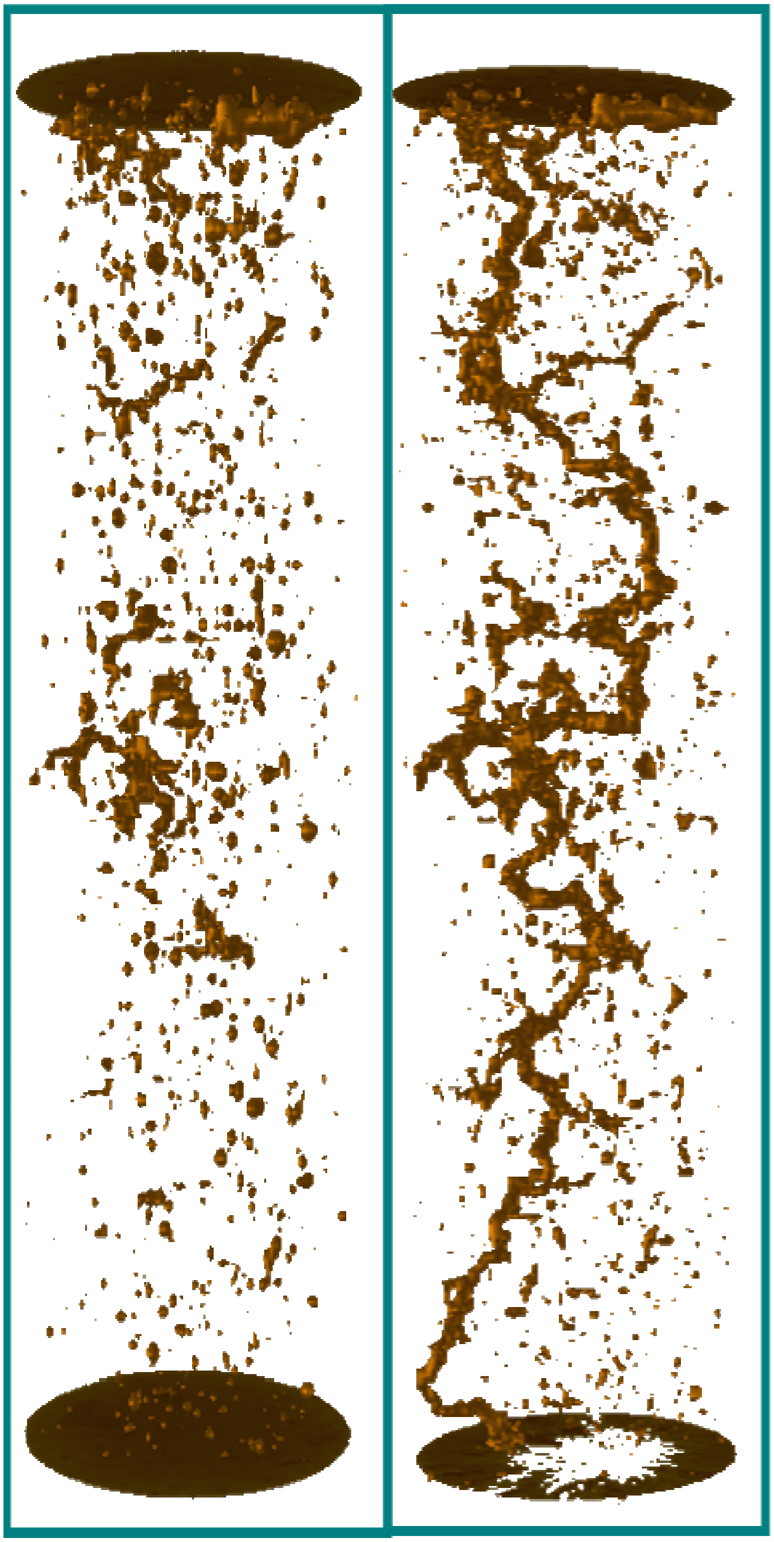

Figure C. 7 Inner structure of BC7 (solid parts showing vugs and/or wormholes)

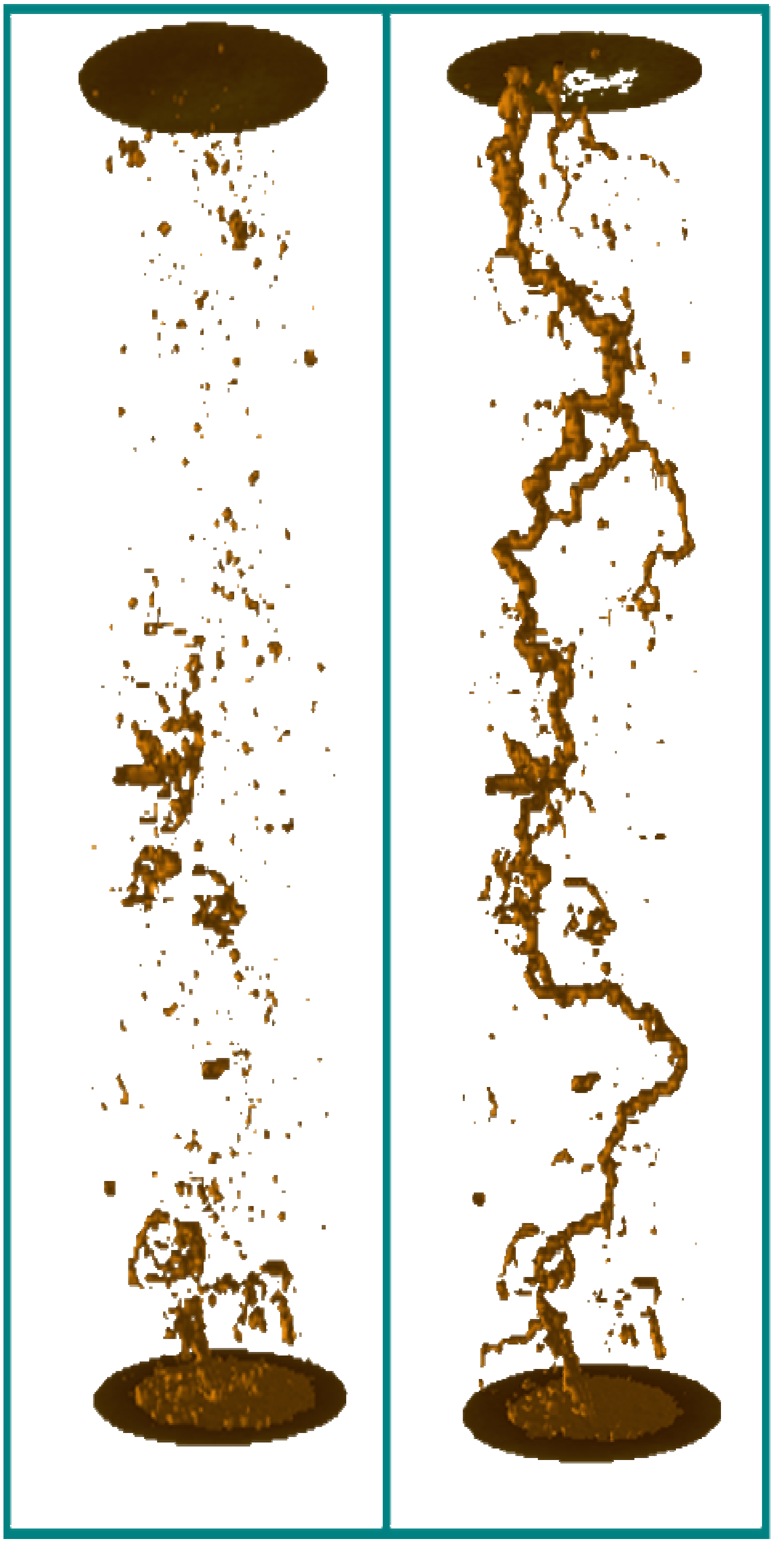

Figure C. 8 Inner structure of BC10 (solid parts showing vugs and/or wormholes)

Figure C. 9 Inner structure of BC12 (solid parts showing vugs and/or wormholes)

Figure C. 10 Inner structure of BC13 (solid parts showing vugs and/or wormholes)

Figure C. 11 Inner structure of BC14 (solid parts showing vugs and/or wormholes)

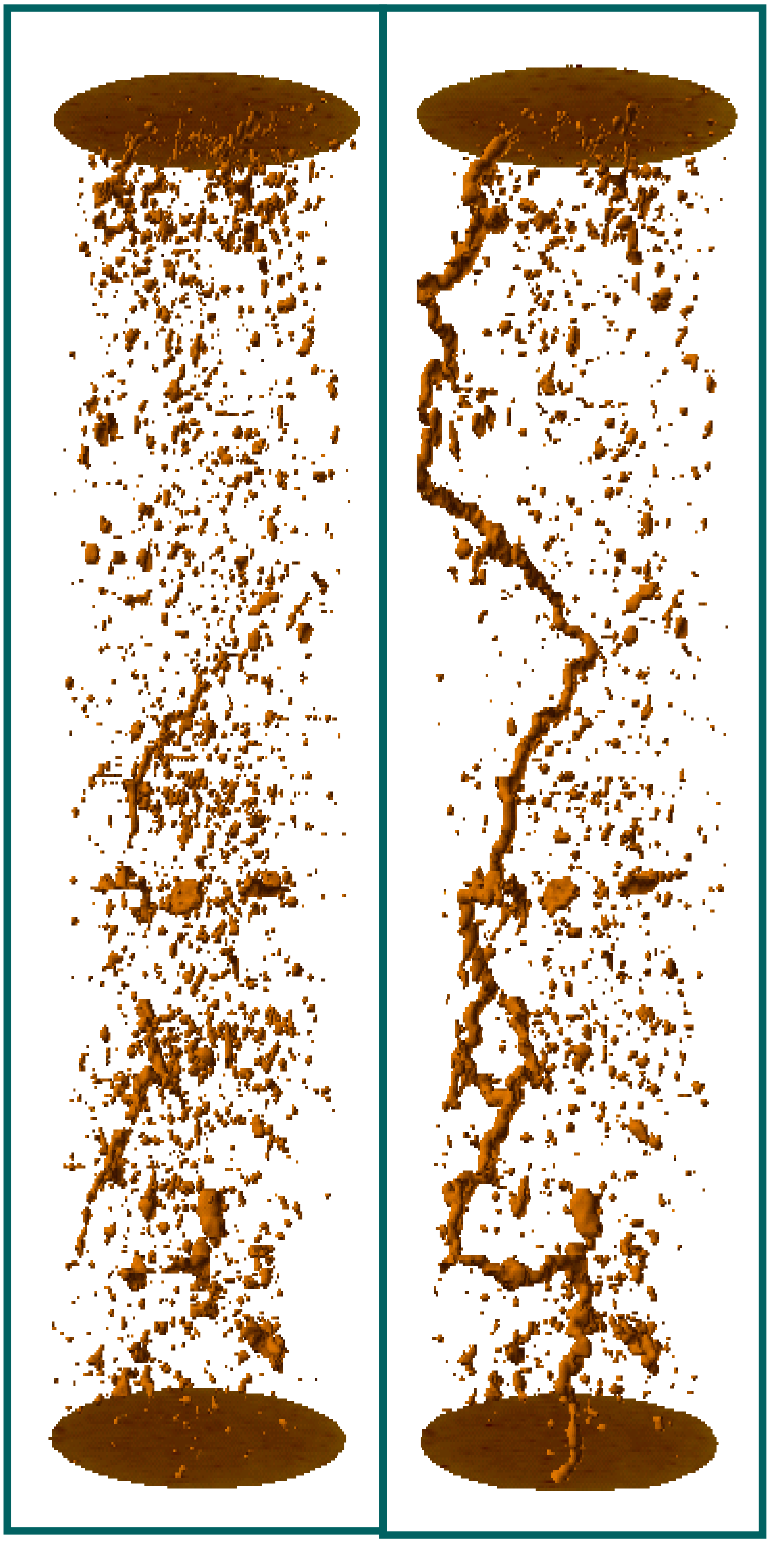

Figure C. 12 Inner structure of BC21 (solid parts showing vugs and/or wormholes)

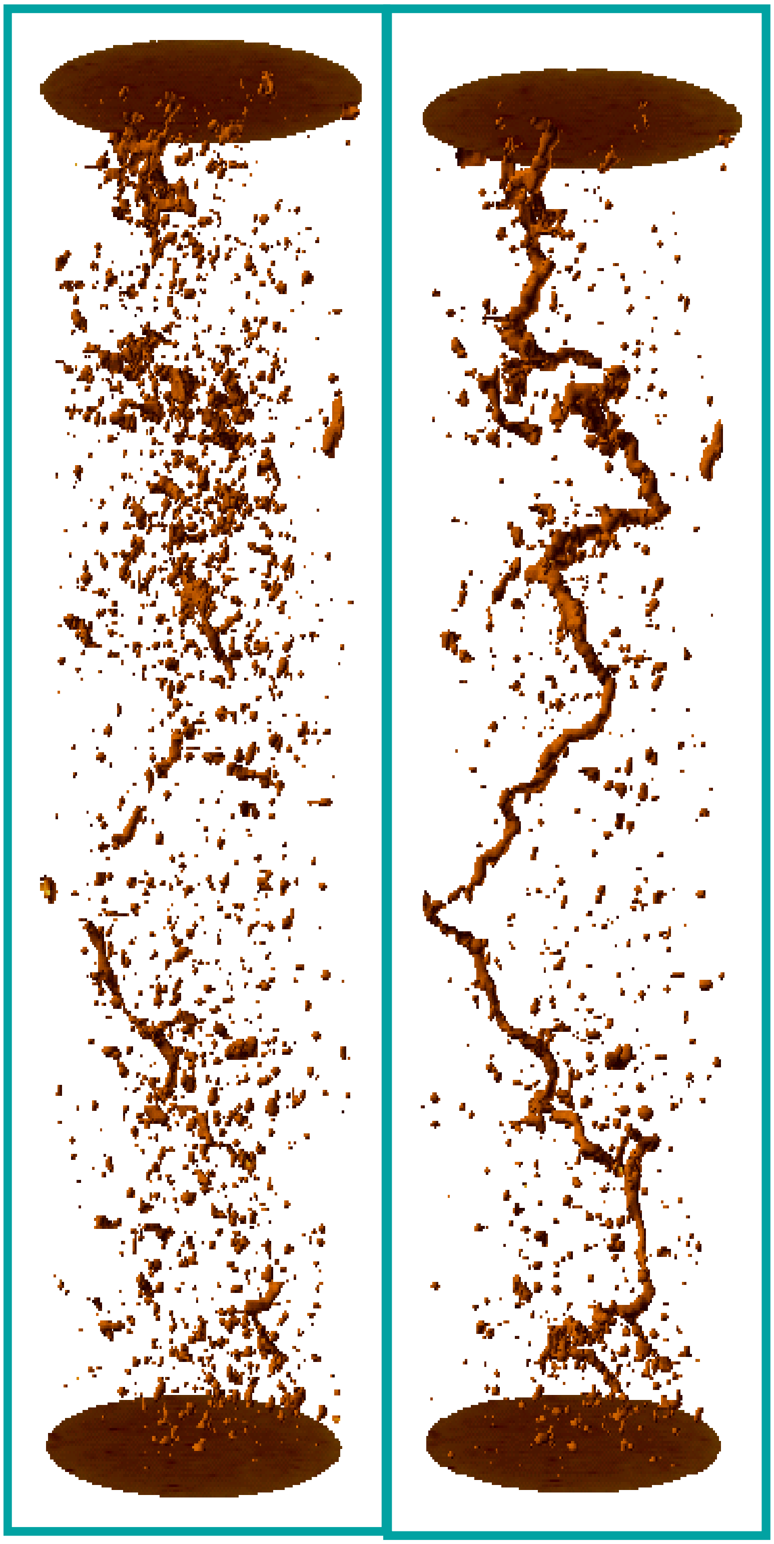

Figure C. 13 Inner structure of BC22 (solid parts showing vugs and/or wormholes)

VITA

Omer Izgec is a petroleum engineer with Chevron Energy Technology Company at *Reservoir Surveillance* team. He holds B.S. (2003) and M.Sc. (2005) degrees from Middle East Technical University (Turkey), and a Ph.D. degree (2009) from Texas A&M University. He has published in the areas of CO_2 sequestration, underground gas storage, waterflood optimization, carbonates, and acidizing. His current areas of focus are carbonate reservoirs, reservoir simulation, reservoir engineering, natural water-drive reservoirs, and CO_2 sequestration in geological formations.

He can be reached at izgec16@yahoo.com.

His permanent address is: Turgutlu Sokak, 17/15, Gazi Osman Pasa, 06700, Ankara, Turkey.

This text was typed by Omer Izgec.